Technische Universität München

Lehrstuhl für Angewandte Mechanik

Development of a high-performance-6-DoF-biomechanical joint analysis system based on an industrial robot

Jorge Horacio Martínez Prado

Vollständiger Abdruck der von der Fakultät für Maschinenwesen der Technischen Universität München zur Erlangung des akademischen Grades eines

Doktor-Ingenieurs

genehmigten Dissertation.

Vorsitzender:

Univ.–Prof. Dr. rer. nat. T. C. Lüth

Prüfer der Dissertation:

1. Univ.–Prof. Dr.–Ing., Dr.–Ing. habil. H. Ulbrich
2. Priv.–Doz. Dr. med. R. H. H. Burgkart

Die Dissertation wurde am 21.02.2012 bei der Technischen Universität München eingereicht und durch die Fakultät für Maschinenwesen am 06.09.2012 angenommen.

Preface

This Ph.D. thesis was written during my work at the division for biomechanics of the Faculty of Medicine Chair of Orthopaedics and Sport Orthopaedics settled in the Klinikum rechts der Isar at the Technische Universität München, in Germany.

Mein besonderer Dank gilt meinem verehrten Doktorvater Univ.–Prof. Dr.–Ing. Dr.–Ing. habil. H. Ulbrich, für die Erstellung des Erstgutachtens, sowie für seine Anregungen und fruchtbaren Diskussionen. Seinem lebhaften Interesse an der Arbeit verdanke ich viele wertvolle Erkenntnisse.

I would like to thank Priv.–Doz. Dr. med. Rainer Burgkart for giving me the opportunity to work under his supervision, for his support and excellent advices during my time in the division. His technical and medical knowledge were essential for the success and completion of this work. I also like to thank my ex-supervisor Dr.–Ing. Tobias Obst for his support and patience especially in the beginning and in the end of my work. Without his technical advices I would not have been able to develop such huge project.

This work was possible thanks to the helpful support from Mexico through the National Counsel of Science and Technology (CONACyT) in cooperation with the German Academic Exchange Service (DAAD).

Ich möchte mich außerdem bei der ganzen Gruppe der Biomechanik bedanken: Zuerst bei den Mitarbeitern, Eduardo Grande García und Peter Föhr, die mit unendlicher Geduld mit mir tausend Sachen diskutiert haben und mir immer mit Rat und Tat zur Seite gestanden sind. Sie haben meine Arbeit bereichert und mein Leben leichter gemacht. Außerdem bei allen Studenten, Praktikanten und HiWis, die mit viel Interesse an meinem Projekt teilgenommen haben und deren erfolgreiche Arbeiten eine große Hilfe für die Fertigstellung meiner Dissertation waren.

Mein Dank geht an meine lieben und sehr verständnisvollen Freunde, die mit netten Gesprächen, Tänzen, Sport oder sogar Meditationen, sowie einem Lächeln zwischendurch meine Arbeit leichter gemacht haben.

Quiero agradecer a mis padres y a toda mi familia por la motivación y el apoyo que me brindaron a pesar de la distancia. Sus conversaciones, cumplidos y su paciencia para escucharme fueron grandes estímulos para el término de este proyecto.

This work would not have been possible without you. Thank you.

Munich, September 2012 *Horacio Martínez*

Gedruckt mit Unterstützung des Deutschen Akademischen Austauschdienstes.

to my future and present family...
... y al espíritu...

Contents

Notations

Conventions

In this thesis scalars are denoted by letters in italic type face (k, q). Vectors and matrices are labeled by bold letters ($\boldsymbol{q}$, $\boldsymbol{A}$). The vector $\boldsymbol{q}$ is composed of elements q_i. The matrix $\boldsymbol{A}$ is composed of elements $\boldsymbol{A}_{ij}$ (i–th row and j–th column). Desired (reference) set values are marked with the subscript r ($\boldsymbol{A}_r$) and estimated (actual) values are described with an a as subscript ($\boldsymbol{A}_a$). The upper dot denotes time derivative ($\dot{q}$). Coordinate systems related to the body x are depicted with $\boldsymbol{R}_x$. A vector $\boldsymbol{x}$ represented in the coordinate system $\boldsymbol{R}_y$ is depicted with $\boldsymbol{x}_y$. Rotation matrices, which are used to transform vectors from $\boldsymbol{R}_x$ to $\boldsymbol{R}_y$ are denoted with $\boldsymbol{R}_x^y$. The superscript ^{T} denotes the transpose of the given vector or matrix and $^{-1}$ denotes the inverse of the given matrix.

Symbols

$\boldsymbol{B}$	(6×6) inertia matrix
$\boldsymbol{C}$	(6×6) centrifugal and Coriolis matrix
$\boldsymbol{F}$	(6×1) force-torque vector
$\boldsymbol{I}$	Identity matrix
$\boldsymbol{J}$	(6×6) Jacobian matrix
$\boldsymbol{K}_P$	Diagonal matrix where the constants for a position controller are defined
$\boldsymbol{K}_D$	Diagonal matrix where the constants for a derivative controller are defined
$\boldsymbol{K}_I$	Diagonal matrix where the constants for an integral controller are defined
$\boldsymbol{R}_x^y$	(3×3) rotation matrix
$\boldsymbol{A}_x^y$	(4×4) homogeneous transformation matrix
$\dot{\boldsymbol{X}}$	(6×1) Cartesian linear and angular velocity vector of the form: $\left[\dot{\boldsymbol{p}}^T\ \boldsymbol{\omega}^T\right]^T$
$\boldsymbol{f}$	(3×1) forces vector
$\boldsymbol{g}$	(6×1) gravity vector
k_r	Gear ratio of the corresponding transmission
k_t	Motor constant
$\boldsymbol{p}_x$	Position vector of point x
$\dot{\boldsymbol{p}}$	(3×1) Cartesian linear velocity vector
$\boldsymbol{q}$	(6×1) joint position vector
$\dot{\boldsymbol{q}}$	(6×1) joint velocity vector
$\ddot{\boldsymbol{q}}$	(6×1) joint acceleration vector
$\boldsymbol{\omega}$	(3×1) Cartesian angular velocity vector
$\boldsymbol{\tau}$	Torque vector
$\boldsymbol{\phi}$	(4×1) quaternion

Abbreviations

CAD	Computer–aided–design
DD	Direct dynamics
DK	Direct kinematics
DoF	Degrees of Freedom: the set of independent displacements and/or rotations that specify completely the displaced position and orientation of a body or system
FTS	Force-Torque sensor
GUI	Graphical User Interface: user interface that allows the user to interact with a computer. It provides graphical icons, visual indicators or special graphical elements called widgets
IAR	Instantaneous axes of rotation
ID	Inverse dynamics
IJC	Independent joint control
IK	Inverse kinematics
PID	Proportional, integral and derivative controller
ROM	Range of motion
RT	Real-time
SCS	Sensor coordinate system
TCS	Tool coordinate system
TCP	Tool center point
WCS	World coordinate system

Abstract

A novel system to test biological specimens in 6 DoF is here presented which provides a solid foundation to perform complex, robust and scalable biomechanical experiments. Basic functions have been implemented within the new proposed system to cover different fundamental demands directly related to the robotic arm, such as motion control in joint and Cartesian space, current commanded motion and two approaches of interaction control: hybrid control and direct force control to load specimens exerting desired forces and moments in predefined axes. The interaction with the framework through a GUI and a 3D visualization provides a friendly, intuitive and easy way to use the system. A safety concept was developed providing the protection of damage for the user, for the specimen, for the environment and for the robot itself.

The control architectures were tested with non-biological and biological materials. Direct force control was robust enough to ensure stability when testing both types of materials. The system is able to perform different experiments in different time intervals. It has been shown that the biological specimen can be moved in the free space without any restriction. This experiment setup allows an anatomical and therefore more realistic movement in vitro of biological specimens. The contribution of this work is a proposal of a novel system architecture which makes possible to accomplish high complex tests in human and animal joints.

1 Introduction

The science of biomechanics explores the mechanics of "biological entities". It analyzes biological specimens under the mechanical aspect. The physical concepts like static, kinematic, dynamic, deformation, fatigue, are applied in biological systems like musculoskeletal system, vascular system, respiratory system and more [50].

An accurate description and knowledge of the human body (such as its stiffness, viscoelasticity, force, strain and stress) is necessary to develop and construct better medical implants and to develop better and suitable therapies and rehabilitation programs. Therefore biomechanical experiments are performed in order to find the properties of these complex systems.

In vitro (latin for "within glass") experiments refer to biological studies that are performed using components of an organism that have been removed or isolated from their usual biological context in order reduce the complexity of the whole organism and separate the part of interest. *In vivo* (latin for "within the living") experiments refer to biological studies where a living organism in its biological context is the center of study.

Biomechanical studies are nowadays accomplished mostly with the help of universal testing machines [16,85,145] (Figure 1.1), which allow analyses in 1 or 2 axes. In order to analyze in detail biological specimens it is necessary to describe their biomechanical properties such as forces, degrees of freedom, axes of rotation, stiffness, viscoelastic properties, configuration of ligaments, geometry of the surfaces and friction. However, the specimens to test are complex systems (e.g. human or animal joints) and the DoF of universal test machines are not enough to evaluate all these properties. A human joint is much more complex to describe than a "simple" rigid structure since a joint involves more than one fixed structure, its viscoelasticity is non linear and depending on the position and angular configuration of the limbs, the degrees of freedom are coupled and its range of motion depends also on the position. To perform these complex tests, complicated constructions and mounted engines are needed. In this way, forces and moments can be applied in additional degrees of freedom in order to determine mechanical properties of the biological specimens.

The usage of robots in these kind of analyses has become essential to accomplish specific experiments that fulfill the required complexity. Current applications use robots to apply forces, moments, displacements, and specific behaviors of human joints [59, 60, 62, 63, 132, 141, 143, 154]. These kind of systems allow to test bones, joints, soft tissues, artificial joints and other biological specimens with certain flexibility.

1.1 Motivation

As the mean age of the population increases, the number of patients that need surgical intervention in a motion organ continues to grow according to the Federal Office of Statistics

Figure 1.1: Universal testing machine Roell Amsler. Division of Biomechanics. Klinikum rechts der Isar of the Technische Universität München, Germany

in Germany [17]. Better methods to insert implants are required where the surgeon can know the best place and orientation in the patient body to fix such implant. In order to optimize this knowledge it is mandatory to comprehend in detail the role that play different ligaments, bones, muscles and tendons in a joint. How the forces act in these parts and the effect that those produce in the deformation, elongation, stiffness, viscoelasticity, constraints, and friction are until these days unknown.

Biomechanical *in vitro* tests help to perform experiments in order to load human joints. With the help of sensors it is possible to measure the response of the ligaments that are actuating to bend, opposing or supporting the movement within their own range of motion. The setup of the experiments plays a very important role in the analysis of biological specimens. The experiments can be configured in such way that they simulate or recreate, as close as possible, the reality. This is a huge challenge due to several reasons (e.g. *In vivo* tests are difficult to develop without cutting or altering the tissue or biological part to test [10, 90, 113, 150, 155]) and lack in the data. Even when all biomechanical properties can be known it is very difficult mechanically to simulate or recreate the overall biological effects.

Even if *in vitro* biomechanical tests do not represent, exactly, the reality, they are very useful for understanding the viscoelastic properties of the tested specimens. This knowledge is also used by the endoprosthesis manufacturers and surgeons. The results of these tests can give valuable information of the resistance, stiffness and other properties that the implants

must have in order to ensure performance, durability and other features to maximize their lifetime and provide safety and health to the patients.

In contrast to universal testing machines with 1 or 2 DoF, a robotic system is able to execute complex movements and apply complex loads on the specimens. Such manipulators with different possibilities of movement offers several advantages. The robot can load specimens with different forces and moments in different directions, without constraining them to only 2 DoF. It is also possible to repeat multidimensional movements with high accuracy. Thus the stress can be determined on a specimen with an intact or reconstructed ligaments damaged in an identical motion. By comparing the forces and moments in the intact and damaged specimen, a valuable insight into the functions of the anatomical components of the specimen can be obtained. On the other hand, after the data has been evaluated, it would be possible to test and compare different implants or even surgical techniques. The measurements may also prove to be valuable for the validation of simulation models. Another possibility, which the system can perform, is the measurement of the load on the specimen by natural movements. For this purpose, data from in vivo measurements of human motion can be acquired in order to be transmitted as a trajectory to the robot. The measured forces and moments, when the robot performs movements of the biological joint, give hints to identify the body parts that are more or less mechanically loaded at certain points of the movement. Another advantage using a robotic system is that the kinematic of the robot is already described. The position, velocity and even acceleration of the end-effector is known through the kinematic chain of the robot links. This information corresponds directly with the kinematic of the tested specimen. This means that the characterization of the kinematic of the biological tested body is also known and can provide clinically relevant data.

1.2 Goals

The division for biomechanics of the Faculty of Medicine Chair of Orthopaedics and Sport Orthopaedics settled in the Klinikum rechts der Isar at the Technische Universität München in Germany, is engaged to develop a high-performance 6 DoF biomechanical joint analysis system based on an industrial robot. The robotic system may be thought as a testing machine that can apply loads (according to its positions or forces) in a 6 DoF environment (3 forces or displacements and 3 moments or rotations). The system should be able to apply these loads separately or in combination, that is to say, it should be possible to apply any force or moment in any direction or around any axis, respectively. The specimens should be free to move in the 6 DoF.

The interaction with the machine should ensure safety for the user, for the specimen to test, for the environment and for the robot itself. The contribution of this work is a proposal of a framework architecture and a system which makes possible to accomplish high complex tests in human and animal joints. A modular structure, together with a strategic distribution of the modules provides flexibility for the adaptation to different sizes and kinds of specimens. It should provide as well scalability, allowing the replacement or the addition of sensors, change or modify the control architectures, and adapt or modify the experiment setups. All this should be made without a big effort and expense of time.

The system architecture should be flexible enough to adapt itself to the different experimental scenarios with biological specimens without requiring exhaustive changes in the internal structure. It should be constructed in a modular way in order to distribute the tasks depending on their role. A modular architecture offers a better maintainability, simplicity, flexibility and scalability. In this way, the upgrading, replacing or adding a new component must not affect the basic structure of the system.

The robot should be able to move also under force and position control. The tested bodies can be loaded also applying certain displacements and rotations (e.g. following a predefined trajectory given in position/orientation or force/moment values) in order to collect data (e.g. forces and moments, or kinematic variables like velocity or acceleration) of the specimen.

A particularly issue to be considered when thinking about biomechanical tests using a robotic system is the presence of singular configurations of the manipulator. In the neighborhood and at particular configurations an exact solution of the robot inverse kinematic becomes singular. Consequently, unfeasible joint velocities may be produced which yields into unexpected behavior of the robotic system. During the test of specimens, high velocities and position deviations can damage the system, the specimen and represent a danger to the user. Therefore, another important objective of this work is to assure safety in the presence of such singular robot configurations.

The framework should be able to be operated without a depth knowledge of the system. Due to this, it is necessary to develop a GUI where the most important parameters for the controller and for the experiment setup can be introduced avoiding also that the user modifies important variables or configuration that can damage any components.

The system should be able to display a virtual 3D environment in order to visualize the robot connected with the specimen. This has the objective that the user can observe the scene from different angles in order to define specific parameters for a specific experiment. This virtual world should also provide a visibility of the test from a close perspective without being in the range where the robot can move. This 3D environment should be also available in simulation for planning purposes.

The parameters that are wanted are the viscoelasticity of the specimen, where both, viscous and elastic characteristics under deformation, are sought. The stiffness, where the resistance of the specimen to deformation by an applied force is wanted. The role that the different constraints (due to constraining forces, mechanical coupled degrees of freedom and elastic and viscous properties) play in the specimen when tested. The analysis of such anatomical specimens is highly complex because it is not an isolated material that is to be tested but a complex system where constraining forces (depending on the position and orientation of the components) arise. The elastic properties are not linear and the ROM of every joint is highly complex.

The time to perform the experiments is a very important parameter due to a decomposition process of biological specimens. The features of a specimen degenerate every second that passes by. The system should be able to perform different experiments in a relative short time in order to acquire representative and suitable data. This time may be introduced by the user, where the time of the experiment (followed profile under position/orientation or force/moment variables) is defined. The system should be able to load specimens with different velocities in order to implement static and dynamic tests.

The work with biological specimens requires the attachment of bones, muscles, tendons, ligaments, adipose tissues and the combination with blood and other substances to the testing machine. This attachment becomes a critical issue. In order to perform any biomechanical test, the fixation of the biological specimen should be ensured within the whole time of the experiment.

Covered these goals, the machine would be able to perform high complex tests in the space of anatomical specimens in order to provide valuable information about their kinematics, dynamics and quantification of their physical properties.

2 Background

2.1 The Spine

The human spine is part of the musculoskeletal system and forms the central axis of the human body. To understand the mechanism and functional disorders of the human spine, a basic knowledge about the anatomy and pathology of the spinal column is required.

Anatomy

The human spine consists of 25 vertebral bodies arranged in column structure at the posterior of the neck and trunk of the body. The spine (Figure 2.1) is divided into four sections: cervical (7 vertebral bodies), thoracic (12 vertebral bodies), lumbar (5 vertebral bodies), and sacrum. Each vertebral body has a hard shell of cortical bone of 1 to 3 mm thickness and an inner trabecular bone (Figure 2.2). As seen in Figure 2.1, the cervical and lumbar sections have a naturally lordotic curvature while the thoracic and sacral sections have a naturally kyphotic curvature structure.

A typical lumbar vertebral body is shown in Figure 2.2(a) and consists of an anterior (body) and a posterior (foramen) section. The body contains the attachment sites to the intervertebral disc and has a thin layer of cartilage. This section constitutes the vertebral body. The foramen contains lamina and pedicle which encloses the spinal cord protecting it. The transverse processes bulges laterally and give the attachment points for muscles and ligaments. The spinous process allows attachment points for muscle and ligaments and is the most posterior structure of the vertebral body. The uniform basic shape of every lumbar vertebra is adjusted in each section to the various static and dynamic requirements. Each lumbar vertebra, like the shown in Figure 2.2(b), consists of a ventral vertebral body, *corpus vertebrae*, and a bony arch situated on the dorsal side, *arcus vertebrae*, the spinous process, *proc. spinosus*, and two transverse, *proc. transverse*, and four articular processes *proc. articular* [117].

The anatomy of the articular processes is for each region of the spine distinctive and its orientation is determined by the geometry and mobility of each segment. The movement of the vertebral column is not only determined by the shape of the vertebrae, but essentially by the architecture and material properties of intervertebral discs and ligaments. The interaction of these individual elements allows to maintain a certain body position (static function) and to ensure mobility of the trunk (dynamic function) [85].

White [151] defines the functional spinal unit or the motion segment as “the smallest segment of the spine that exhibits biomechanical characteristics similar to those of the entire spine. It consists of two adjacent vertebrae and the connecting ligamentous tissues”. According to White [151] the main directions of motion of a functional segment are:

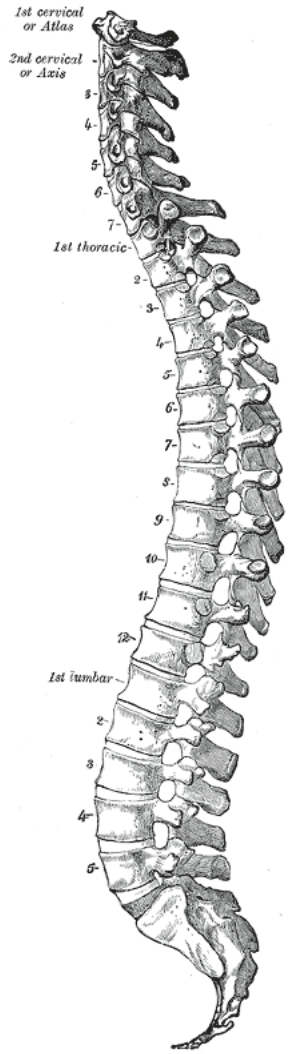

Figure 2.1: Vertebral column [64]. C1-C7 cervical, Th1-Th12 thoracic, L1-L5 lumbar and sacrum.

flexion extension (FE), lateral bending (LB) left/right and axial rotation (AR) left/right (Figure 2.3).

Pathology

Pathology is the study of diseases and deals with their causes, development and consequences like morphological changes in the body. Basically there are two types of back pain: the specific and nonspecific. In 85% of all back pain patients an exact cause cannot be detected [14, 37]. If this is the case, the term "non-specific back pain" is applied. For specific back pain there is a demonstrable morphological cause in the spine and occur 15% of all diagnoses [14]. The causes include trauma, degenerative changes, inflammation, infections and tumors. Eysel [37] presented a percentage distribution, showed in Table 2.1, with respect to their occurrences in the ventral or dorsal region of the vertebra.

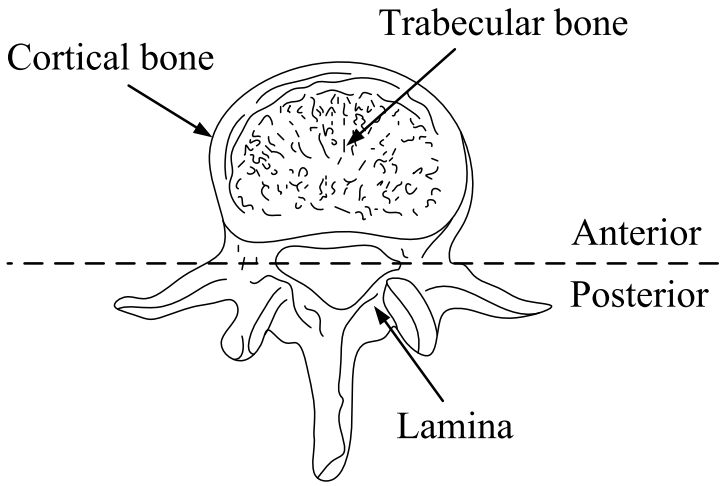

(a)

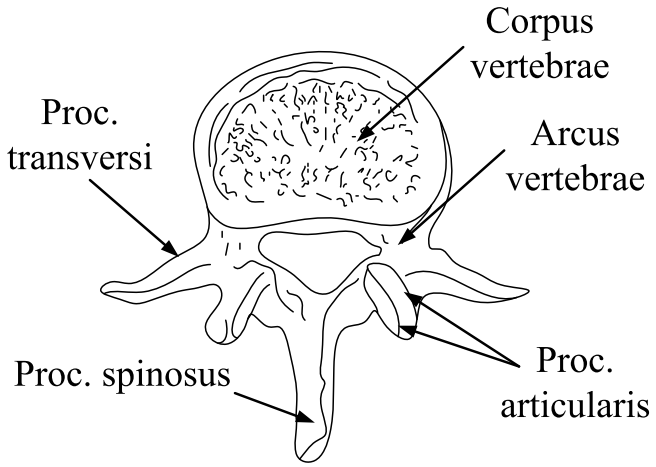

(b)

Figure 2.2: Transverse view of a lumbar vertebral body.

Magerl [104] proposed a new classification of thoracic and lumbar fractures. This classification is established according to the main mechanism of injury. Magerl considers three main types: A, B and C which injury pattern is determined by the forces acting on the spine such as compression, distraction and axial torque. Type A considers all injuries caused by vertebral body compression, type B considers all injuries in anterior posterior element caused by distraction and type C considers all injuries in anterior posterior element caused by rotation. Figure 2.4 shows this classification.

Type A fractures occur in 66.1%, type B in 14.5% and type C in 19.4% of the cases in a study of 1445 consecutive thoracolumbar injuries [104]. The injury of the first lumbar vertebra and the adjacent structures has 49% probability to occur and is with it the most frequent [11, 104].

Benign and malignant tumors of the spine occur in all age groups and in each spinal segment. Since the spine is a suitable place for bone metastases, 97% of all spinal tumors are metastatic and 3% are of spinal origin [26]. Among the most common primary tumors

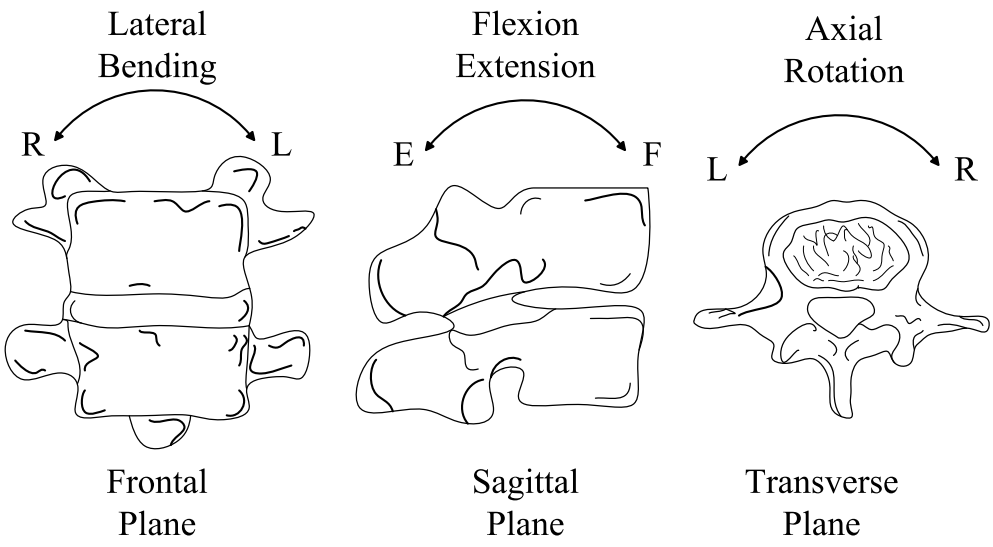

Figure 2.3: Spine rotations. Letters R and L stand for right and left respectively, F and E for flexion and extension.

Table 2.1: Percentage distribution of the pathological occurrences in the dorsal and ventral region of the spine [37].

	Dorsal	Ventral
Deformation	50%	50%
Degeneration	50%	50%
Tumor	10%	90%
Inflammation	0%	100%
Fracture	30%	70%

that cause the spine metastases are lung tumors, hematological tumors, renal cell cancer, breast and prostate cancers [26]. This can result in advanced growth of the tumor or the collapse of the vertebral body and/or the compression of the spinal canal [16].

Another pathological change in the spine is caused by degeneration of the connective tissues and bony structures of the spine. The degeneration of the bone structure of the spine usually occurs in advanced age [16]. Osteoporosis is one of this degeneration and can lead to bone fractures.

In the connective tissue structures, degeneration occurs mainly in the intervertebral discs. Due to reduction of the water binding ability of the tissue, the elasticity of the intervertebral discs decreases. Consequently, the shock absorbing function under axial load is reduced [112].

2.2 Spine Biomechanics

Knowledge of biomechanical properties of the spine is a prerequisite for experimental studies on isolated motion segments.

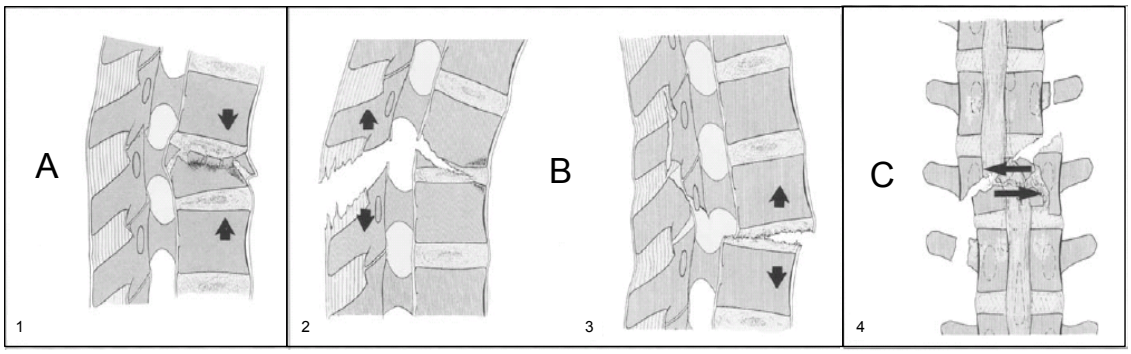

Figure 2.4: Modified according to Magerl [104]. Classification of three types of injury. Type A (1), compression of the anterior column. Type B, posterior transverse disruption (2) and anterior transverse disruption (3). Type C, injury caused by rotation. Reprinted with kind permission of Springer Science and Business Media.

The movements of individual directions of specific segments of the spine (specimens) can be represented in a load-deformation curve (Figure 2.5). In the neutral zone (NZ) the structures are considerably deformed under low load. If this increases, the structures reach the elastic zone (EZ). In this area the specimen does not return to its initial state if the load is relieved due to viscoelastic properties of the segments. However, a damage in the specimen in this phase does not occur. Both regions, NZ and EZ constitute the ROM of the specimen. After the EZ follows the plastic zone (PZ) where the specimen suffers an irreversible damage.

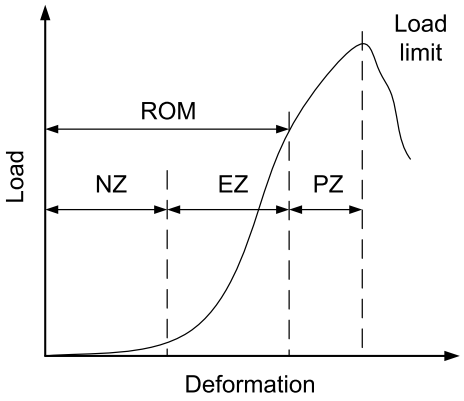

Figure 2.5: Modified according to White [151]. Load-deformation curve. NZ stands for neutral zone, EZ for elastic zone, PZ for plastic zone and ROM for range of motion.

The range of motion (ROM) is the sum of the neutral zone and the elastic zone in one direction of motion. It is the most common kinematic parameter used in biomechanical testing protocols in order to evaluate spinal devices. It is the total motion of the spinal section in study. Normally the ROM will compare this movement from a healthy specimen with an instrumented or surgically altered specimen in order to report a quantitative analysis of the effects of spinal devices.

The ROM is very wide and every section has different parameters. The cervical section allows to move the head in a lateral bending about 35° in both directions and in flexion-extension of 65° and 40° respectively. In the transverse plane a rotation of both sides about 50°. The thoracic section allows movements of 40° in lateral bending in both directions, 85° and 60° in flexion-extension respectively. In the transverse plane a rotation about 40° of both sides [133]. The complete movement of the whole spine depends of 25 segments mechanically coupled which makes it a very complex articulating column.

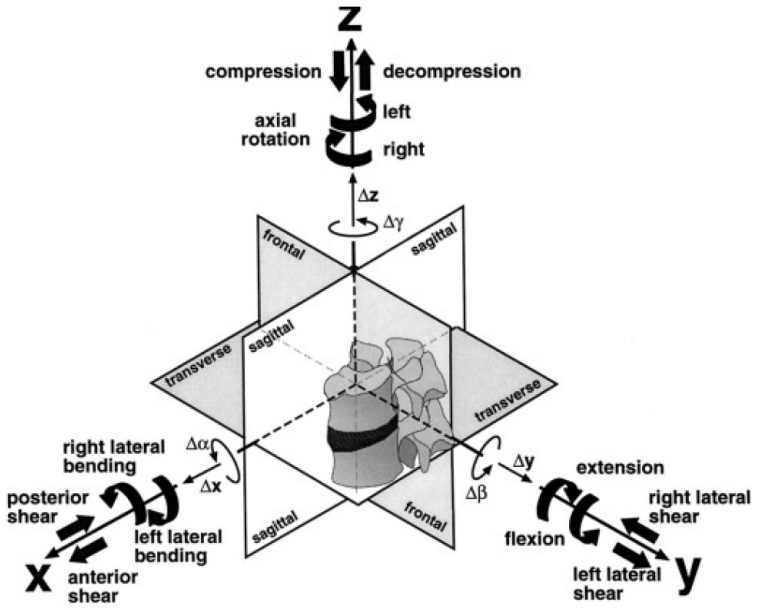

Figure 2.6: Coordinate system of the spine [157]. The arrows of the motion components $\Delta\alpha$, $\Delta\beta$, $\Delta\gamma$, Δ x, Δ y, Δ z represent the positive direction. Reprinted with kind permission of Springer Science and Business Media.

A Cartesian coordinate system with three orthogonal axes, right-handed, is described by Wilke [157] and shown in Figure 2.6 in order to define an international testing criteria for spinal implants. The global coordinate system shall lie in the middle of the underside of the lower mounted end of the specimens.

With an appropriate coordinate system the following loads can be defined: lateral bending along the frontal plane corresponds to a moment about $\pm X$ axis; flexion/extension (lateral shear along the sagittal plane) is a moment about $\pm Y$ axis; an axial rotation corresponds to a moment in $\pm Z$ axis. Forces along $\pm X$, $\pm Y$ and $\pm Z$ axes describe anterior/posterior shear, left/right shear and distraction/compression forces respectively. When using moment loading in the lumbar spine, an amplitude of $\pm 7.5\,\mathrm{Nm}$ is suggested; for the thoracic spine, $\pm 5\,\mathrm{Nm}$; for the cervical spine, $\pm 1\,\mathrm{Nm}$ at C1-2 and otherwise, $\pm 2.5\,\mathrm{Nm}$ [157].

The neutral zone (NZ) is defined by Panjabi [121] as the region of intervertebral motion around the neutral posture where little resistance is offered by the passive spinal column. In [157] Wilke defines it as the measurement of the laxity of the spinal specimen. It describes the range over which the specimen moves essentially free of applied loading. It is the difference between the angles at zero load between the two phases of motion.

In material science the elastic region is defined as the portion of the curve (in a stress-strain curve) where the material will return to its original shape if the load is removed. In spinal test it is defined as the deformation measured from the end of the neutral zone to the point of maximal loading.

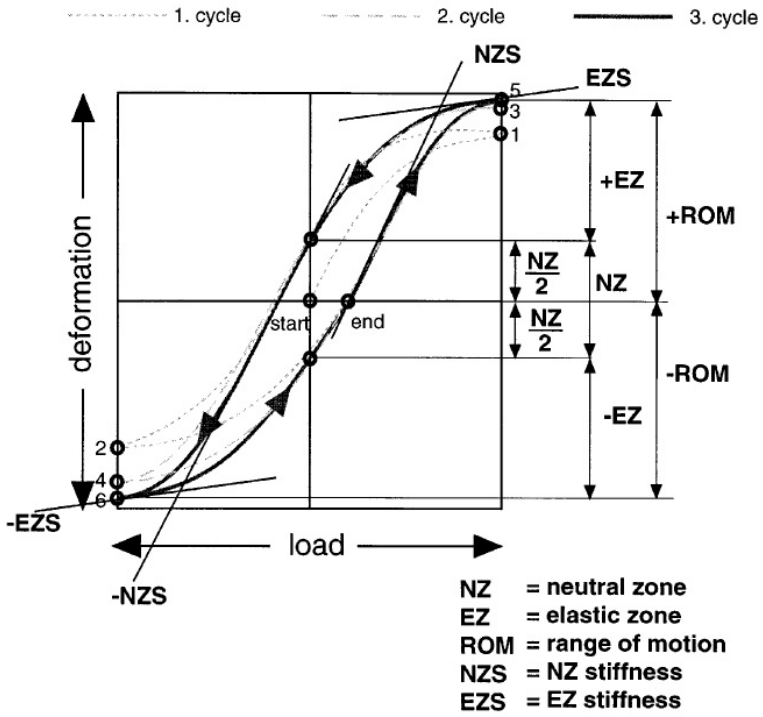

Figure 2.7: Load-displacement curve where 3 cycles are described [157]. Reprinted with kind permission of Springer Science and Business Media.

The neutral zone stiffness (NZS) and the elastic zone stiffness are the stiffness characterizing the relatively lax deformation and the elastic deformation of the specimen, respectively. Figure 2.7 illustrates these concepts.

3 State of the Art

Biomechanical studies are nowadays accomplished with the help of computers and machines. In order to analyze in depth a human joint it is necessary to describe its biomechanical properties, forces, degrees of freedom, axes of rotation, configuration of ligaments, geometry of the surfaces, friction, etc. A human joint is much more complex to describe than a simple rigid structure since it involves more than one homogeneous structure. The usage of robots in these kind of analyses has become essential in order to accomplish specific experiments that fulfill the required complexity. Current applications use robots to apply forces, moments and displacements in human joints. These kind of systems allow to test bones, joints, soft tissues, artificial joints and other biological specimens.

These experiments are usually too complex because every human joint is different. Their constraints, ROM, stiffness and other properties vary in every case. Due to these features, special machines have to be constructed. A system composed by a robot to perform biomechanical experiments provides high flexibility to test different joints (e.g. knee, hip or shoulder) without changing the construct or architecture. Specifications, constants in the control loop and initial and final conditions have to be set.

Different spine testers have been developed and described in the literature. The load on the specimens can be produced by robotic arms [60, 143], Stewart platforms [62, 141] or other complex systems [59, 63, 132, 154]. These machines allow the application of loads in more than one degree of freedom. Forces and moments may be applied separately or combined in different spatial axes. Thus it is possible to create a protocol where the specimen can be tested in order to describe its properties.

The use of robotics may provide advantages in the protocol to test specimens allowing the movement and control of 6 degrees of freedom (DoF). A very accepted method to test biological spines described by Panjabi [119] consists in an applied rotation about a specific axis on the body while five remaining DoFs are left unconstrained.

In this section are described the systems that several groups developed in order to perform these complex biomechanical tests.

3.1 Spine Testers

In order to carry on *in vitro* experiments with spines, different machines have been created. Gilbertson [60] used a 6 DoF robotic manipulator Unimate, PUMA model 762 with a 6 DOF force moment sensor UFS (UFS Model 4015A100-U760 JR3) in order to test a lumbar spine (Figure 3.1). He used a hybrid control and a similar algorithm from Fujie [46]. The loads can be applied in the spine separately or in combination, resulting in an unconstrained 3-dimensional displacement (translation and rotations). The parameters of the spine that can be determined are the flexibility and stiffness coefficients, properties that are very

useful for characterizing the biomechanics of the intact, injured and stabilized spine. The sensor mounted in the TCP has a full-scale force capacity of $\pm 445\,\mathrm{N}$ in X and Y axes and $\pm 890\,\mathrm{N}$ in Z axis, and a full-scale moment capacity of $\pm 50\,\mathrm{Nm}$ in all axes. Gilbertson gave information of the duration of the test and found that for passive flexion/extension the system moved 1° per minute. Other forces and moments that were not commanded (nonsagittal force and moments around Y and Z axis in this case) were not explicitly controlled. The minimization of the controlled forces were between ± 6 N, while the residual axial rotation and lateral bending moments varied between $\pm 1\,\mathrm{Nm}$.

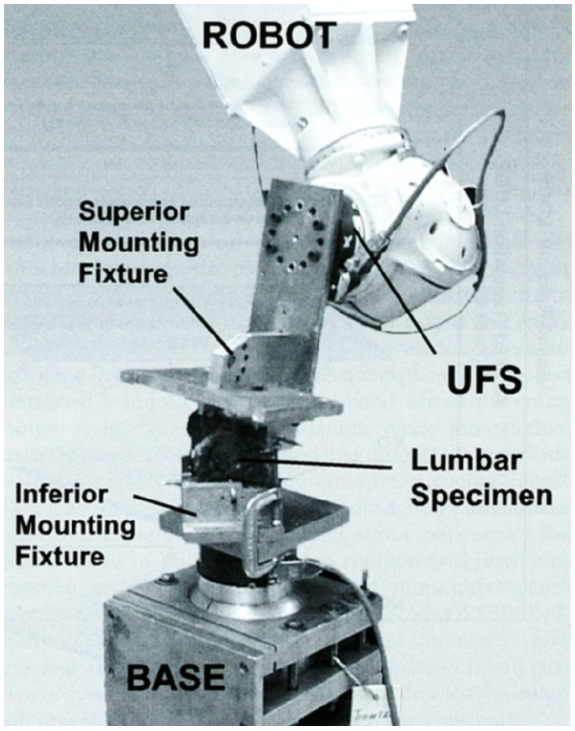

Figure 3.1: Spine tester from Gilbertson. Reprinted from [60], with permission from Elsevier.

Lysack [101] developed an apparatus in order to apply pure moments to spine specimens (Figure 3.2). This machine allows continuous cycling of the spine between specified flexion and extension maximum load endpoints and uses the concept of deadweights and cables acting about pulleys in order to produce force couples. Hysteresis curves can be generated and analyzed for different spinal constructs. The use of continuous loading permits the analysis of the spine's behavior within the neutral zone. This machine produced continuous angle-moment data for the entire range of motion of the spine including the neutral zone. It can produce a maximum moment of 28 Nm at a loading frequency of 0.5 Hz. In order to quantify the relative angles of the movement of the specimen he uses Cardan angles. The moments are generated with an electromechanical linear actuator (Model B8.5-T2-23S1, Dynact Inc., San Jose CA). The limitations of this machine are encountered when testing very long or unstable spine specimens. In these cases, the off-axis moments may increase substantially.

Wilke [154] developed a machine in order to determine the quasistatic, three-dimensional, load-displacement characteristics of spines including simulated muscle forces (Figure 3.3).

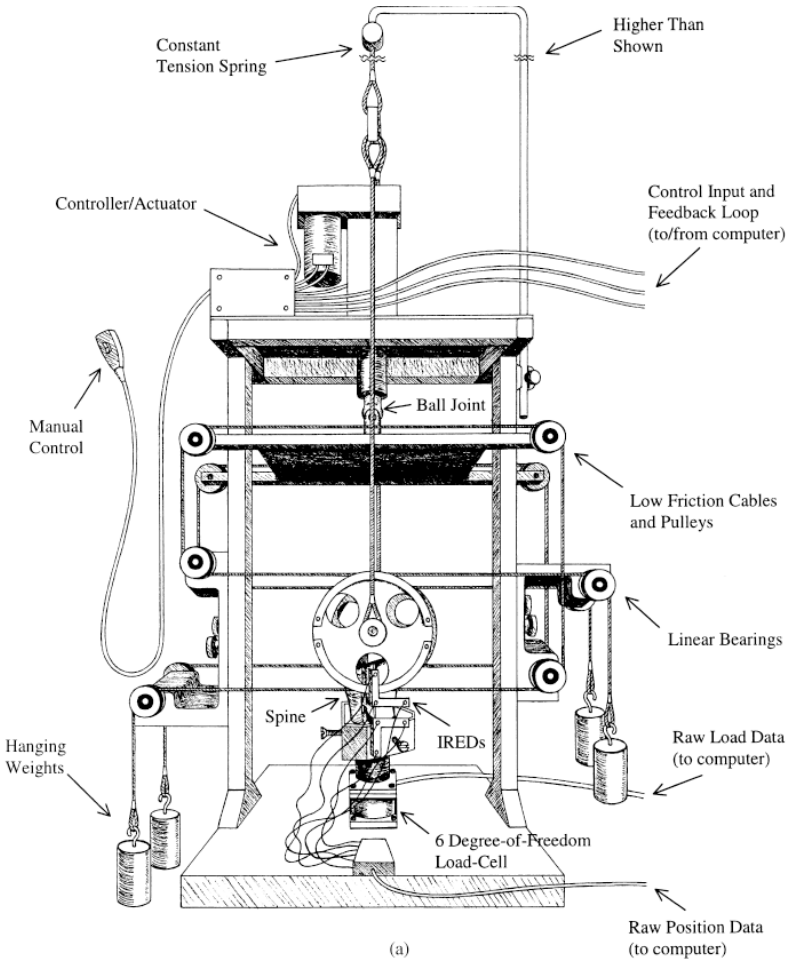

Figure 3.2: Spine tester from Lysack. Reprinted from [101], with permission from Elsevier.

Three force and three moment components can be applied in either direction individually or in combination and all of them are computer-controlled. The spine can move in all 6 DoF. Maximum lateral translation of the machine is up to 225 mm, up to 250 mm in axial translation and up to 750 mm in anterior or posterior translation, all with a resolution of 0.025 mm. The height of its portal can be adapted to a specimen of length up to 800 mm. The size of the machine is 700 x 1000 x 2000 mm (with x length x height). A cardan joint allows lateral rotation up to ±90°, any axial rotation and up to ±45° in flexion/extension. The machine allows continuous as well as stepwise load and unload cycles with changing directions. The measuring range of this load cell is for the forces F_x, F_z = 500 N and F_y = 1500 N, and the moments M_x, M_y, M_z = 40 Nm. The muscle forces are introduced by cables attached with screws to the insertion points. Each cable represents a muscle group. The forces in the cables are controlled by a pneumatic system.

Schmölz in [132] and Knop [87] used a 6 DoF spine simulator (Figure 3.4) where the clamped specimens can be loaded with variable pure moments in three directions of motion. The system is actuated with stepping motors and movement deflections recorded by an object tracking system based on magnetic field technology. The measuring accuracy involves an error of 0.1° and 0.1 mm. Additional error of a variety of instrumentation set-ups were of 2%.

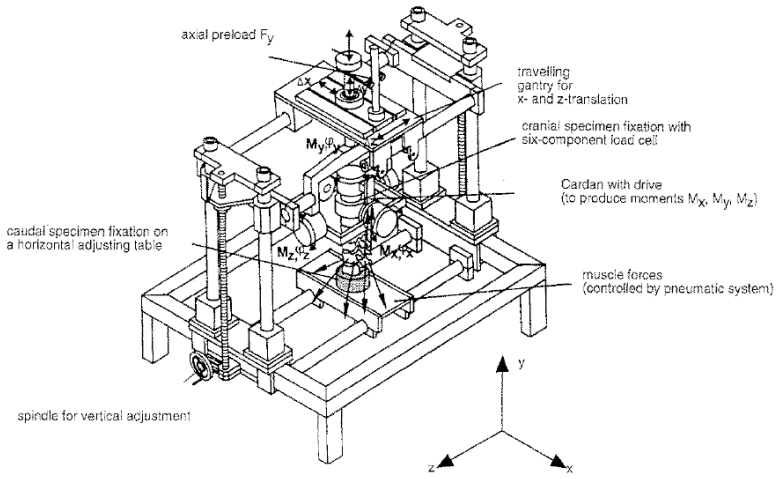

Figure 3.3: Spine tester from Wilke [154]. Reprinted with kind permission of Springer Science and Business Media.

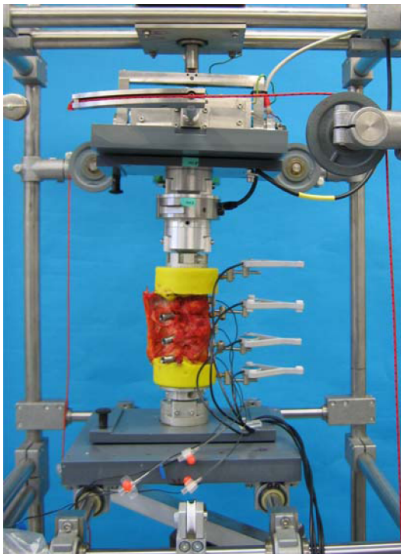

Figure 3.4: Spine tester from Schmölz [132]. Reprinted with kind permission of Springer Science and Business Media.

Thompson [143] used a 6 DoF robot Kawasaki PH260 to define the neutral zone of intervertebral joints (Figure 3.5). Force data acquisition was achieved using a JR3 50M31 FTS which can determine 3 forces and 3 moments in a three-dimensional space. The robot was controlled under position control in order to load the specimens with specific moments about different axes. The centers of rotation for movements were taken from published studies. For all tests each specimen was moved three times through its full range of movement about its unique IARs. This information was also taken from the literature.

Gèdet [59] developed a spinal loading simulator were bending moments about three anatomical axes can be applied using brushless motors (Figure 3.6). The specimen is mounted under a cardan frame. The flexion-extension and lateral bending axes are

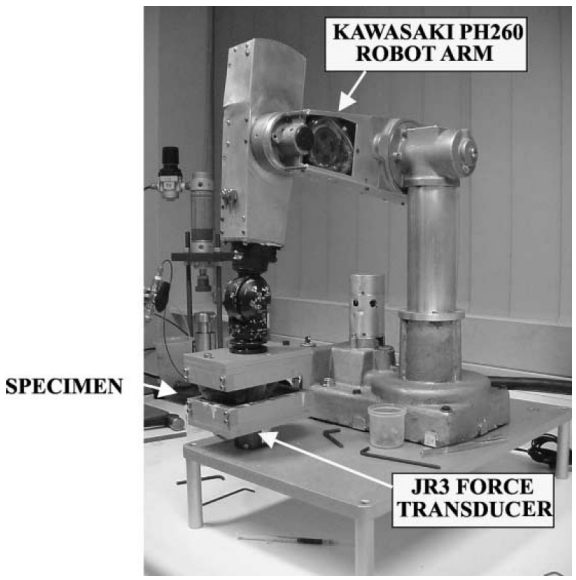

Figure 3.5: Spine tester from Thompson. Reprinted from [143], with permission from Elsevier.

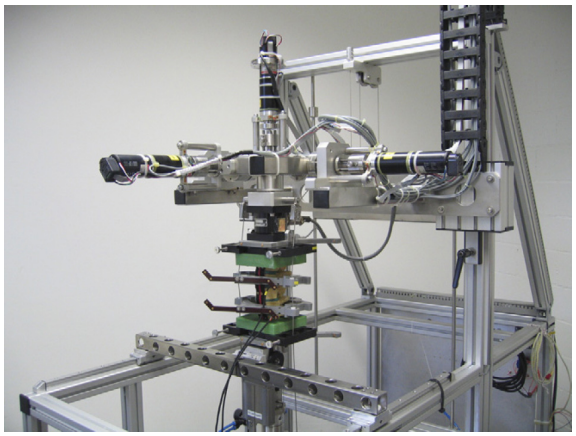

Figure 3.6: Spine tester from Gèdet. Reprinted from [59], with permission from Elsevier.

counterbalanced. The specimen is supported from above by the machine frame and fixed below to a linear slider where linear translation is free. They can be tested with or without dynamic axial compressive loads. Forces and moments are recorded by a 6 DoF load cell (MC3A 1000, AMTI, Watertown, MA, USA). Motions are calculated with an optoelectronic motion analysis system (Optotrak 3020). Gèdet says that one potential source of error in the kinematic analysis comes from the friction. These components in translation are not directly driven. In order to allow reproducibility a polymer tube was used to perform the experiments.

A Stewart platform (hexapod robot) was used by Stokes [141]. This platform can move a specimen in a 6 DoF (Figure 3.7). The joints can move through stepper motors coupled to precision lead screws. Six linear encoders were used to measure and control the displacements of the testing machine. A motion controller can drive the hexapod under

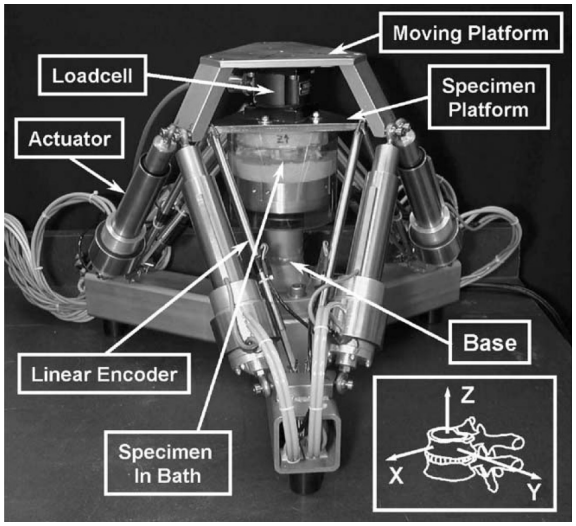

Figure 3.7: Spine tester from Stokes [141].

closed-loop position control. Length changes in the actuators were programmed to produce rotations and translations about any arbitrary axis system. Each displacement test consisted of five cycles in which the position was ramped at a constant rate. The computation of force and moments at the vertebral body were accomplish in post-processing.

A spine simulator was developed by Goertzen [63] where an articulating arm applied moments to the specimens. Two lightweight universal joints were attached to the end of a ball spline. The ball spline allowed linear translation of the arm while transmitting the moment from the motor to the specimen. A torque measuring load cell was used (TRT-200,

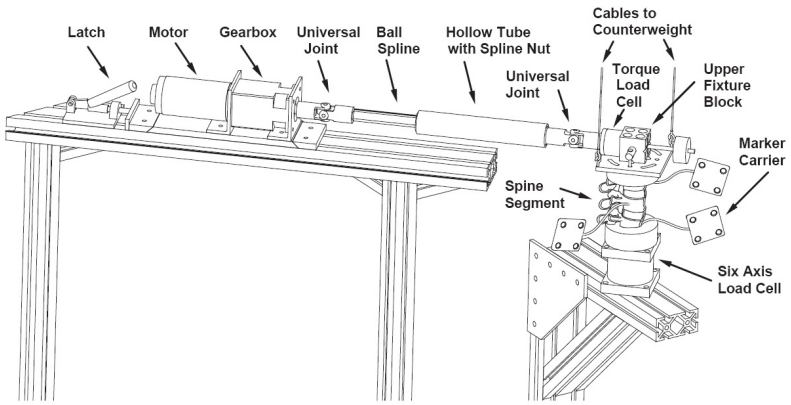

Figure 3.8: Spine tester I from Goertzen. Reprinted from [63], with permission from Elsevier.

Transducer Techniques, Temecula, CA). This configuration allowed an applied moment, 1 DoF, and the other 5 DoF were left unconstrained. A XY translation device allowed a counterweight to follow three translations of the specimen. The servo motor was controlled by motion control and was capable of either angle or torque controlled testing.

In [62] Goertzen presents another application of a velocity-based force control routine used for robotic biomechanical testing where a Stewart platform (R-2000 Rotopod, Parallel

Robotic Systems Corporation, Hampton, NH) was used (Figure 3.9). Forces and moments were acquired with a six-axis force-moment sensor (AMTI MC3A-6-1000 Advanced Mechanical Technology Inc., Watertown, MA). Two fixtures were attached to the specimen. The upper fixture was mounted to a cross beam. The lower specimen fixture was mounted

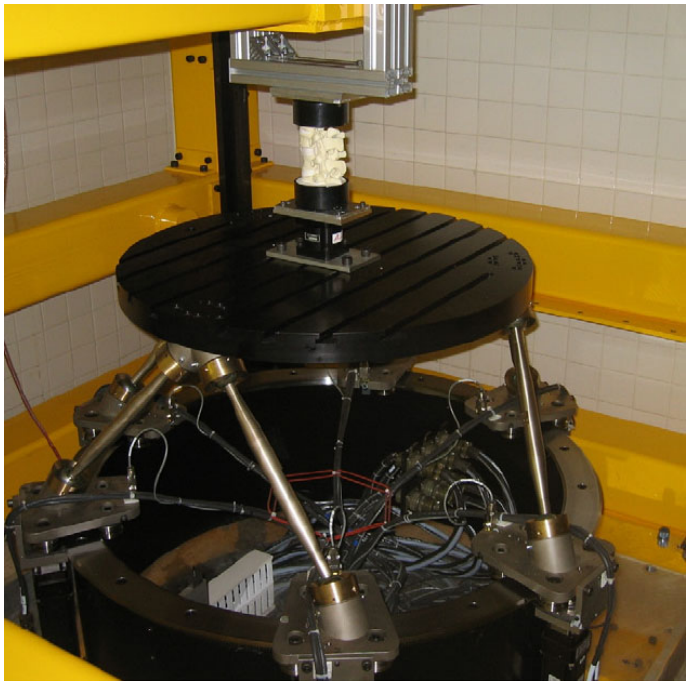

Figure 3.9: Spine tester II from Goertzen. Reprinted from [62], with permission from Elsevier.

on the six-axis load cell which was attached to the robot platform. The basis for the force control is a command (JogVector) provided by the robot manufacturer. The JogVector parameters were calculated in each iteration of the control loop by normalizing the force errors with a preselected force window value on each unconstrained axis. When the force error was less than the force window, resulted in a JogVector parameter that reduces the velocity as force errors approach zero. The frequency of the controller was reported as 20 Hz. The force window parameters were determined *a priori* in a tuning process. Tracking errors on the unconstrained axes were less than 1 N and 0.05 Nm for a flexion-extension moment of 0.27 Nm.

Table 3.1 contains a summary of all works where a machine was developed in order to test spines. These works use different mechanical methods in order to apply forces and moments. Data in brackets are supposed by our group but the author did not give any information.

3.2 Discussion

All research groups presented here use a specific kind of control in order to applied loads, however not all give information about it and also there are lacks in the information about the control frequency. It is supposed by our group that the spine testers developed by

Table 3.1: Summary of machines to test spines

Author	Spine Tester	Control	Controller Frequency
Gilbertson	Puma 762	Hybrid control	(100 Hz)
Lysack	Pulleys and electro-mechanical linear actuator	No data	No data
Wilke	Stepper motors and pneumatic system	No data	No data
Schmölz	Stepper motors and pulleys	No data	No data
Thompson	Kawasaki PH260	(Position control)	(100 Hz)
Gèdet	Brushless motors	Position control	No data
Stokes	Hexapod robot	Position control	No data
Goertzen I	Articulated arm	Position control	No data
Goertzen II	Hexapod robot	Velocity control	20 Hz

Lysack, Wilke and Schmölz work under the concept of rotating a single axis of a motor until a predefined force or moment is measured. This control approach is called position control.

Previous experiments with serial robots and hexapods make use of FTS in order to measure the load applied on a specimen. The hybrid control used by Gilbertson is for biomechanical tests slow (1° per minute) and the stability can be ensured only under special conditions and previous knowledge of the specimen and coupling properties with the manipulator (e.g. geometry, stiffness, kind of contact, velocity compliance of both robot and specimen [2, 3, 166, 167]). The velocity reported in his experiments has to be considered due to decomposition process of biological specimens.

Stokes and Thompson use a robot (hexapod and serial respectively) under position control. The main disadvantage of this architecture is that the trajectory in position-orientation coordinates must be known in advance to ensure proper movements of the robots. These parameters are very specific for every joint. They depend on many factors like patient age, health, weight and height, time of storage of cadaveric specimens, and much more. The model of the manipulator to test biological specimen can be calculated with enough precision but a detailed description of the particular specimen is difficult to obtain. In such cases the usage of a mere position control for controlling not just interaction but also the magnitude of the load is a candidate to fail.

Another disadvantage is that a pure force/moment control has not been implemented with these kind of robots for biomechanical goals. The groups using a hexapod apply the load indirectly through the position or velocity and stop the movement when the desired force or moment has been reached. This can provide high velocities of the robot and reduce the time of the experiments but it also reduces the sensibility to react to the natural forces that arise in the specimen. A characterization of the ROM will be corrupted when using a spine tester controlled under position or velocity control due to the reasons given before.

Other machines apply a moment or a force and with the help of a linear slider it is possible to avoid forces in the two-dimensional plane where it moves [59, 63]. There are two big disadvantages with such setups. The first one is that the linear slider is not frictionless and therefore forces arise while testing. These forces and moments are very difficult to measure accurately. Due to this, constraint forces and moments will be present in the measure. Other disadvantage is that these constraint forces are not controlled but passively avoided. The application of a pure moment in a rigid body is only theoretically possible. In a finite element analysis it is easy to demonstrate that the sum of all internal forces in the body is zero but not the moment. It is only possible to induce a moment about an axis and to minimize forces and torques in all others.

It is assumed that the groups using a serial and hexapod robot are working with the commonly used sampled rate of 50/100 Hz. This parameter is important for the stability and robustness of the controller when testing, specially when force/torque control is applied.

None of the described works use a direct force control. Many research groups have investigate the stability of interaction control in oder fields [66, 83, 167] but it is still a high complex problem. In order to apply this kind of interaction control to load biological specimens with specific forces and moments in chosen axes, it is mandatory to develop a robust controller with a high frequency in order to ensure the stability of the whole system (e.g. avoidance of vibrations, unstable behaviors with different properties of the specimens like stiffness).

4 Concept

In order to develop a high-performance 6 DoF biomechanical joint analysis system based on an industrial robot it is necessary to interconnect specific components and to develop a modular architecture where priority tasks and modules are programmed. The robotic system may be thought of an universal testing machine that can apply loads in a 6 DoF environment. The system should be able to apply any force or moment, single or in combination, in any direction or around any axis. Thus the specimens are free to move in the 6 DoF. Covering these points the machine would be able to perform high complex tests of anatomical specimens in order to provide valuable information about their kinematics, dynamics and quantification of their physical properties.

The demands that such system should cover are described in this chapter. All components to achieve these goals are here shown. Their interconnection, design and architecture are in detail described.

4.1 System Demands

The spectrum of possible tests of such 6 DoF testing machine is very wide. The system architecture must be flexible enough to adapt itself to the demands of the different scenarios that biological tests demand. A modular design is a strategic distribution of the different tasks, depending of their role and if they are time critical or not. A modular hardware-interface expands also the flexibility and offers the possibility to change old or even add new hardware without changing the architecture of the whole system. Thus it is possible to have maintainability and scalability.

The manufacturer of the robot Stäubli RX 90-B provides the basic components (hardware and software) to design own control structures. In this way the controller can be implemented as code in the control program of the central unit with a maximum control frequency of 100 Hz. The design of a complex controller in the form of text is error-prone especially when the code is long and confusing. In addition, the implementation of robust or other architectures (e.g. hybrid controllers), which regulate the same positions, forces and moments, increases the computational effort considerably. This results in significantly longer cycle times for control and it may happen, in worst case, that the system becomes unstable and the robot may be uncontrollable.

A force control architecture demands a fast frequency in order to ensure stability and a good performance of the controller. Direct force control depends directly on the frequency of the controller due to the feedback inner loop implemented with force/torque signals. The system stability is the main concern when using this control.

The interaction with the machine should ensure safety for the user, for the specimen to test, for the environment and for the robot itself. A modular structure, together with a

strategic distribution of the modules provides flexibility for the adaptation to different sizes and kinds of specimens.

The system architecture should be flexible enough to adapt itself to the different experimental scenarios with biological specimens without requiring exhaustive changes in the internal structure. It should be constructed in a modular way in order to distribute the tasks depending on their role. A modular architecture offers a better maintainability, simplicity, flexibility and scalability. In this way, upgrading, replacing or adding a new component must not affect the basic structure of the system.

The robot should be able to move under position and under force control and a combination of both. The tested bodies can be loaded also applying certain displacements and rotations.

The time to perform the experiments is a very important parameter due to a decomposition process of biological specimens. The features of the specimen change every second that passes by. The system should be able to perform different experiments in a relative short time in order to acquire representative and suitable data. The system must be able to define a variable where the time of the experiment or the followed profile is given.

A particularly issue to be considered when thinking about biomechanical tests using a robotic system is the presence of singular configurations of the manipulator. In the neighborhood and at particular configurations an exact solution of the robot inverse kinematic becomes singular. Consequently, unfeasible joint velocities may be produced which yields into unexpected behavior of the robotic system. During the test of specimens, high velocities and position deviations can produce damage to the system, the specimen and represent a danger to the user. Therefore, another important objective of this work is to assure safety in the presence of such singular robot configurations.

The framework should be able to be operated without a depth knowledge of the system. Due to this, it is necessary the construction of a GUI where the most important parameters for the controller and for the experiment setup can be introduced avoiding also that the user modifies important variables or configuration that can damage the performance of the robot.

The system should be able to display a virtual 3D environment in order to visualize the robot connected with the specimen. This has the objective that the user can observe the scene from different angles in order to define specific parameters for a specific experiment. This virtual would should also provide a visibility of the test from a close perspective without being in the range where the robot can move. This 3D environment should be also available in simulation for planning purposes.

When working with biological specimens, the attachment of bones, muscles, tendons, ligaments and adipose tissues to the testing machine becomes a critical issue. Biological specimens are very special “materials”. They are very difficult to represent with models (e.g. in finite element theory), they have a very complex geometry, their properties are not linear, all DoF are coupled, they are anisotropic and their properties change with the time. These materials contain certain amount of fat, blood and other substances. This makes them very difficult to be attached to a mechanism. In order to perform any biomechanical test, the fixation of the biological specimen should be ensured within the whole time of the experiment.

In order to cover these demands, technical and biomechanical components should be combined and configured. In the next sections these components are described and the interconnection between them is explained in detail.

4.2 Components for Measurement, Control and Manipulation

A robot that performs biomechanical tests brings many advantages and expands the range of possible test scenarios. However, it is a high sensitive and high complex technical system. Several components should cover the demands of computation, visualization, configuration and ensure the functionality of the whole system. Different computers are specialized in different time-critical and non-time-critical tasks. Power electronics and safety for the hardware should be ensured to control the manipulator. The development programs reside in a specialized PC and the calculation of kinematics and dynamics in real time reside in other. When the tests are carried on, the robot can be a danger for the test objects, for itself and for the user. Special components and safety loops are used in order to achieve high complex tasks.

The main components to achieve this goal are:

- Robot
- Control unit CS7B
- Host PC
- Target PC
- Force-torque sensor

4.2.1 Robot

The robotic arm Stäubli RX 90-B is used in this project (Figure 4.1). The connection between joints constitute a mechanical structure that assimilates a human arm. Every part is therefore named shoulder (B), upper arm (C), elbow (D), underarm (E) and wrist (F). The basis (A) is where everything else rests. These parts are also named joints or axes: where A corresponds to joint 1, B to joint 2 and so on. The wrist is composed by joints 5 and 6. At the end of the last joint it is possible to attach special tools for specific tasks.

This structure of the robotic arm decouples the position from the orientation of the end-effector. With the joints 1 to 3 it is possible to change the position of the intersection of the rest of the joints. The orientation of the end-effector can be changed then with joints 4 to 6.

The RX90-B has two particularities:

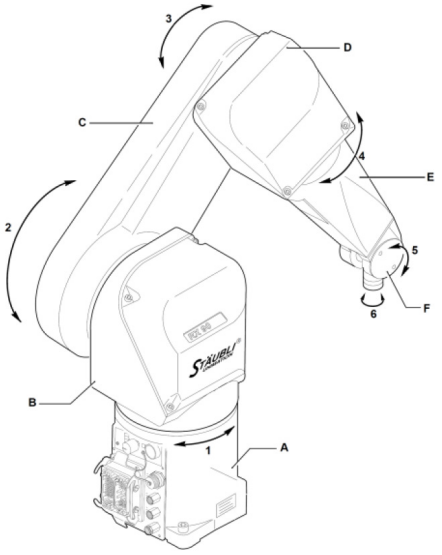

Figure 4.1: Mechanical structure of the industrial robot Stäubli RX 90-B [142].

1. High moments are naturally induced depending on the position of the manipulator due to gravitational forces and heavy links of the robot. The motor of joint 2 must apply a very high torque only to compensate these forces. In order to reduce this torque, the robot RX90-B has a spring that applies a force in an opposite direction of the movement of the joint.
2. Drives 5 and 6 have a common transmission, so that the axes of the joints 5 and 6 are coupled to each other.

Spring in joint 2

There are two clamp points to where the spring can be attached. Both points are situated in the joint 1 and one of them is excentric and over the first one (see Figure 4.2). Thus the spring elongates when the joint 2 does not stand in the zero position (vertically straight) and it brings a force in order to return it to this initial configuration.

The spring force is given by the spring stiffness k of the prestressing force P_c and the change in length of the spring Δx by:

$$F_{spring} = k\Delta x + P_c \tag{4.1}$$

Coupling in joint 5 and 6

Drives 5 and 6 have a common transmissions, so that the axes of the joints 5 and 6 are coupled to each other (see Figure 4.3). Motor 5 drives, through a worm gear, the link 5. Link 6 is mounted orthogonally to the axis of rotation 5. The drive of link 6 is actuated via a worm gear and a bevel gear whose rotation axis coincides with the axis 5.

The moments of inertia of the shaft of the engine and of the transmission can be reduced to an entire moment of inertia I_{m_i}. In addition, the three-phase AC motor can be replaced

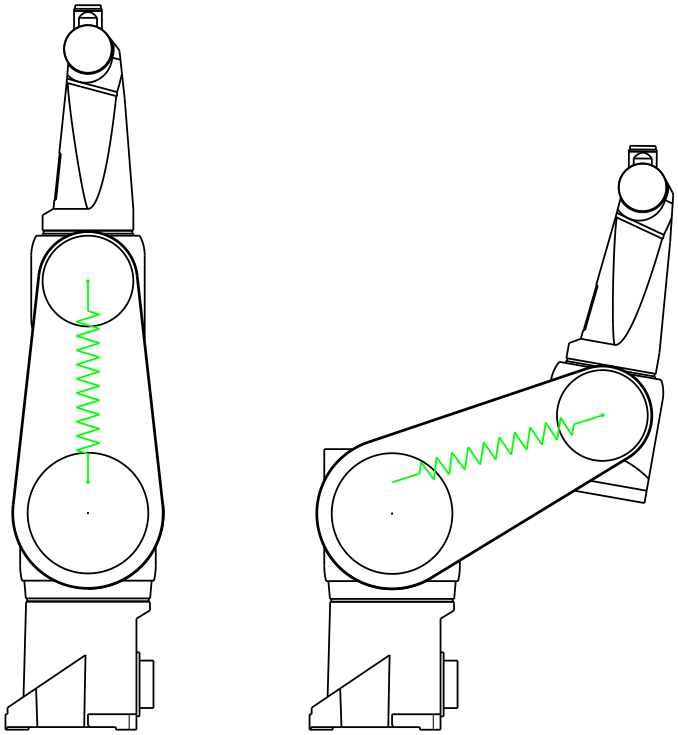

Figure 4.2: Schematic representation of the spring. The spring is attached at the points and is stretched and deflection at the second link from the zero position.

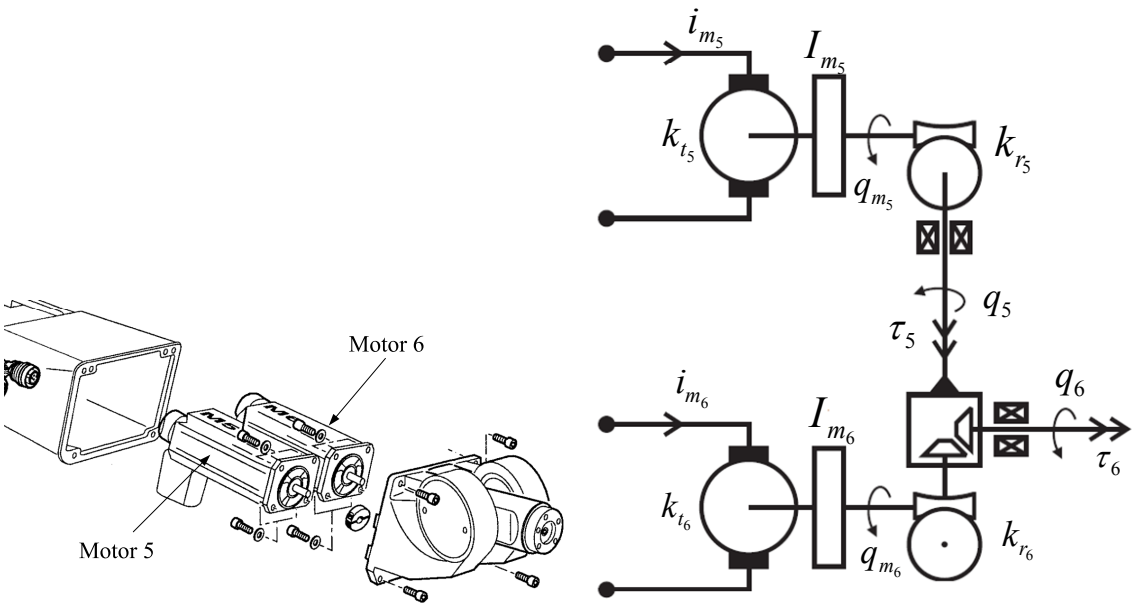

(a) (b)

Figure 4.3: a) View of the robot wrist [142]. b) Schematic representation of the drive system of the axes 5 and 6 of the industrial robot Stäubli RX 90-B.

by an equivalent direct current i_{m_i}. Furthermore, it is assumed that the engine torque is directly proportional to the motor current in the coils. The motor torque τ_{motor_i} is thus obtained from the product of the motor current i_{m_i} and the motor constants k_{t_i}. For the torques of the motors τ_{motor_5} and τ_{motor_6} the torques of the transmission output is described by:

$$\tau_{motor_5} = k_{t_5} i_{m_5} = \frac{\tau_5}{k_{r_5}} \tag{4.2}$$

$$\tau_{motor_6} = k_{t_6} i_{m_6} = \frac{\tau_6}{k_{r_6}} \tag{4.3}$$

where k_{r_i} is the gear ratio of the corresponding transmission. Neglecting friction and external forces and moments and taking into account the coupling, the following relationship can be done:

$$\begin{bmatrix} \tau_5 \\ \tau_6 \end{bmatrix} = \begin{bmatrix} k_{r_5} & k_{r_6} \\ 0 & k_{r_6} \end{bmatrix} \begin{bmatrix} \tau_{m_5} \\ \tau_{m_6} \end{bmatrix} \text{ and } \begin{bmatrix} \tau_{m_5} \\ \tau_{m_6} \end{bmatrix} = \begin{bmatrix} 1/k_{r_5} & -1/k_{r_6} \\ 0 & 1/k_{r_6} \end{bmatrix} \begin{bmatrix} \tau_5 \\ \tau_6 \end{bmatrix} \tag{4.4}$$

where τ_{m_5} and τ_{m_6} are the parts of the motor torques which are applied to the acceleration of the respective components. Taking in account the relationship between motor positions, velocities and accelerations and movements of the axes 5 and 6, the following relationships can be made:

$$\begin{bmatrix} q_5 \\ q_6 \end{bmatrix} = \begin{bmatrix} 1/k_{r_5} & 0 \\ -1/k_{r_5} & 1/k_{r_6} \end{bmatrix} \begin{bmatrix} q_{m_5} \\ q_{m_6} \end{bmatrix} \text{ and } \begin{bmatrix} q_{m_5} \\ q_{m_6} \end{bmatrix} = \begin{bmatrix} k_{r_5} & 0 \\ k_{r_6} & k_{r_6} \end{bmatrix} \begin{bmatrix} q_5 \\ q_6 \end{bmatrix} \tag{4.5}$$

$$\begin{bmatrix} \dot{q}_5 \\ \dot{q}_6 \end{bmatrix} = \begin{bmatrix} 1/k_{r_5} & 0 \\ -1/k_{r_5} & 1/k_{r_6} \end{bmatrix} \begin{bmatrix} \dot{q}_{m_5} \\ \dot{q}_{m_6} \end{bmatrix} \text{ and } \begin{bmatrix} \dot{q}_{m_5} \\ \dot{q}_{m_6} \end{bmatrix} = \begin{bmatrix} k_{r_5} & 0 \\ k_{r_6} & k_{r_6} \end{bmatrix} \begin{bmatrix} \dot{q}_5 \\ \dot{q}_6 \end{bmatrix} \tag{4.6}$$

$$\begin{bmatrix} \ddot{q}_5 \\ \ddot{q}_6 \end{bmatrix} = \begin{bmatrix} 1/k_{r_5} & 0 \\ -1/k_{r_5} & 1/k_{r_6} \end{bmatrix} \begin{bmatrix} \ddot{q}_{m_5} \\ \ddot{q}_{m_6} \end{bmatrix} \text{ and } \begin{bmatrix} \ddot{q}_{m_5} \\ \ddot{q}_{m_6} \end{bmatrix} = \begin{bmatrix} k_{r_5} & 0 \\ k_{r_6} & k_{r_6} \end{bmatrix} \begin{bmatrix} \ddot{q}_5 \\ \ddot{q}_6 \end{bmatrix} \tag{4.7}$$

4.2.2 Control Unit CS7B

Stäubli provides the robot with the control unit CS7B, which uses the hardware and software from AdeptMotion VME. The components of this control unit build a central system with power electronics, interface cards for every axis with servo amplifiers and an interface board. The CS7B serves to the administration of peripheral devices and to the calculation of the control signals. The unit control is connected with the servo amplifiers through interface cards, which control the motors. The interface cards read at their inputs the signals from the incremental encoder mounted on each motor of the robotic arm, and generates analog signals at the outputs (maximum / minimum ±10V) to control the amplifier. On the interface board run all security-related signals of the robot, so that they can be monitored by the central unit.

The control programs for AdeptMotion VME are written in language V+, which already provides some functionality for the control of robot drives. In operation, the commands from the V+ generate desired value positions for each axis of the robot and transmit them to the servo controller. The structure of the controller for every axis is already preconfigured in AdeptMotion VME. In essence, this is for PID controller with low pass

filters, whose parameters can be adjusted by the operator. The frequency range of the controller AdeptMotion VME is from 60 Hz to 100 Hz.

The outputs of the controller correspond to the desired values for the motor torque at each axis. Through digital-analog converters are these converted into analog voltage signals with values in the range of ±10 V and passed to the amplifiers of the motors. The amplifiers have special controllers, which regulate the motor current and thus the moment in the individual drives.

Each axis is analogous to an oscillating spring, mass, damper system when using the controller AdeptMotion VME. This corresponds to the desired position of the robot axis position of the mass when the spring is relaxed. The difference between actual and desired position of the robot axis is therefore equated with the displacement of the mass to the relaxed position. With the help of an engine tuning program can the spring stiffness and damping be set through the parameters of the controller. These correspond to the vibration system of every axis of the robot.

4.2.3 Host

The host computer is where all non-real-time applications are running. It contains all not deterministic tasks. It communicates with the target computer through Ethernet. Here belong all high level applications that are not time critical like GUI, visualization and parameters configuration. The host is responsible for receiving data coming from the target to be displayed and saved. Its operating system is Windows XP SP2. The following programs are installed in the host:

- MATLAB & Simulink with special toolboxes
- LabVIEW
- Blender
- Virtual computer
- AdeptMotion V+
- Visual Studio C/C++ Compiler

The design of the controller, equations of motion, kinematics, dynamics and all calculations related to the manipulator are programmed in the development environment MATLAB & Simulink. With the toolbox xPC Target and using the Visual Studio compiler C/C++ is possible to convert all these programmed applications in code that will be compiled and downloaded onto the Target computer.

The GUI running in LabVIEW and all its attributes and settings can be here programmed. The GUI runs also in this computer.

A virtual world in 3D runs in Blender. This visualization is in this PC programmed and can be changed and started.

A virtual computer is in the host PC installed where the operating system Windows 98 is running. Here is installed the AdeptMotion software in order to build a connection between

the control unit and the program V+. This allows the usage of the original controllers and instructions to move the robot.

4.2.4 Target

High determinism is a feature of real-time systems and guarantees that the calculations and operations occur in a defined time step. Deterministic applications are valuable for their reliability in consistently responding to inputs and supplying outputs with very little jitter.

The operating system of the target is xPC Target. Here are all tasks that are time critical. The control loop and safety monitoring are considered as time critical because both need to be executed on time to ensure accuracy and safety for robot, user and environment. This process involves the calculation of the kinematic (direct and inverse) and the dynamic of the robot.

This real-time computer has several interface cards with analog outputs to generate signals in the range of $\pm 10\,\mathrm{V}$ and generates the input signals for the servo amplifiers of the motors. It reads also the signals from the incremental encoders and from the force and torque sensors. Thus it is possible to develop own controllers which are much faster and robust than the one delivered from the manufacturer Stäubli.

4.2.5 Force-Torque Sensor

The sensor JR3, Inc., USA can measure in the three spatial axes, forces, moments of linear and angular accelerations. Altogether there are 12 DoF:

- 3 forces: F_x, F_y, F_z
- 3 moments: M_x, M_y, M_z
- 3 linear accelerations: L_x, L_y, L_z
- 3 rotational accelerations: R_x, R_y, R_z

The sensor is designed for a maximum force of $\pm$ 200 N, maximum moment of $\pm$ 20 Nm, and maximum accelerations of up to $\pm$5g. Table 4.1 shows the maximum load in each axis. The maximum loads describe the limits of the usable measuring range in which the sensor

Table 4.1: Maximum loads in every axis of the FTS.

Axis	Maximum load
F_x	1245.93N
F_y	1201.43N
F_z	5028.21N
M_x	93.81Nm
M_y	107.37Nm
M_z	79.12Nm

provides meaningful measurements. The sensor should not be uniaxial loaded with more than than 222 N in the X and Y axis and not more than 444 N in the Z axis. Moments greater 20 Nm should be avoided.

Shocks and impulsive loads, can be tolerated by the sensor up to a certain degree. However, if the maximum loads from Table 4.1 are exceeded, the sensor must be recalibrated. In worst case it can cause permanent damage to the sensor. The Z axis may be loaded up to 11 times their maximum force with no grave consequences. X and Y axis can resist up to 5 times it maximum force. Moments, which are about 4 times as large as the maximum moment can damage the sensor. Under multiaxial load two conditions must be fulfilled in order to prevent damage to the sensor (JR3, 2007):

$$\frac{F_x}{1512.91} + \frac{F_y}{1824.39} + \frac{F_z}{5028.21} + \frac{M_x}{93.81} + \frac{M_z}{79.12} \leq 1 \tag{4.8}$$

$$\frac{F_x}{1245.93} + \frac{F_y}{1201.43} + \frac{F_z}{5028.21} + \frac{M_x}{186.49} + \frac{M_y}{107.37} + \frac{M_z}{79.12} \leq 1 \tag{4.9}$$

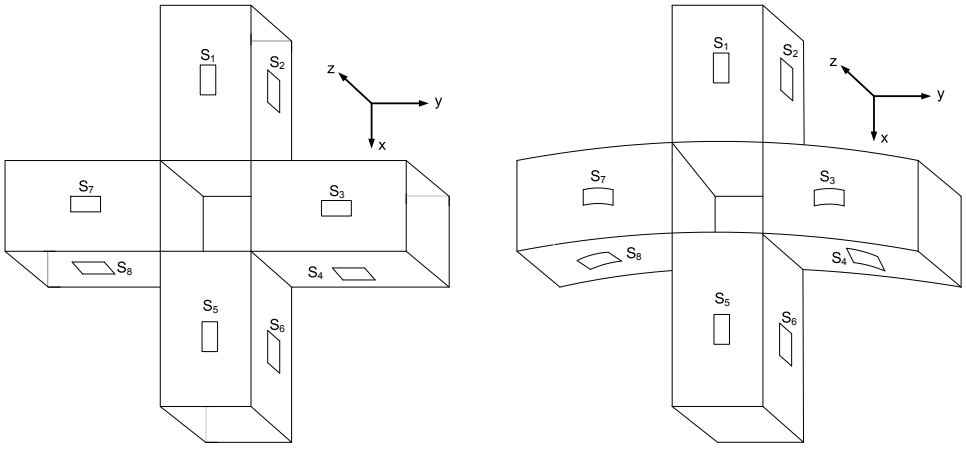

Figure 4.4: Arrangement of the strain gages in sensor. a) Sensor without strain. b) Sensor under strain.

By means of 8 strain gages attached to a cross, 3 forces and 3 moments can be measured. The strain gages provide signals proportional to the deformation of the body where they are attached. With the combination of all these 8 gages and a calibration matrix is possible to convert these signals related with the strain into force and moment. The structure of the sensor is shown in Figure 4.4. Here is important to note that with this kind of sensor it is not possible to measure force and moment in a direct way. The sensor has also accelerometers in order to provide an extra signal with three rotational and three linear acceleration independent from the strain gages signals.

4.3 Components for Biomechanical Tests

The system consists not only of the robot to exert the forces and moments to load the specimen, but also of all those components that ensure the fixation of the biological joint

and at the same time allow the free movement of it in 6 DoF. The constituent elements are:

- Resin
- Vise
- Low friction linear slider
- Tool

4.3.1 Resin

In the division of biomechanics a polyurethane resin of the company RenShape with the description "RenCast FC 53" was used to embed all biological specimens. It is composed of an isocyanate and polyol which mixture is one-to-one in weight. The mixture of both fluid components creates a chemical reaction where its viscosity will increase producing an exothermic reaction. After approx. 30 or 40 minutes the resin is completely hart and can be processed. In Table 4.2 are shown the properties of the RenCast.

Table 4.2: Physical properties of the RenCast FC 53

Demoulding time	30 to 40 minutes
Density	1.1 g/cm³
Viscosity at 25°C	80 mPa s
Compressive strength	41 to 44 MPa
Compressive modulus	1150 to 2400 MPa

4.3.2 Vise

A clamping device was used to attach the test bodies to a fix place. It is massive and has the advantage of adjust the fixation force closing or opening two jaws by a screw. However, its limitation consists in the dimension of the object to be fix. If it is bigger than the maximum aperture of the vise, the object cannot be stabilize.

4.3.3 Low Friction Linear Slider

A low friction linear slider contains four linear ball bearing systems which ride on linear rails allowing a free movement in 2 DoF. Two linear ball bearings can slide on two rails allowing the movement in one dimension. Two more rails are attached on this first construction and the linear ball bearings are positioned parallel to the first ones. In this way, and by superposition, a two dimensional low friction linear slider is developed.

4.3.4 Tool

A robotic tool is a device to perform a specific work. A tool can be designed to weld, paint, handle dangerous material, and many other applications. The tool is the physical interface between robot and environment. In this project it serves as the connection between robot and specimen. A bracket was used to attach the FTS at one side and the resin holding the specimen at the other. This 90° connection of the bracket facilitates the insertion of screws to fixate the tool to the FTS and to the resin. It has also the advantage of positioning the robot at the side of the biological components avoiding a singular configuration in the manipulator.

4.4 System Architecture

Due to the limitations already described of the control structure in AdeptMotion VME and low cycle time when using the manufacturer components, an alternative approach to control the robot was chosen. The controller that calculates the required motor torque will be on a powerful computer with a real-time operating system which provides flexible and high frequency control possibilities. This real-time computer has an interface card with analog outputs in order to generate signals in the range of $\pm$10V and is thus able to generate the input signals for the servo amplifiers of the motors. It is also possible that signals from the incremental encoders, FTS and other sensors be read by the real-time computer. In this way it is possible to develop an own control architecture with different control loops.

Therefore no fixed structure must be preserved. In addition, the program structures remain clearly by the graphic design and can be understood, changed and enhanced easily. Furthermore, through the real-time computer is possible to achieve a cycle time of 0.5 kHz even when running complex control algorithms with high computational complexity. The technical and biomechanical components described before are interconnected as shown in Figure 4.5. 3 boards located in the control unit CS7B have the following description: VME board serves as an interface card between other boards. MI6 is a 6 channel board designed to control 6 motion axes and to read 6 incremental encoders. AWC (Adept Windows Controller) is the board which connects with the servo module, activate the brakes and runs a power down sequence.

The system architecture is divided in three main parts:

1. RT applications, mechanics, hardware and electronics
2. Non-RT applications
3. Safety
4. Biomechanical components

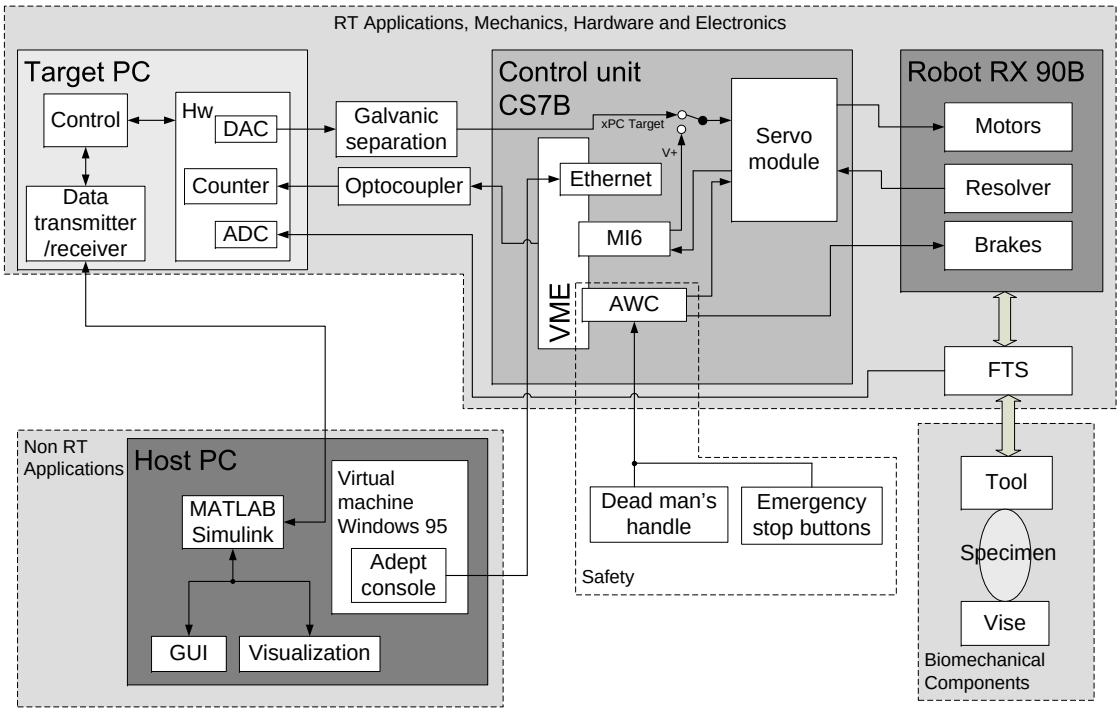

Figure 4.5: System overview where technical and biomechanical components are interconnected.

4.4.1 RT Applications, Mechanics, Hardware and Electronics

In this first part are all those components of software, hardware and electronics which response and activation is in real time. These components are in charge of producing signals to move each joint of the robot, reading the encoders in order to sense the position of every joint, computing of direct and inverse kinematics and dynamics, activating the brakes, reading the incoming signals of different sensors and achieving control loops. In this part there are two groups to be configured by the user:

- RT control: V+
- RT control: xPC Target

RT control: V+

The RT control V+ is physically located in the power unit of the robot. It consists of a servo module and an interface module. The first one produces the signals to move the joints, the second one reads the incoming signals from the resolver, converts them into encoder signals and process them to get encoder counts. With these two modules it is possible to move the robot and achieve feedback control with a frequency from 60 Hz to 100 Hz.

RT control: xPC Target

This RT control is located inside the xPC Target computer. It needs physical signals in order to calculate variables programmed in the Simulink environment. Three PCI cards are needed to accomplish this goal:

- DAC card. Generates signals to move the robot joints
- Counter card. Counts the incoming encoder signals in order to compute the position of every joint of the robot
- ADC card. Reads incoming signals from the FTS

Two electronic boards were developed:

- Galvanic separation. In this board are located isolation amplifiers in order to separate the signals generated by the DAC and the signals received by the servo module in the power unit of the robot
- Optocoupler. In this board are located optocouplers in order to separate physically the signals generated by the interface module in the power unit of the robot and the signals received by the counter card

These two boards provide electronic safety for the xPC target computer and the power unit of the robot.

With RT control xPC Target it is possible to achieve control loops with a frequency of 0.5 kHz in order to move the robot and to read signals from the FTS. The combination of all these elements makes possible the generation of an extended control with a higher frequency of operation (Interactive control - force control).

4.4.2 Non-RT Applications

Here are all those software applications which operation is not in real time. Here it is possible to develop real-time applications in a conventional PC which afterwards will establish communication with the xPC Target computer in order to perform these applications in real time. In this part it is also possible to choose the type of RT control to use either RT control V+ or RT control xPC Target. The Non-RT / applications is divided in two groups:

1. Test configuration. Here it is possible to develop all the applications that will run in real time. The following components are found in the test configuration:
    - A conventional Desktop (Workstation) PC where several applications (e.g. Blender, LabVIEW) are running
    - MATLAB & Simulink. Through a high level environment based on graphic programming language it is possible to create applications to configure special movements of the robot in order to achieve specific tests
    - Virtual machine Windows 95. It is used in order to have a console to program directly in the CPU of the unit power of the robot. Several configuration of the robot can be done through this virtual machine

2. Safety configuration. Here it is possible to configure the parameters of the safety to protect the environment or the robot during test of controllers. Unexpected movements of the robot may occur during the test of the joints e.g. $\boldsymbol{K}_I$, $\boldsymbol{K}_P$, $\boldsymbol{K}_D$ of a PID controller, maximum velocity, acceleration of joints, etc.

The graphical user interface of the test configuration is in this PC and the user is able to start-stop the test and to select different parameters. It is also possible to visualize the experiment or the movements of the robot in a 3D environment.

The software architecture is a non-real time application. In order to achieve different goals several functions of the robot are divided in tasks. All tasks are enclosed in a state machine where commands are sent to the controller in order to achieve the chosen task.

A specific decision or command can be made in two ways. The first way is commanded directly from the user and is called *user command*. He can choose between several tasks like "stop the robot", "change operational space" to "joint space controller", use "position control" or "force control", "go home" or " go to initial position". The user has the control of what the robot does.

The second way to make decisions is commanded from the task itself and is called *software command*. If the task has been completed the state machine will change automatically to *STOP* state. Thus several states can be defined in order to edit or add new tasks to the robot. All states are identified depending on its goal. In order to administrate all different possible commands and taking the right actions, like change to the right state depending on a force variable, a central decision unit called *Command Manager* is implemented. The Command Manager receives all software and user commands and depending on the last and actual states it delivers a unique signal interpreted by the state machine. The state machine will send the specific task, that the robot has to do. Safety can also be programmed here. Specific actions can be made depending on several values (e.g. velocities or forces), and when these variables exceed a preprogrammed limit the robot can execute a predetermined action. A graphical description is shown in Figure 4.6.

Some functions have high priority inside the user commanded. The state *STOP* has high priority. Even if the robot is in the middle of a task, it will stop if this state is activated no matter if it comes from the user or from the State machine itself. The tasks cannot jump directly from one to another. For safety reasons they have to pass though *Stop* state as shown in Figure 4.6.

Thus a new way to program the robot in order to achieve different and specific tasks is presented. New developers and programmers may not know what it is in the core of the architecture, but they can reach all functions based on this modular and state machine system. All what they have to change is the Command Manager and to add, change or delete states on the state chart. This simplifies the action that any GUI has to do since the only action to perform is to change the inputs on the state machine.

4.4.3 Safety

This module is in charge of stopping the robot. It can be activated via software (programmed in with V+ or with Simulink) and/or hardware (emergency stop buttons, ESB). Here it is possible to program a safety room where an imaginary box is built. If the robot exceeds

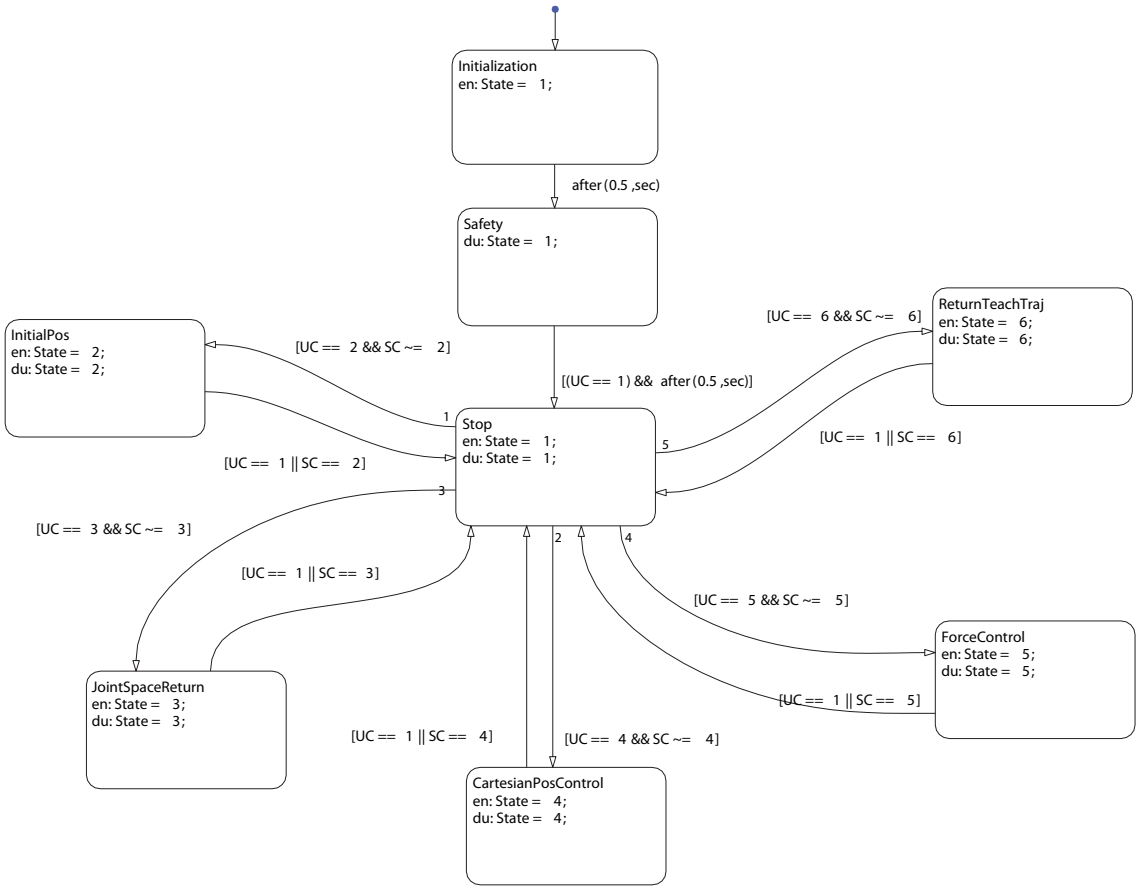

Figure 4.6: State machine where 6 States are defined. UC stands for User Command and SC for Software Command.

these borders it will stop. Another possible configuration is to define angle limits for every joint in order to protect the robot from movements that can collide with it self. If any joint of the robot exceeds its own limit, the robot will activate the emergency stop and it will remain in its last position. It is also possible to activate the emergency stop pressing any ESB or releasing the dead man´s handle. Here are also two safety interfaces:

- Dead man´s handle. If this button is pressed all the system can run. Once that that the button is released the robot will stop
- Emergency stop buttons. In case of unexpected behavior of the robot or emergency is possible to stop the robot by pressing one of these buttons

4.4.4 Biomechanical Components

The robot is used as a testing machine in order to generate specific movements to test biological specimens. To measure forces and moments a FTS is attached to the robot. In order to fix the tested body to the sensor an interface is needed. It ensures the fixation of the biological specimen. This can be a clamp mechanisms or a tool (shown in Figure 4.5) with several screws or a block made by resin. The other side of the specimen has to be

fixed to another interface or platform. This can be a linear slider, a six axes load cell or a vise. The link between specimen and platform should provide a reliable fixation. The resin “RenCast FC 53” presents several advantages and was used in order to embed all specimens.

5 Control of the Robot

There are basically two ways in control engineering to design a controller. The most frequently used method of control needs no mathematical model of the plant. Here, the controller is designed on empirical methods and tested on real systems. First, the type of controller is selected and its parameters estimated. Then the parameters are adjusted by means of experiments. The determination of the parameters is made through simple trial and error, setting rules or instructed by supporting software. Secondly, it is possible to design a controller using a model of the controlled system through analytical methods. The model here is a simplified picture of the real system, which describes the dynamic behavior as the relationship between inputs and outputs of the controlled system.

A suitable control strategy can be selected on a systematic way by analyzing the model features and then optimizing its parameters (e.g. $\boldsymbol{K}_P$, $\boldsymbol{K}_I$, $\boldsymbol{K}_D$). Unlike the first method of control, the controller is not initially implemented in the real system, but tested in simulation. This allows early identification of critical conditions and technical damage or danger to users due to inadequate controls which can be avoided. However, the model is only a simplified picture of the real system, so that the simulation results must be validated by experiments.

A method to compensate the gravitational effects of a tool attached to the sensor is needed in biomechanical tests. When the tool is attached to the sensor it reports a value different from zero. This deviation should be compensated.

In this section are described the main calculations in order to achieve the control of the manipulator. Direct and inverse kinematics are presented as well as the derivation of the equation of motion. Different control architectures to perform biomechanical tests are presented here. Results in simulation and in the real system are shown. Finally, the calculations to compensate an offset and gravitational forces/moments in the FTS is presented.

5.1 Kinematics

Kinematics is the branch of physics that deals with the motion of the rigid bodies without considering the forces that cause this motion. In robotics, kinematics plays a very important role, not only to calculate the dynamic model of the manipulator, but also as an indispensable prerequisite to motion planning, singularity analysis and conversion between spaces (from joint to Cartesian space). A serial robot consists of a number of rigid links connected with joints. The joints are normally of revolute or prismatic type in order to reduce manufacture and control complexity. They are situated in an orthogonal, intersecting joints axes and/or in a parallel way. The kinematics analysis of serial robots, consists basically of two sub-problems, the forward and inverse kinematics problems.

General methods exist to solve either the forward kinematics problem as well as the inverse one. These methods are efficient and numerically well behaved. They can be applied to robots with general geometry and any number of joints. However, they require a lot of calculation.

Although computational time and effort could be not a difficult task for modern microprocessors, numerical accuracy can be also lost. Some more elaborated numerical techniques exist to find all solution, but these demand more computational effort, which may be an inconvenient for real-time controllers.

5.1.1 Direct Kinematics

The direct kinematics finds the position and orientation of a robot's end-effector with respect to a reference coordinates system given the joint variables of the robot. The joint variables are the angles between the links in the case of rotational joints, and the link extension in the case of prismatic joints.

The creation of a geometric model for a serial robot is often on the Denavit-Hartenberg convention. The classical Denavit-Hartenberg convention provides general rules on the definition of coordinate systems on two consecutive links, and for converting coordinates between these systems [134].

With the help of the classical Denavit-Hartenberg convention a geometric model for a serial robot can be created in a systematic way. However, this method can not be used for robots with tree structure or with a closed kinematic chain. Moreover, it may seem confusing that the vector z_{i-1} coincides with the joint axis of the of the ith joint. To fix these problems, it was proposed by Khalil and Kleinfinger, a modified Denavit-Hartenberg convention [81, 82].

The resulting coordinate transformation from coordinate system i to i-1 is obtained by the matrix multiplication of two transformations as:

$$\boldsymbol{A}_i^{i-1}(q_i) = \boldsymbol{A}_{i'}^{i-1}\boldsymbol{A}_i^{i'} = \begin{bmatrix} \cos\theta_i & -\sin\theta_i & 0 & a_i \\ \cos\alpha_i \sin\theta_i & \cos\alpha_i \cos\theta_i & -\sin\alpha_i & -\sin\theta_i d_i \\ \sin\alpha_i \sin\theta_i & \sin\alpha_i \cos\theta_i & \cos\alpha_i & \cos\alpha_i d_i \\ 0 & 0 & 0 & 1 \end{bmatrix} \tag{5.1}$$

where a_i and d_i are the displacements along X and Z axes respectively. α_i and θ_i are the rotation about X and Z respectively.

The geometric model of the industrial robot Stäubli RX 90-B was created in this work using the modified Denavit-Hartenberg convention. The locations of the coordinate systems are shown in Figure 5.1. Table A.1 lists the Denavit-Hartenberg parameters for the description of transformations between different coordinate systems. $\boldsymbol{q}$ is the 6×1 vector of joint variables where $\boldsymbol{q}(\theta) = [\theta_1, \theta_2 - \frac{\pi}{2}, \theta_3 + \frac{\pi}{2}, \theta_4, \theta_5, \theta_6]^T$. In the joints 2 and 3, the angles have an offset so that the robotic arm extended to the top has a state value of $\boldsymbol{q} = [0\ 0\ 0\ 0\ 0\ 0]^T$. The homogeneous transformation matrices can be formulated according to the equation 5.1.

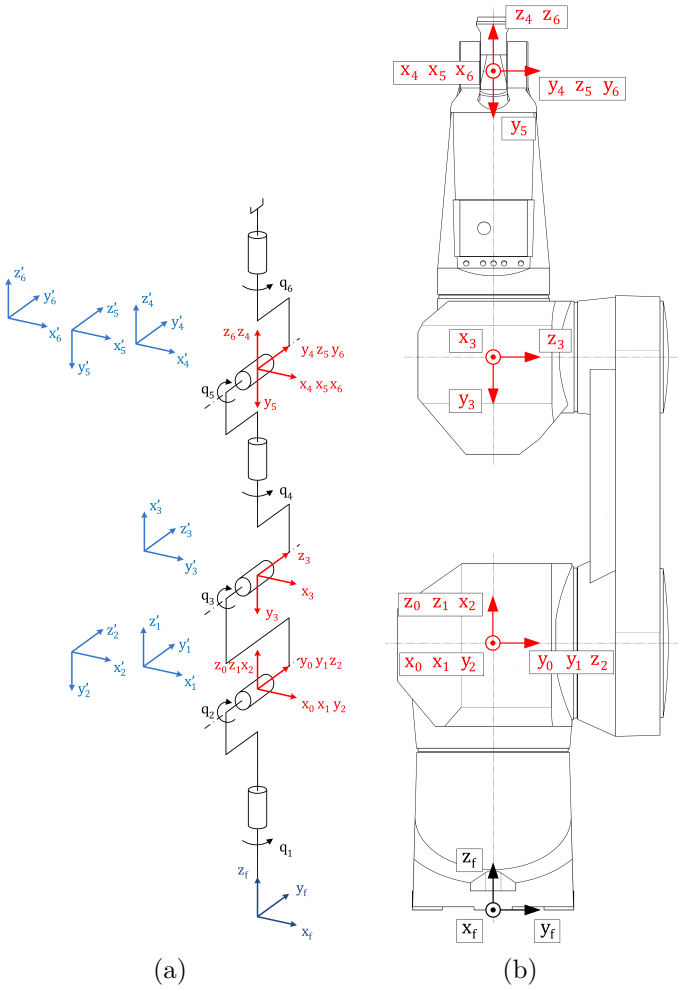

Figure 5.1: a) Kinematic scheme of the Stäubli RX 90-B industrial robot with body-fixed coordinate systems and orientation of the intermediate systems (prime symbol) as a guide. b) Illustrates the position of the coordinate systems in the industrial robot Stäubli RX 90-B.

5.1.2 Inverse Kinematics

The kinematic model of the robot describes the relationship between the angular velocities $\dot{\mathbf{q}}$ in the axes of the robotic arm and the linear velocities $\dot{\mathbf{p}}$ and angular velocities $\boldsymbol{\omega}$ of the end-effector. This relationship is expressed using the geometric Jacobian:

$$\boldsymbol{v} = \dot{\boldsymbol{X}} = \begin{bmatrix} \dot{\boldsymbol{p}} \\ \boldsymbol{\omega} \end{bmatrix} = \boldsymbol{J}(\boldsymbol{q})\dot{\boldsymbol{q}} \tag{5.2}$$

where $\boldsymbol{v}$ is the velocity in Cartesian space composed of the linear velocity $\dot{\boldsymbol{p}}$ and the angular velocity $\boldsymbol{\omega}$. $\boldsymbol{J}(\boldsymbol{q})$ is the Jacobian matrix: $\boldsymbol{J}(\boldsymbol{q}) = \left[\boldsymbol{J}_p^T \; \boldsymbol{J}_o^T\right]^T$.

The matrix $\boldsymbol{J}_p$ of dimension (3×6) herein describes the relationship between the angular velocities $\dot{q}_1 \cdots \dot{q}_n$ in the axes of the robot and the linear velocities of the end-effector,

Table 5.1: Denavit-Hartenberg parameters of the RX 90-B.

Transformation	α [rad]	a[m]	d[m]	θ[rad]
foot $\rightarrow$ 1	0	0	0.42	θ_1
1 $\rightarrow$ 2	$-\pi/2$	0	0	θ_2 - $\pi/2$
2 $\rightarrow$ 3	0	0.45	0	θ_3 + $\pi/2$
3 $\rightarrow$ 4	$\pi/2$	0	0.45	θ_4
4 $\rightarrow$ 5	$-\pi/2$	0	0	θ_5
5 $\rightarrow$ 6	$\pi/2$	0	0	θ_6

relative to the stationary base. The matrix $\boldsymbol{J}_o$ of dimension (3×6) is therefore the relationship between $\dot{q}_1 \cdots \dot{q}_n$ and the angular velocity of the end-effector.

The inverse kinematics problem consists in finding the joint variables of the manipulator given a position and orientation of the end-effector in the Cartesian space. This problem is in general nonlinear, it does not have always a closed-form solution and when it has it, the same pose may be reached by different configurations of the robot. The solution may be out of the volume range of the manipulator kinematic structure. In the case of a singular configuration or in redundant manipulators this problem may have infinite solutions. The inverse kinematics is of great importance due to the space description of the tasks (e.g. grasping, paletting, welding). They are normally stated in operational space due to the facility and intuitive way to define them. Working in the Cartesian space is more intuitive.

The solution may be found by two approaches: algebraic or geometric. Sciavicco in [134] describes these as: "Computation of closed-form solutions requires either *algebraic intuition* to find out those significant equations containing the unknowns or *geometric intuition* to find out those significant points on the structure with respect to which it is convenient to express position and/or orientation as a function of a reduced number of unknowns."

Other way than the geometric or algebraic method to calculate the inverse kinematics, is using *differential kinematics*, which gives the relationship between joint velocities and the corresponding end-effector linear and angular velocities in Cartesian space. This relationship-factor is given by the configuration dependent Jacobian matrix. Besides, it is possible to relate differential increments in the vector of joint variables ($\delta \boldsymbol{q}$) and differential increments in Cartesian space ($\delta \boldsymbol{X}$) using the resulting Jacobian. This constitutes one of the most important tools for manipulator depiction. The Jacobian is useful for finding singular configurations, analyzing redundancy, determining inverse kinematics algorithms, describing the mapping between forces in the end-effector and torques at the joints and to calculate the motion equation of the robot.

By definition, the Jacobian can be written as:

$$\delta \boldsymbol{X} = \boldsymbol{J} \delta \boldsymbol{q} \tag{5.3}$$

In addition, it is possible to write:

$$\dot{\boldsymbol{X}} = \boldsymbol{J} \dot{\boldsymbol{q}} \tag{5.4}$$

Thus, if it is desired to compute the manipulator posture in joint positions, the inversion

of the Jacobian must be calculated:

$$\dot{\boldsymbol{q}} = \boldsymbol{J}^{-1}\dot{\boldsymbol{X}} \tag{5.5}$$

This technique is independent of the solvability of the kinematic structure. However, it is necessary that the Jacobian be square and full rank. This means that this procedure will fail when the manipulator is in any singular configuration and in the vicinity of it.

In this project the method *Damped least squares* (DLS) [18, 20, 28] was chosen in order to have a solution for singular configurations of the robot. This method avoids many problems with singularities and can give a numerically stable method. The strategy is to choose values for $\Delta\boldsymbol{\theta}$ to update the joint angles. One approach to solve this is the equation:

$$\mathbf{e} = \boldsymbol{J}\Delta\boldsymbol{\theta} \tag{5.6}$$

where $\mathbf{e}$ is the desired change in position of the end-effector, $\mathbf{J}$ is the Jacobian matrix and $\Delta\boldsymbol{\theta}$ is the change in joint angles.

The DLS finds the value of $\Delta\boldsymbol{\theta}$ that minimizes the quantity:

$$\|\mathbf{J}\Delta\boldsymbol{\theta} - \mathbf{e}\|^2 + \lambda^2 \|\Delta\boldsymbol{\theta}\|^2 \tag{5.7}$$

where λ is a non-zero damping constant.

It can be shown that $\mathbf{J}^T\mathbf{J} + \lambda^2\mathbf{I}$ is non-singular. Thus, the damped least squares solution is equal to:

$$\Delta\boldsymbol{\theta} = \mathbf{J}^T \left(\mathbf{J}\mathbf{J}^T + \lambda^2\mathbf{I}\right)^{-1} \mathbf{e} \tag{5.8}$$

Thus the DLS finds a stable solution in singular configuration of the robot. However, the calculation of the inverse kinematics at non-singular configurations will diverge from a exact solution by this method. The DLS losses accuracy in the position and velocity in order to have a stable solution.

5.2 Dynamics

In order to follow a desired motion, the RX 90-B must perform a motion of its 6 axes commanded by the controller. The movement in one axis affects the forces on the drives in the other axes. The input and output behavior of the drives in each axis, which characterizes the relationships between the control signals of the motors and the movement of the robot, depends directly on the current signals.

The dynamics of a robot is the algebraic context of its motion parameters $\boldsymbol{q}$, $\dot{\boldsymbol{q}}$, $\ddot{\boldsymbol{q}}$ and its joint moments. As a basic principle, two problems can be distinguish: the inverse dynamics and direct dynamics. In the inverse dynamic problem the variables of motion of the robot are known and the corresponding joint moments given the kinematic time variables are sought. The dynamic model of a robot describes the relationship between the forces and torques of the motors and the mechanical motion of the structure. To determine the equations of motion of a robot, several methods can be selected. There are two classical methods to compute this model: Lagrange and Newton-Euler formulation. The equation

of motion can be written in the compact matrix form depending in joint space variables as [134]:

$$\boldsymbol{B}(\boldsymbol{q})\ddot{\boldsymbol{q}} + \boldsymbol{C}(\boldsymbol{q},\dot{\boldsymbol{q}})\dot{\boldsymbol{q}} + \boldsymbol{F}_v\dot{\boldsymbol{q}} + \boldsymbol{F}_s sgn(\dot{\boldsymbol{q}}) + \boldsymbol{g}(\boldsymbol{q}) = \boldsymbol{\tau} \tag{5.9}$$

where $\boldsymbol{B}$ is the square matrix of inertia, $\boldsymbol{C}$ is the square matrix of centrifugal and Coriolis forces. The viscous and Coulomb friction effects are taken into account by the matrices $\boldsymbol{F}_v$ and $\boldsymbol{F}_s$ respectively. $sgn(\dot{\boldsymbol{q}})$ denotes the (6×1) vector whose components are given by the sign functions of the single joint velocities. $\boldsymbol{g}$ is the vector of gravity, $\boldsymbol{\tau}$ is the vector of the actuation torques.

The direct dynamics problem leads to the calculation of the acceleration vector given the vectors of joint positions $\boldsymbol{q}$, joint velocities $\dot{\boldsymbol{q}}$ and joint torques $\boldsymbol{\tau}$:

$$\ddot{\boldsymbol{q}} = f(\boldsymbol{q},\dot{\boldsymbol{q}},\boldsymbol{\tau}) \tag{5.10}$$

Using equations (5.9) and (5.10), the direct dynamics can be reformulated as:

$$\ddot{\boldsymbol{q}} = \boldsymbol{B}^{-1}(\boldsymbol{q})(\boldsymbol{\tau} - \boldsymbol{\tau}') \tag{5.11}$$

where

$$\boldsymbol{\tau}' = \boldsymbol{C}(\boldsymbol{q},\dot{\boldsymbol{q}})\dot{\boldsymbol{q}} + \boldsymbol{F}_v\dot{\boldsymbol{q}} + \boldsymbol{F}_s sgn(\dot{\boldsymbol{q}}) + \boldsymbol{g}(\boldsymbol{q}) \tag{5.12}$$

ID is used to compute the actuator torques which are needed to achieve a desired motion. It is also used to identify the dynamic parameters that are necessary for both control and simulation applications. DD is used for simulation purposes. It finds out what the robot does when known joint torques are applied. The DD is calculated in all Figures where “Robot” or “Manipulator” is written.

Knowing the dynamic behavior of the robot can be of great advantage for different reasons, some of them are:

- Simulation of the robot in order to study new control strategies without been necessary to expose the real robot to unexpected behavior.
- Identification of inertial parameters of the robot, which normally are not precisely known, and in some cases even totally unknown.
- Improve robot performance by applying more advanced model-based control algorithms

ID control, computed torque and other control schemes make use of the dynamic model since it is known that their integration improves the robot performance. Unfortunately, dynamic model control systems have been hampered due to the complexity to derive the dynamic model and their high computational cost. Reduction of the model is then necessary by finding the minimum set of inertial parameters to make a satisfying approximation of the model, this enhances the computational efficiency so it can be used in real time applications.

The first approach was done based on the Lagrange formulation because is conceptually simple and systematic. Its derivation is developed in Appendix A.

5.3 Joint Space Control

Controlling the robot in Joint Space is the simplest way to control a robot manipulator. Here, no transformation between different spaces is necessary, since everything is worked on with general coordinates $\boldsymbol{q}$. That means that only a simple controller is used in each control loop. Planning trajectory in joint space is the simplest and the fastest method. It is require fewer online computations because there is no need to compute the inverse kinematics model at each update rate. It is also not affected by crossing singular configurations as well as the maximum velocity and acceleration can be determined from the actuator data sheets. The drawback is that the end-effector pose is not directly controlled, and hence, collision avoidance is nearly impossible especially when the application needs a specific motion for robot end-effector. The joint space scheme is appropriate to achieve fast motion in a free space where no specific trajectory of the end-effector is needed to follow.

5.3.1 Independent Joint Control

In order to perform a specific motion with the RX 90-B, several axes must be controlled at the same time. The movement in one axis affects the forces on the drives on the other axes. The input-output behavior of the drives in each axis, which constitutes the relationships between the control signals of the motors and the movement of the robot, depends on the current configuration of the robot arm and contains non-linearities.

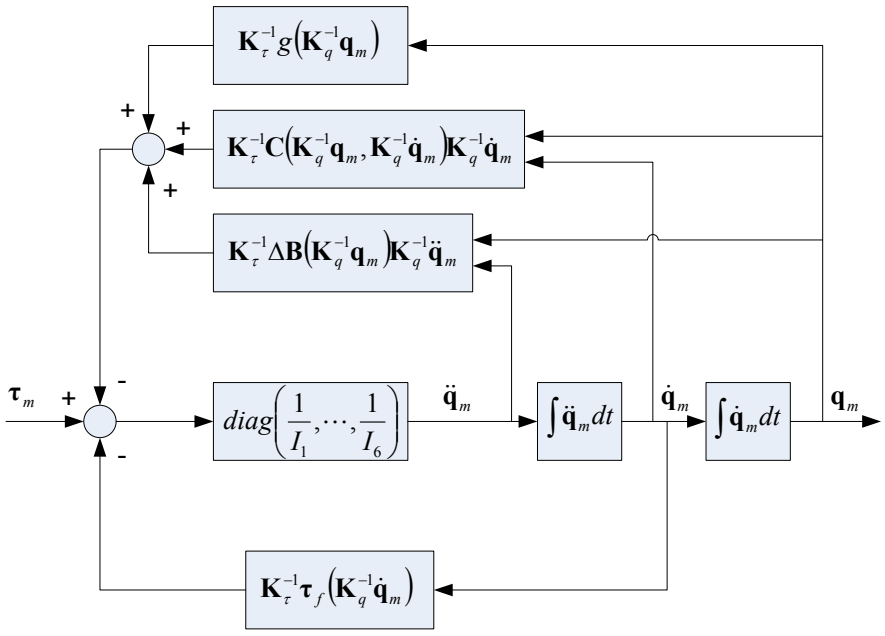

Figure 5.2: Block diagram of the drives of the RX 90-B. The individual drives are decoupled. I_i are the configuration-independent constant part of the reduced moments of inertia of the motors. The configuration-dependent terms, which describe the dynamic coupling of the robot axes, are taken as an apparent disturbing torque applied to the individual drives.

The simplest control strategy for a robot is a decentralized control. The axes of the robotic arm are considered as independent and are separately regulated. This may be controlled by using a simple PID controller. The configuration-dependent, nonlinear coupling and related effects are considered as disturbance in the individual control loops. Basically, the control parameters are determined experimentally in this approach, even without a dynamic model. However, these controllers should be tested with caution, due to high speeds and maximum power, in order to avoid damage to the robot or the environment. With this approach the robot is seen as single-input/single-output system.

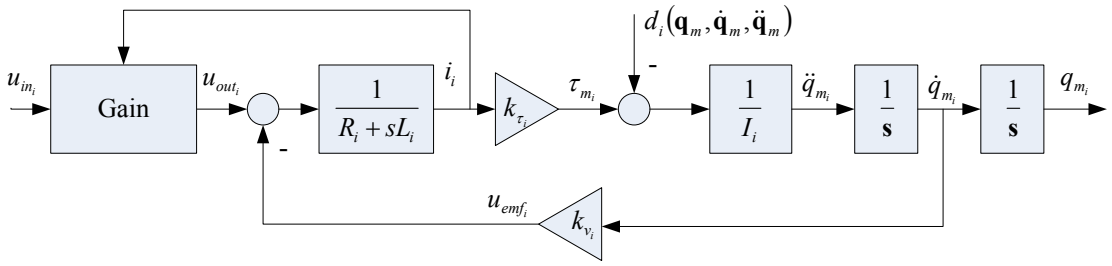

Figure 5.3: Representation of a drive for simulation with modeled servo amplifier and motor. R_i and L_i are the resistance and the inductance of the armature in the motor respectively. u_{emf} is the retroactive voltage due to the armature motion in the magnetic field. The voltage u_{emf} is calculated with the product between the rotational speed of the motor shaft $\dot{q}_{m_i}$ and the motor constant k_{v_i}. k_τ is the torque constant of the motor. The inductance L_i is generally very small and in the model of robot actuators can be neglected.

IJC is a control architecture where all joints of the robot are considered as independent from all others. The coupling between joints is here taken as a disturbance for the controller as shown in Figure 5.2, where $\boldsymbol{q}_m$ is the vector of joint variables of the motor (and not of the link). $\boldsymbol{K}_q$ is the reduction gear ratio matrix. This matrix relates $\boldsymbol{q}$ with $\boldsymbol{q}_m$. $\boldsymbol{K}_\tau$ is the reduction gear ratio that relates the vector of joint torques $\boldsymbol{\tau}$ with the vector of motor torques $\boldsymbol{\tau}_m$. $\boldsymbol{\Delta B}$ is the part of $\boldsymbol{B}$ that depends on the configuration of the robot (all those terms that are configuration dependent). $\boldsymbol{g}$ is the vector with gravitational terms. $\boldsymbol{I}_n$ are those average inertias reported to the motor axis and are independent from configuration terms. Thus it is possible to model every drive of the robot as shown in Figure 5.3.

Once the model has been calculated, a controller can be designed to move every joint of the robot. A cascade controller with position and velocity loops was chosen. This architecture suits with the knowledge of the constants of every motor of the robotic arm. A large proportional value gives a high rejection to disturbances and increases the stiffness of the system. An integral part cancel the effects of the stationary error. A proportional-integral action is suggested to control this single-input/single-output system [134].

In a cascade control several loops are closed with different variables. These loops are embedded creating inner and outer loops. As the name indicates, a position-velocity cascade control, takes the position values and closes the loop comparing the actual values with reference values. This closed-loop builds an outer loop. The actual velocity values are compared with the output of the outer loop. Changing the constant of these two loops

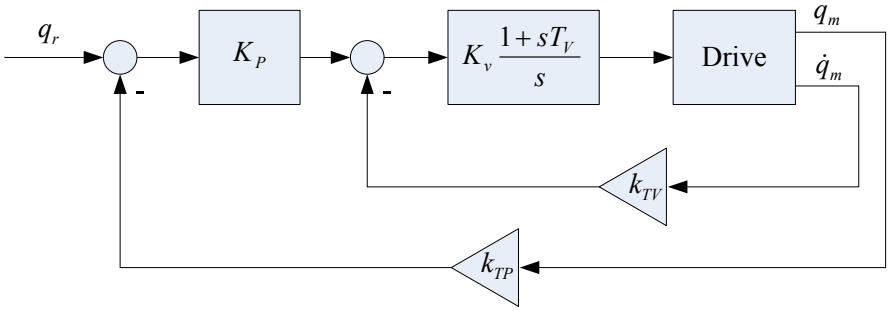

Figure 5.4: Cascade controller. q_m and $\dot{q}_m$ are the position and velocity of the motor respectively. k_{TV} and k_{TP} are transducer constants. K_P and K_V are the controller constant for position and velocity respectively. $T_V = T_m$ where $T_m = \frac{RI}{k_\tau k_v}$.

affects the position of the zeros and poles of the system. This has direct influence in the behavior of the performance and response of every joint of the robot. A position-velocity cascade feedback control is shown in Figure 5.4.

Two profiles were programmed in order to test such control architecture. The first one builds a slow reference value for every joint. The second one builds a fast reference value. As it is shown in Figure 5.5 the manipulator can follow the desired value with a smaller error than when it has to follow a fast reference value (Figure 5.6). This last Figure shows

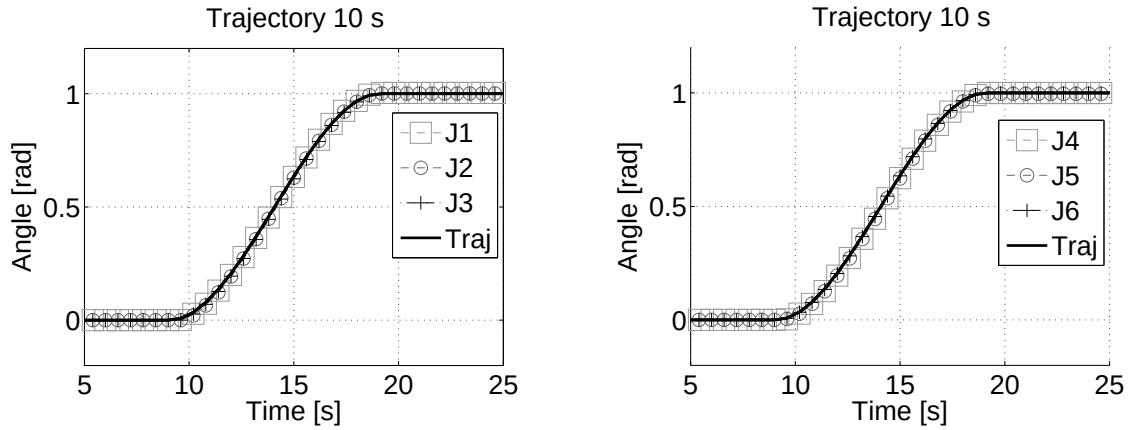

Figure 5.5: Joint space control experiment. The thick line corresponds to the desired value. The trajectory takes 10 seconds to reach 1 rad. a) Response of joints 1 to 3. b) Response of joints 4 to 6.

also an overshoot in the response of the joint number 1 and a delay in all joints. This delay is smaller in joints 4 to 6. This is because these robot axes are the small ones and therefore the mass that they have to move is lower. All these differences are basically due to the dynamic configuration dependent variables (e.g. gravity, friction, centrifugal and Coriolis forces) that are consider like disturbances.

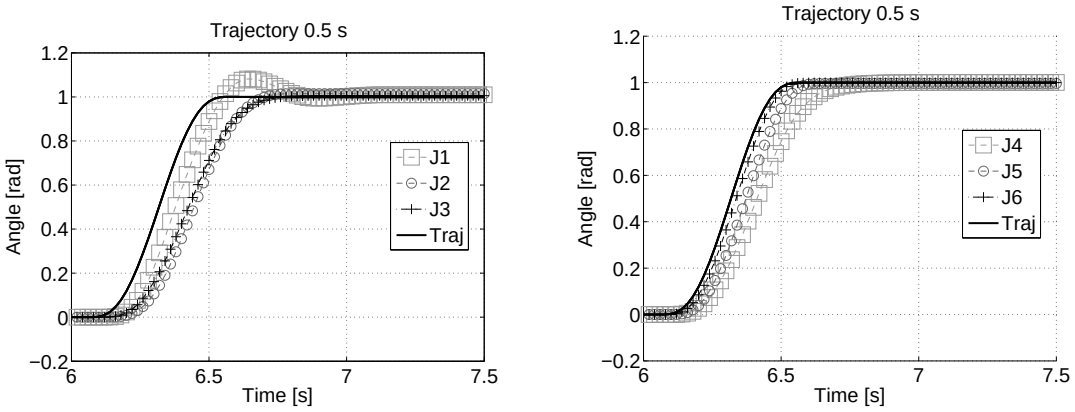

Figure 5.6: Joint space control experiment. The thick line corresponds to the desired value. The trajectory takes 0.5 seconds to reach 1 rad. a) Response of joints 1 to 3. b) Response of joints 4 to 6.

5.4 Cartesian Space Control

In section 5.1, a set of kinematic algorithms for the RX 90-B was developed, which relates joint positions and velocities to Cartesian coordinates and rates of the end-effector. Now it is desired to design a Cartesian Space Position Controller. In such controller, the use of kinematic transformations is essential, since the reference position is given relative to the end-effector coordinates, and the control signal transmitted to the robot must be applied in general coordinates.

The main objective of the controllers presented here is to corroborate the correct performance of the kinematic equations. The controllers described here are of two types:

- PD controller
- ID controller

5.4.1 PD Controller

The PD approach controls the behavior of the robot over the position and velocity errors given in Cartesian space (equations 5.1 and 5.2). These are then transformed to its corresponding $\dot{\boldsymbol{q}}$ in the joint space by means of the $\boldsymbol{J}^{-1}$ and then applied to the robot. Figure 5.7 shows the general structure of this controller where a proportional and derivative part is present. The coupling effect due to the motion of the other links is here ignored, since it is assumed that the coupling effects are disturbances in the control loop of the servo driver.

The representation of $\boldsymbol{X}_e$ in Figure 5.7 is composed of two quantities: 3 parameters of position (x, y and z) and for the orientation the quaternion was chosen [41, 107, 137, 168]. Instead of rotating an object through a series of successive rotations like Euler angles do, a quaternion rotates the object through a single arbitrary rotation axis. Thus a singularity in the representation is avoided (see Appendix C). The representation of the quaternion

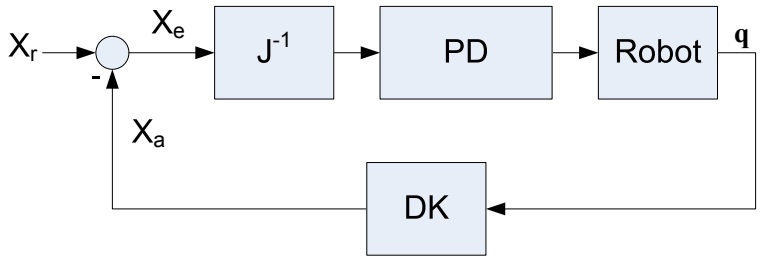

Figure 5.7: Cartesian position controller. PD structure. $\boldsymbol{X}_r$ is the position reference value, $\boldsymbol{X}_a$ is the position actual value, $\boldsymbol{X}_e$ is the error after comparing the values $\boldsymbol{X}_r$ and $\boldsymbol{X}_a$. DK stands for the direct kinematics.

consists of a combination of three parameters (also called vector part: ϵ_x, ϵ_y and ϵ_z) and a real number (also called scalar part: η):

$$\boldsymbol{\phi} = [\eta\ \boldsymbol{\epsilon}^T]^T = [\eta\ \epsilon_x\ \epsilon_y\ \epsilon_z]^T \tag{5.13}$$

Thus the reference and the actual value of position coordinates is described by the (7×1) vector in equation 5.14:

$$\boldsymbol{X}_\phi = \left[\boldsymbol{p}^T\ \boldsymbol{\phi}^T\right]^T = [x\ y\ z\ \eta\ \epsilon_x\ \epsilon_y\ \epsilon_z]^T \tag{5.14}$$

In order to test the PD control three different trajectories in Cartesian space were given as a reference value.

The first trajectory is a line in 3D space which was programmed to be completed in 5 seconds. Figure 5.8 shows tests related to a line in 3D space. Here is difficult to recognize the reference value from the actual value. The robot can follow with high accuracy this profile in 3 dimensions.

The second profile is a rectangle in three dimensions. In Figure 5.9 is shown the reference values and the trajectory followed by the robot. Every side was programmed to be completed in 5 seconds. In Figure 5.10 it can be seen that the error on the XY plane is difficult to visualize in comparison with the error on the XZ plane. That is because of the scale.

The last profile is an eight form shown in Figure 5.11. The reference value was programmed to be completed in 32 seconds. In Figure 5.12 it can be seen that the error on XY plane is not possible to visualize because of the scale.

Figure 5.13 shows the error in position and in orientation along and about the three main axes. All maximum mean errors were found along X axis for every profile. It can be seen that the maximum mean error in position when a line was followed is along X axis and has a value of 0.42 mm. The errors in the orientation have their maximum value about Z axis. The maximum mean error in orientation is about Z axis when the robot follows a line profile and has a value of 0.052°.

These experiments show that the errors are below 0.5 mm in position and 0.06° in orientation which makes the system suitable for biomechanical experiments.

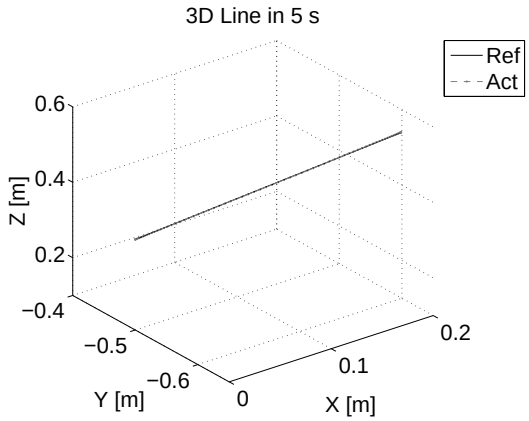

Figure 5.8: Line in Cartesian space under PDC.

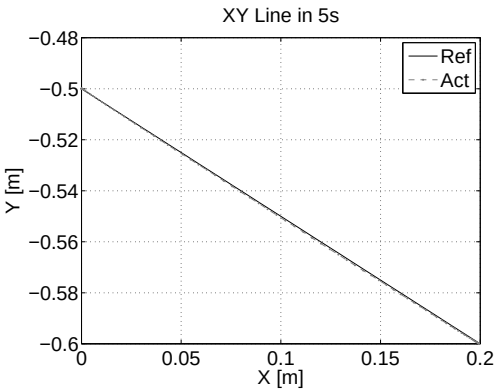

(a) XY representation.

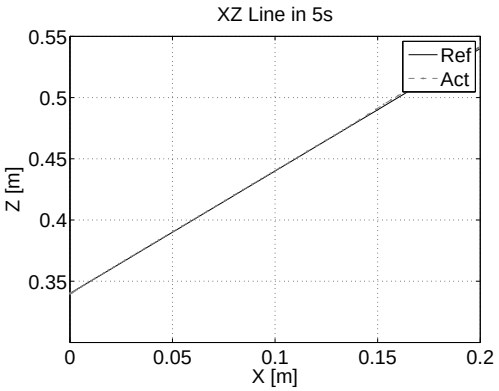

(b) XZ representation.

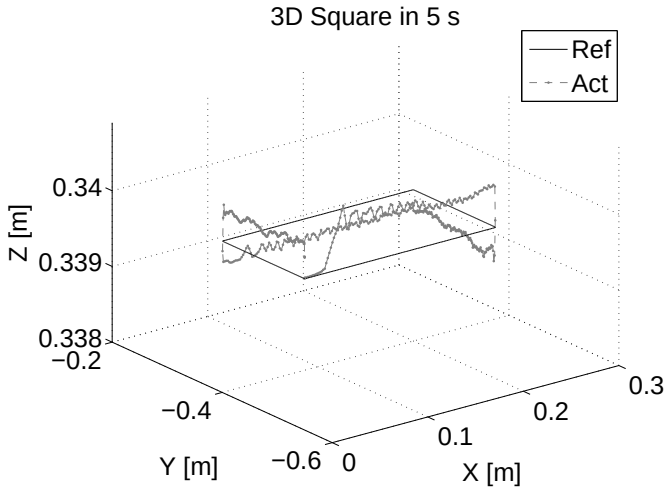

Figure 5.9: Square in Cartesian space under PDC. Three dimensional representation.

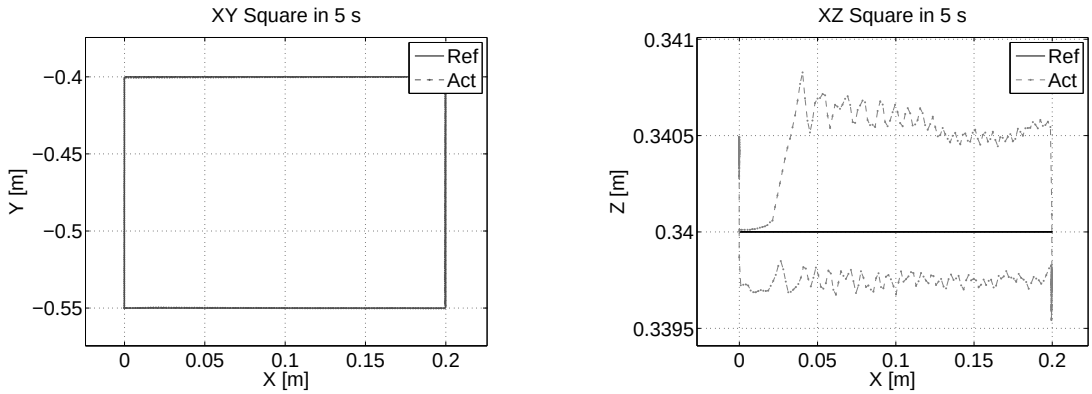

(a) XY representation. (b) XZ representation

Figure 5.10: Square in Cartesian space.

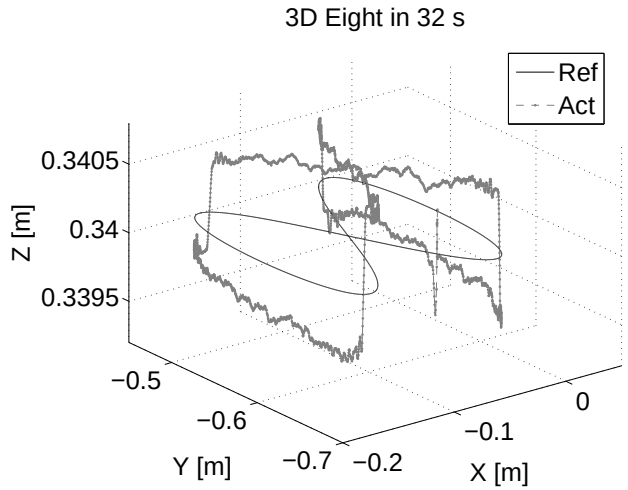

Figure 5.11: Eight in Cartesian space under PDC. Three dimensional representation.

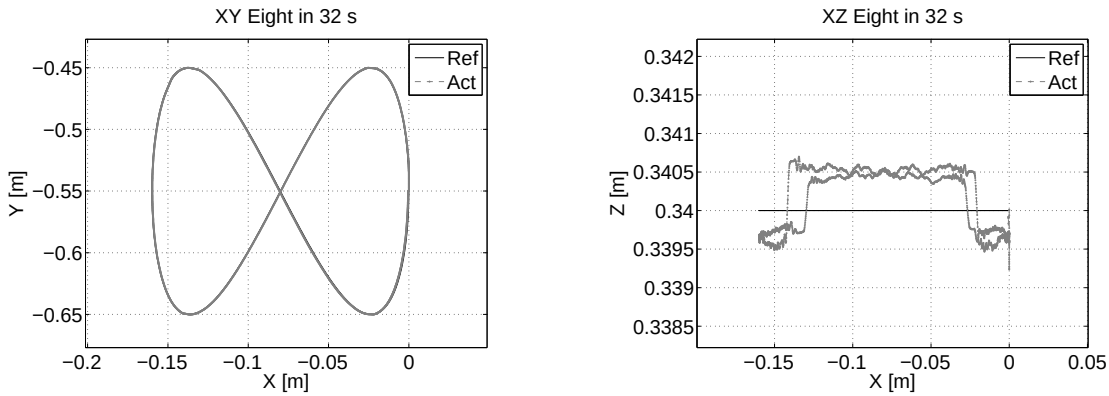

(a) XY representation. (b) XZ representation

Figure 5.12: Eight in Cartesian space.

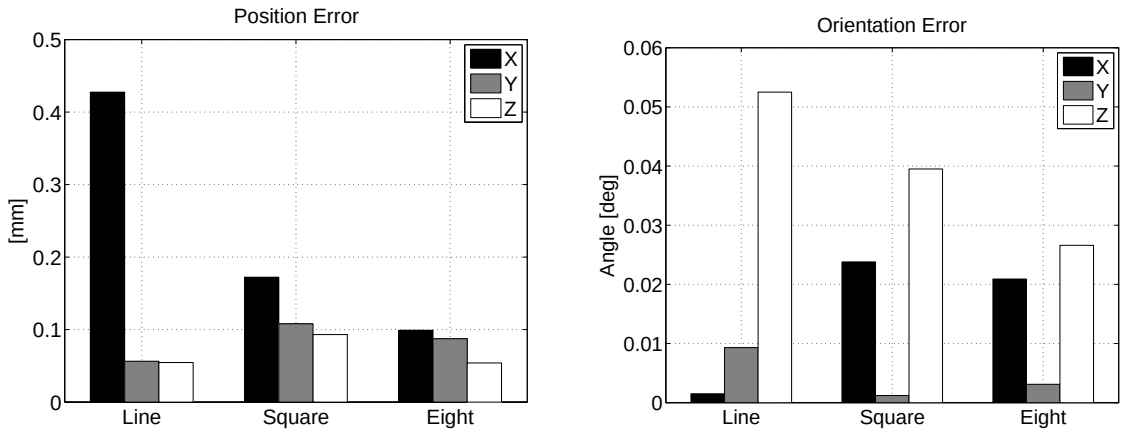

Figure 5.13: a) Position error under PDC. b) Orientation error under PDC.

5.4.2 ID Controller

On the basis of a dynamic model of the robot it is possible to develop central control strategies, in which the robot is considered as a multivariable system with multiple inputs and outputs. Couplings, nonlinearities and configuration-dependent effects on the drives are not included as disturbances but are part of the controlled system and can be included in the control law. As a consequence, in comparison to a decentralized control, a more accurate tracking behavior for a given trajectory can be achieved. A better control approach can be design using equation 5.9 called inverse dynamic control (IDC).

For these reasons several controllers based on a dynamic model should be designed for the RX 90-B. The quality of the controller depends directly on the accuracy of the model. The computation of a model is, however, highly complicated and requires a precise knowledge of the system.

According to equation 5.9 it is possible to design the operational space inverse dynamic control shown in Figure 5.14. $\boldsymbol{K}_D$ and $\boldsymbol{K}_P$ are the constants of the PD controller and $\boldsymbol{n}(\boldsymbol{q},\dot{\boldsymbol{q}}) = \boldsymbol{C}(\boldsymbol{q},\dot{\boldsymbol{q}})\dot{\boldsymbol{q}} + \boldsymbol{F}_v\dot{\boldsymbol{q}} + \boldsymbol{F}_s sgn(\dot{\boldsymbol{q}}) + \boldsymbol{g}(\boldsymbol{q})$.

Several simulations were carried on in order to test this effective control strategy. The same trajectories in Cartesian space of section 5.4.1 were tested. The first profile is a line in 3D. Figure 5.15 and 5.16 show the reference values and the trajectory followed by the simulated robot.

The second profile is a rectangle in three dimensions. In Figure 5.17 the reference values and the trajectory followed by the robot are shown. Every side was programmed to be completed within 5 seconds. It can be seen that the difference in the trajectories on the XY plane is difficult to visualize in comparison with the XZ plane.

The last profile is an "8" form. The reference value was programmed to be completed in 32 seconds. In Figure 5.12 the reference and actual value of the robot is shown. Here can be seen, as in the last figures, that the difference in the trajectories on XY plane is not possible to visualize because of the scale.

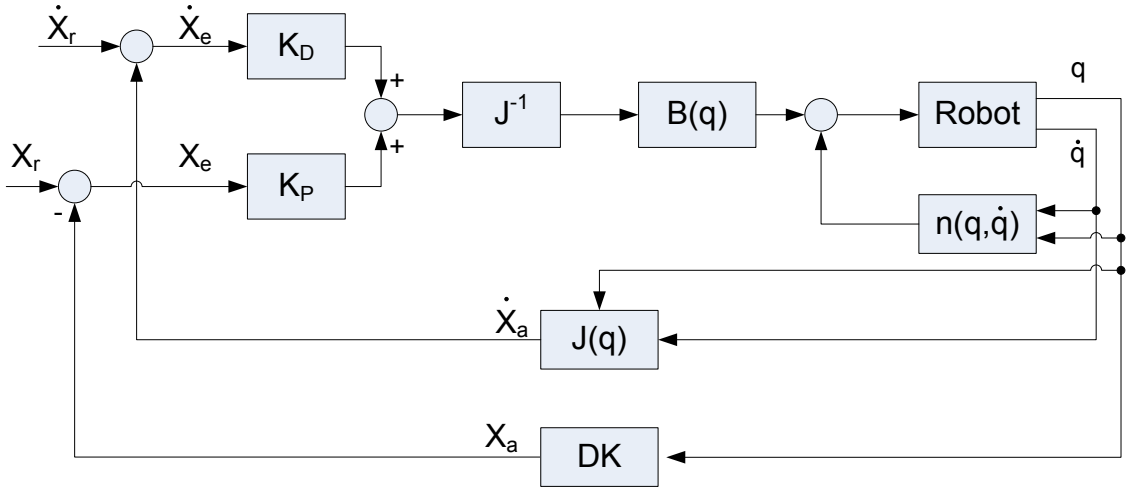

Figure 5.14: Inverse Dynamic Control in Cartesian space.

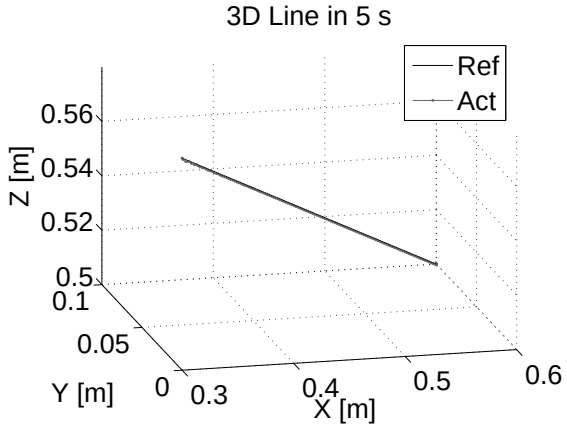

Figure 5.15: Line in Cartesian space under IDC. 3D representation.

Figures 5.21 and 5.22 show the error in position and in orientation along and about the three main axes. All maximum mean errors were found along X axis for every profile. It can be seen that the maximum mean error in position is along X axis and has a value of 0.046 mm when a line was followed. The errors in the orientation have their maximum value about Z axis. The maximum mean error in orientation is about Z axis when the robot follows a line profile and has a value of 0.67°. It can be seen that the error in position was minimized in a power of 10 in comparison with the errors using PDC. However, the orientation error increased in the same magnitude.

These experiments show that the error in the position is less than 0.05 mm and less than 0.7° in orientation.

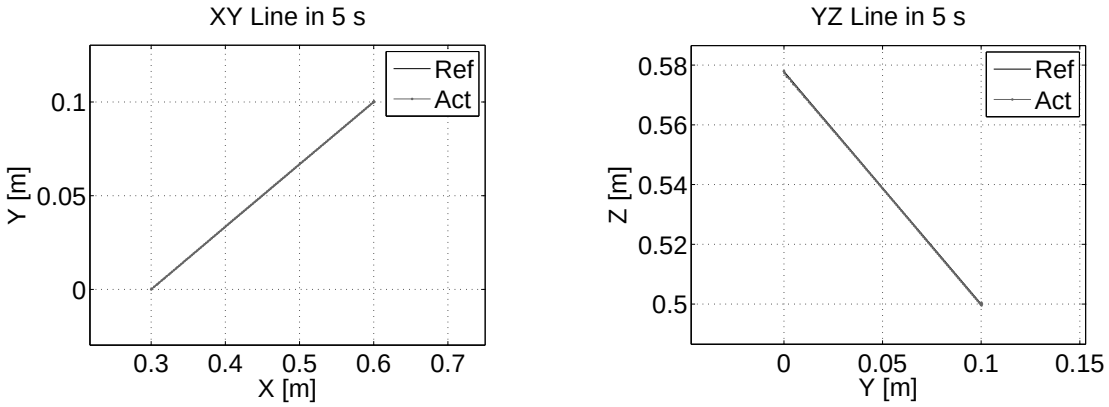

(a) XYrepresentation. (b) YZ representation

Figure 5.16: Line in Cartesian space under IDC.

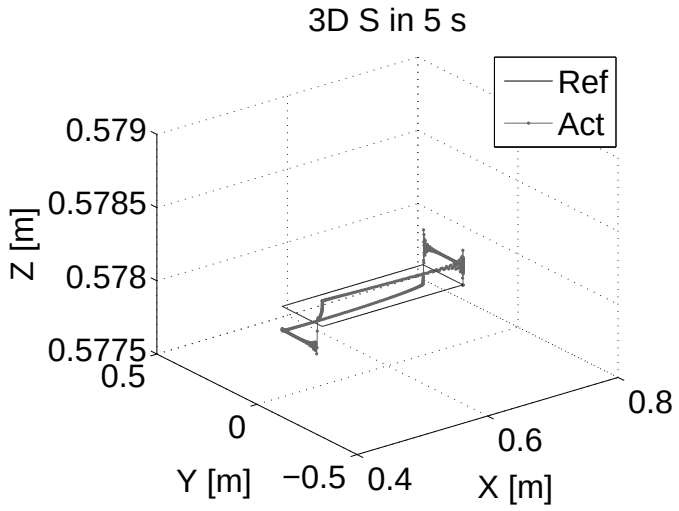

Figure 5.17: Square in Cartesian space under IDC. Three dimensional representation.

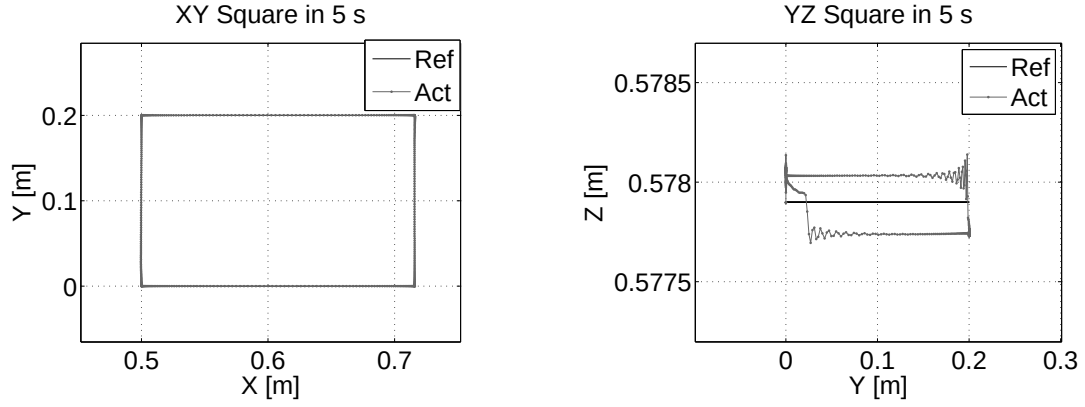

(a) XY representation. (b) YZ representation

Figure 5.18: Square in Cartesian space under IDC.

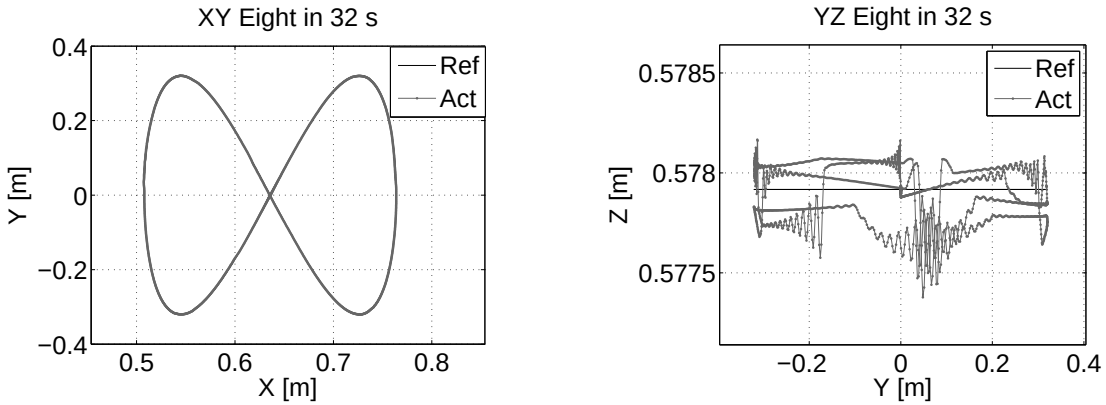

(a) XY representation. (b) YZ representation.

Figure 5.19: Eight in Cartesian space under IDC.

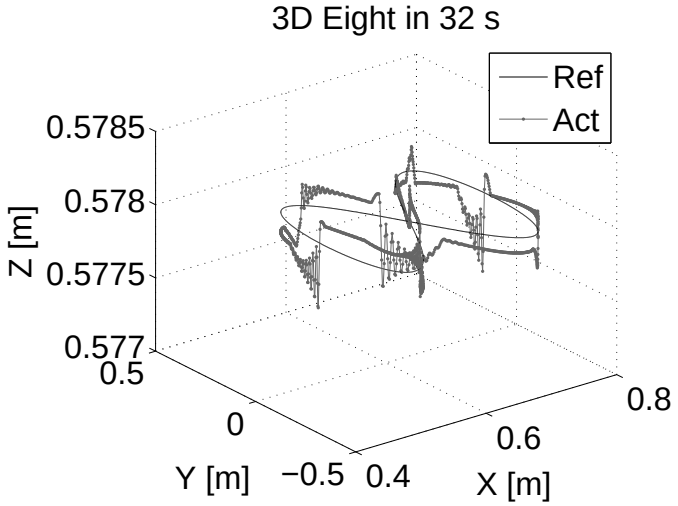

Figure 5.20: Eight in Cartesian space under IDC. 3D representation.

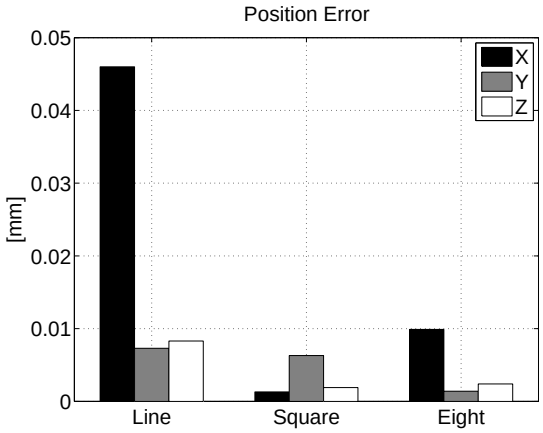

Figure 5.21: Position error under IDC.

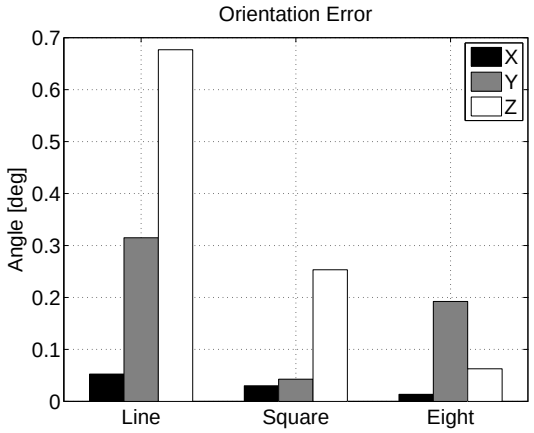

Figure 5.22: Orientation error under IDC.

5.5 Interaction Control

Manipulation requires the robot to be in contact with the environment. It means that both, manipulator and object to be manipulated, are mechanically coupled. The quantity that describes this interaction is the contact force at the end-effector, and thus the manipulator cannot be treated as an isolated system. The very precise position control is not adequate for this purpose. The planning errors may arise contact forces causing deviations of the end-effector. If the position control reacts to reduce such deviation, the contact force will increase causing the saturation of the joint actuators or the breakage of the system in contact. During interaction, the body in contact sets constraints on the path followed by the robot and the situation mentioned before can occur. This drawback can be solved by changing the control strategy [134].

There are many controllers in the literature such as admittance, impedance, stiffness, compliance, hybrid, parallel and force control. All these treat the problem of contact and have special features for specific applications.

Generally it is possible to separate two types of interaction control:

- Indirect control
- Direct control

The first one deals with the mechanics of the interaction rather than controlling directly the movement of the robot. The signals of the forces actuating in the manipulator are not directly compared with a reference or desired value (these forces can be measured by FTS, torque sensors or measuring the current induced in every joint of the manipulator). This means that the force loop in the control structure is an *open-loop* architecture since a direct error is not calculated. The *closed-loop* of such control structure is made in position or velocity. This means that the reference or desired values must be given in terms of position or velocity and will be compared with the actual values given by the sensors of the manipulator and thereby an error will be minimized by the controller.

Compliance and impedance control are examples of such an architecture. The impedance control, for instance, attempts to implement a dynamic relation between the environment and manipulator variables. It controls the impedance as the "port of interaction" with the environment [66]. Figure 5.23 shows that the closed-loop is made with position variables and the force ($\boldsymbol{h}_a$) is just taken into the controller without comparison.

Direct control deals with a direct form of controlling the interaction between manipulator and environment. The actual force will be compared with reference values, thereby a closed-loop is implemented. The robot performs specific movements in order to exert a desired force-moment in the environment. This architecture has the possibility to load specimens with a specific force or moment in/about specific axes.

Examples of this control architecture are: hybrid, parallel, admittance and force control.

In this project is of special interest the possibility of loading biological specimens of animals and/or humans. Therefore it was developed the hybrid and the direct force control architectures.

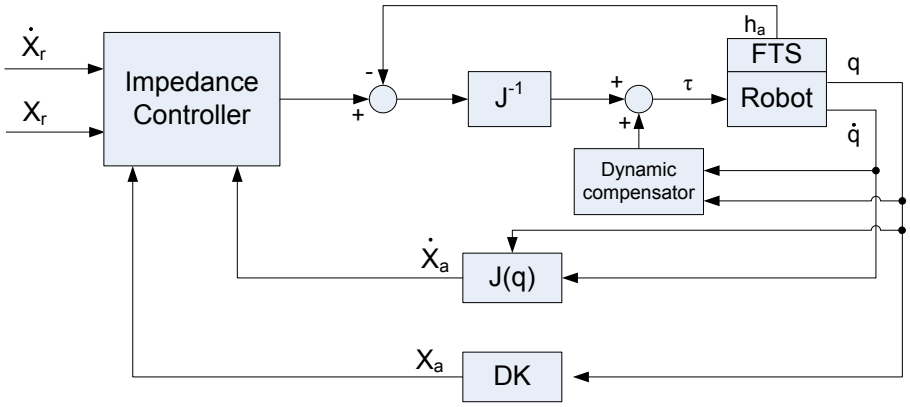

Figure 5.23: Impedance control in Cartesian space.

5.5.1 Direct Force Control

Direct force control is suitable when loading specimens since there is a closed-loop with force-moment signals where a desired profile with units N and Nm can be given.

The goal in biomechanical testing machines is to load specimens with specific profiles. Figure 5.24 shows an example where a spinal should be loaded with a moment about a specific axis while other forces and moments along and about other axis should be zero.

Force Control

A general control architecture of direct force control is shown in Figure 5.25. The reference value $\boldsymbol{F}_r$ is compared with the actual values coming from the FTS $\boldsymbol{h}_a$. The error will be compensated by the controller $\boldsymbol{k}_f$. A damping factor with the Cartesian velocity ($\dot{\boldsymbol{X}}$) that acts in the direction of force control with the velocity gain $\boldsymbol{k}_{vf}$ is designed. $\boldsymbol{J}^T$ converts the units in joint space quantities in order to compute the torques for every joint [83].

The controller $\boldsymbol{k}_f$ is a PI (proportional, integral) controller. Since the signals of forces are normally sensed with noise even after filtering, it is not recommended to use a derivative controller. The derivative action can cause very high values for the torques of the joints which can cause breakage of the motors or of the specimen. It can also lead to instabilities of the robot.

Hybrid Control

The hybrid control [29, 80, 134] combines two interaction control architectures. On the one side there is a closed-loop with force-moment signals, on the other a closed-loop with position-orientation signals. This controller makes possible the control of two important variables in one architecture. However, for any given axis, the manipulator under this control architecture can either control position or force but not both at the same time.

The matrix $\boldsymbol{\Omega}$ act as a switch between both modi. It is a diagonal matrix containing a number 1 if the manipulator is under position control and a 0 if it is under force control. Equation 5.15 is an example where the manipulator is controlled along X, Y axes and about

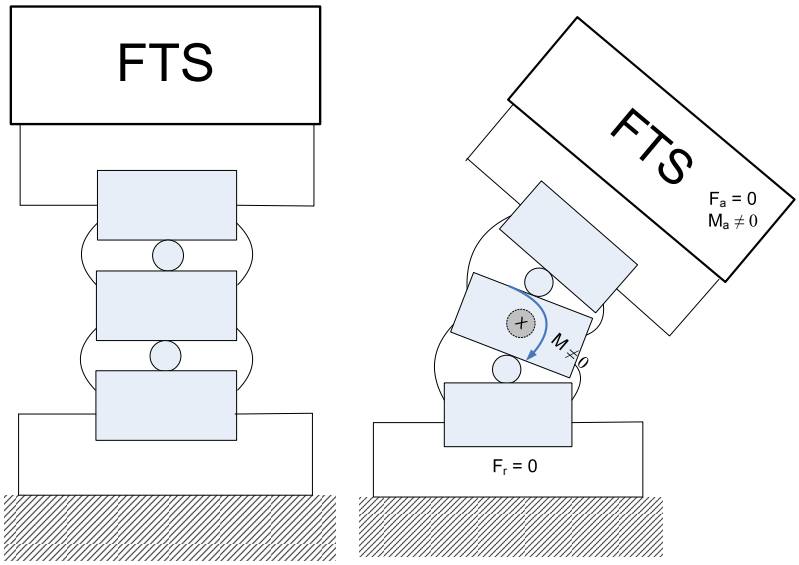

Figure 5.24: a) Schematic representation of three spinal bodies as specimen in initial position (unloaded). b) Specimen loaded with a moment about a single axis while other forces and moments along and about the rest of them are set to zero.

X, Y and Z axes under position control and along Z axis under force control. Thereby the matrix $\tilde{\boldsymbol{\Omega}}$ for force control must be exactly the complement of the $\boldsymbol{\Omega}$ matrix for the position control [29,83,127], that is $\tilde{\boldsymbol{\Omega}} = \boldsymbol{I} - \boldsymbol{\Omega}$, where $\boldsymbol{I}$ is the identity matrix. The hybrid architecture is shown in Figure 5.26.

$$\boldsymbol{\Omega} = \begin{bmatrix} 1 & 0 & 0 & 0 & 0 & 0 \\ 0 & 1 & 0 & 0 & 0 & 0 \\ 0 & 0 & 0 & 0 & 0 & 0 \\ 0 & 0 & 0 & 1 & 0 & 0 \\ 0 & 0 & 0 & 0 & 1 & 0 \\ 0 & 0 & 0 & 0 & 0 & 1 \end{bmatrix} \tag{5.15}$$

Hollerbach [2,3] describes that this controller architecture is unstable in manipulators with revolute joints due to the combination of the $\boldsymbol{\Omega}$ matrix and the Jacobian. Fisher [40] proposed a new architecture where this problem is solved. The matrix $\boldsymbol{\Omega}$ takes the form of $(\boldsymbol{\Omega J})^+$ (where the symbol "+" denotes the pseudo inverse) for position control and $(\tilde{\boldsymbol{\Omega}}\boldsymbol{J})^T$ for force control. The transformations of both quantities always exist and are numerically stable for any manipulator. Although the difference may seem small, it has a tremendous impact on the robustness of hybrid control.

5.6 Automatic Gravity Compensator

When the tool is attached to the FTS (see Figure 4.5), the sensor reports values of force and moment different from zero. Since the weight of the tool and the exact position

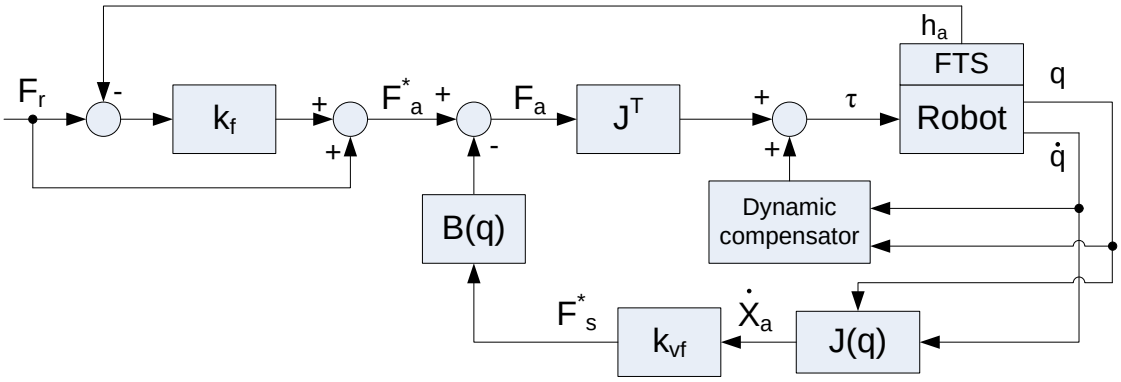

Figure 5.25: Direct Force Control in Cartesian space.

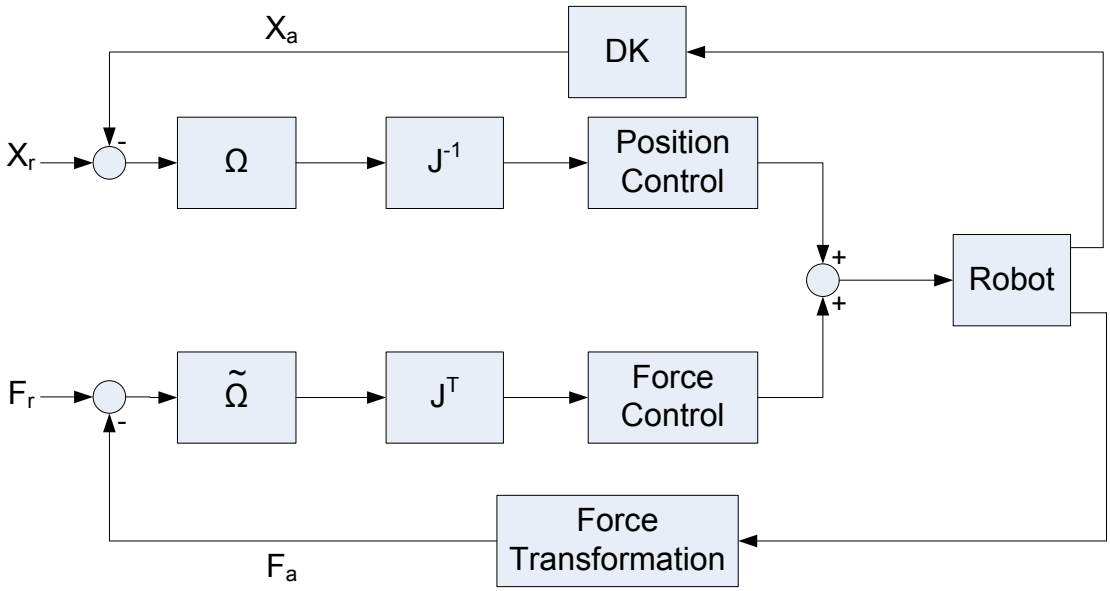

Figure 5.26: Hybrid Control in Cartesian space.

of the center of gravity are rarely known, a method to compensate automatically the gravitational effects of the tool attached to the FTS is needed in biomechanical tests in order to compensate undesired forces and moments signals coming from the gravitational effects of the mounted tool and attachment mechanism of the sensor itself. This deviation introduces errors and can lead to false data, wrong conclusions and the impossibility to compare data produced from other groups with different setups. The weight of the tool and offsets should not have any influence on the measurements.

This sections shows the development of an approach to compensate automatically the weight of the tool attached to the FTS and the description of a mathematical method to change between coordinate systems in order to define the orientation of the direction of the applied forces and moments during biomechanical tests.

5.6.1 Mathematical Method

The manipulator has basically three coordinate systems. The first is called World Coordinate System (WCS) and its position and orientation does not change and serves as a base to reference other coordinate systems. The second coordinate system rests at the top of the last joint (J6) of the robot an it is called J6CS (described by the subscript $_{J6}$). The rotation matrix between both CS is described by the direct kinematics [134] and it is depicted with R_{J6}^{foot}. The FTS has its own coordinate system and it is called sensor coordinate system (SCS). These three important coordinate system are shown in Figure 5.27. Normally J6CS

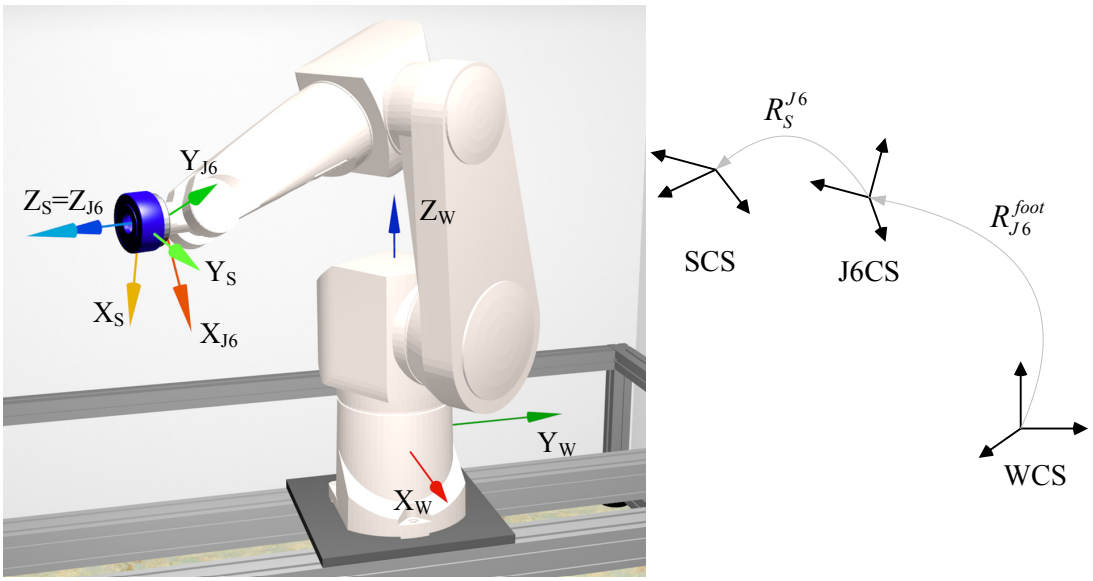

Figure 5.27: 3 coordinate systems: WCS, J6CS and SCS and their pose in the space.

does not match the SCS, therefore an extra transformation should be done in order to align these two coordinate systems. The transformation matrix to align both coordinates system is given by:

$$\boldsymbol{R}_S^{J6} = \begin{bmatrix} \cos\theta & -\sin\theta & 0 \\ \sin\theta & \cos\theta & 0 \\ 0 & 0 & 1 \end{bmatrix} \tag{5.16}$$

When the tool is attached to the sensor it reports a value different from zero (see Figure 5.28). This deviation has 4 components:

1. the forces due to the weight of the tool ($\boldsymbol{F}_{sg}$)
2. the offsets in force when tool is attached to the robot ($\boldsymbol{F}_{off}$)
3. the moments due to the weight of the tool and vector from sensor to the center of mass of the tool ($\boldsymbol{r}_{cm}$)
4. the offsets in moment when tool is attached to the robot ($\boldsymbol{M}_{off}$)

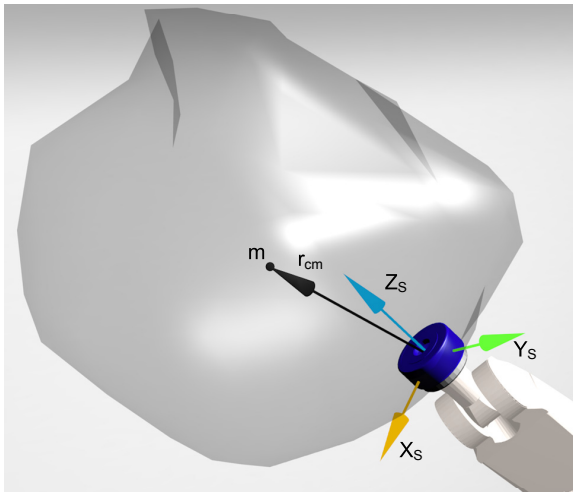

Figure 5.28: Vector $\boldsymbol{r}_{cm}$ that points to the center of mass of an unknown tool mounted on the sensor.

In order to find these 4 parameters the following calculations shuld be done. Gravitational forces are always acting on the direction $-Z_W$ no matter the position of the end-effector. Thus:

$$\boldsymbol{F}_{sg} = \boldsymbol{R}_W^S \boldsymbol{F}_g \tag{5.17}$$

Where $\boldsymbol{F}_{sg}$ is the (3×1) vector of forces (expressed in SCS) reported by the sensor due to the gravity effects on the mounted tool, $\boldsymbol{R}_W^S$ is the (3×3) transformation matrix from SCS to WCS where $\boldsymbol{R}_W^S = (\boldsymbol{R}_S^W)^{-1}$. The matrix $\boldsymbol{R}_S^W$ is known from $\boldsymbol{R}_S^W = \boldsymbol{R}_{J6}^{foot}\boldsymbol{R}_S^{J6}$, where the matrix $\boldsymbol{R}_S^{J6}$ is defined by equation (5.16). $\boldsymbol{F}_g$ is the (3×1) vector of forces (expressed in WCS) due to the gravity. It has only one component in the Z_W axis: $\boldsymbol{F}_g = [0\ 0\ F_{g_z}]^T$, where $F_{g_z} = mg$. Equation (5.17) can be rewritten as:

$$\boldsymbol{F}_{sg} = [\boldsymbol{a}\ \boldsymbol{b}\ \boldsymbol{c}] \begin{bmatrix} 0 \\ 0 \\ F_{g_z} \end{bmatrix} = \boldsymbol{c} F_{g_z} \tag{5.18}$$

where $\boldsymbol{a}$, $\boldsymbol{b}$ and $\boldsymbol{c}$ are the column components of $\boldsymbol{R}_W^S$. The calculation of the moments exerted by F_{g_z} can be done through equation (5.19):

$$\boldsymbol{M}_{sg} = \boldsymbol{r}_{cm} \times \boldsymbol{F}_{sg} = -\boldsymbol{S}(\boldsymbol{F}_{sg})\boldsymbol{r}_{cm} \tag{5.19}$$

where $\times$ is the cross product, $\boldsymbol{r}_{cm}$ is the vector (expressed in SCS) from the SCS to the center of mass of an unkown tool mounted on the FTS and the matrix operator $\boldsymbol{S}(\cdot)$ is described by:

$$\boldsymbol{S}(\boldsymbol{F}_{sg}) = \begin{bmatrix} 0 & -F_{sg_z} & F_{sg_y} \\ F_{sg_z} & 0 & -F_{sg_x} \\ -F_{sg_y} & F_{sg_x} & 0 \end{bmatrix} \tag{5.20}$$

To compensate the deviation of the 4 parameters already mentioned, the following equations

can be set:

$$\boldsymbol{F}_S = \boldsymbol{F}_{meas} - \boldsymbol{F}_{sg} - \boldsymbol{F}_{off} \tag{5.21}$$
$$\boldsymbol{M}_S = \boldsymbol{M}_{meas} - \boldsymbol{M}_{sg} - \boldsymbol{M}_{off} \tag{5.22}$$

where $\boldsymbol{F}_{meas}$, $\boldsymbol{M}_{meas}$, $\boldsymbol{F}_{off}$ and $\boldsymbol{M}_{off}$ are the measured and offset forces and moments respectively (where all are expressed in SCS). When the sensor is under the tool load $\boldsymbol{F}_S$ and $\boldsymbol{M}_S$ should be equal to zero. From equation (5.21) and (5.22) follows:

$$\boldsymbol{F}_{meas} = \boldsymbol{F}_{sg} + \boldsymbol{F}_{off} \tag{5.23}$$
$$\boldsymbol{M}_{meas} = \boldsymbol{M}_{sg} + \boldsymbol{M}_{off} \tag{5.24}$$

Two different poses (denoted by subindex 1 and 2) of the loaded sensor are needed in order to calculate $\boldsymbol{F}_{sg}$ and $\boldsymbol{F}_{off}$. Thus equation (5.23) and (5.24) take the form:

$$\begin{bmatrix} \boldsymbol{F}_{meas_1} \\ \boldsymbol{F}_{meas_2} \end{bmatrix} = \begin{bmatrix} \boldsymbol{c}_1 F_{g_z} + \boldsymbol{F}_{off} \\ \boldsymbol{c}_2 F_{g_z} + \boldsymbol{F}_{off} \end{bmatrix} = \begin{bmatrix} \boldsymbol{c}_1 & \boldsymbol{I} \\ \boldsymbol{c}_2 & \boldsymbol{I} \end{bmatrix} \begin{bmatrix} F_{g_z} \\ \boldsymbol{F}_{off} \end{bmatrix} \tag{5.25}$$

where $\boldsymbol{I}$ is the identity (3×3) matrix. This system is overdeterminated and can be solved calculating the pseudoinverse:

$$\begin{bmatrix} F_{g_z} \\ \boldsymbol{F}_{off} \end{bmatrix} = \left(\begin{bmatrix} \boldsymbol{c}_1 & \boldsymbol{I} \\ \boldsymbol{c}_2 & \boldsymbol{I} \end{bmatrix}^T \begin{bmatrix} \boldsymbol{c}_1 & \boldsymbol{I} \\ \boldsymbol{c}_2 & \boldsymbol{I} \end{bmatrix} \right)^{-1} \begin{bmatrix} \boldsymbol{c}_1 & \boldsymbol{I} \\ \boldsymbol{c}_2 & \boldsymbol{I} \end{bmatrix}^T \begin{bmatrix} \boldsymbol{F}_{meas_1} \\ \boldsymbol{F}_{meas_2} \end{bmatrix} \tag{5.26}$$

In order to calculate the vector $\boldsymbol{r}_{cm}$ and $\boldsymbol{M}_{off}$ three different poses are needed. In view of equation (5.19) and (5.24), it is

$$\begin{bmatrix} \boldsymbol{M}_{meas_1} \\ \boldsymbol{M}_{meas_2} \\ \boldsymbol{M}_{meas_3} \end{bmatrix} = \begin{bmatrix} \boldsymbol{M}_{comp_1} + \boldsymbol{M}_{off} \\ \boldsymbol{M}_{comp_2} + \boldsymbol{M}_{off} \\ \boldsymbol{M}_{comp_3} + \boldsymbol{M}_{off} \end{bmatrix} = \begin{bmatrix} -\boldsymbol{S}(\boldsymbol{F}_{sg})_1 & \boldsymbol{I} \\ -\boldsymbol{S}(\boldsymbol{F}_{sg})_2 & \boldsymbol{I} \\ -\boldsymbol{S}(\boldsymbol{F}_{sg})_3 & \boldsymbol{I} \end{bmatrix} \begin{bmatrix} \boldsymbol{r}_{cm} \\ \boldsymbol{M}_{off} \end{bmatrix} \tag{5.27}$$

Using the pseudoinverse, the system can be solved by:

$$\begin{bmatrix} \boldsymbol{r}_{cm} \\ \boldsymbol{M}_{off} \end{bmatrix} =$$
$$\left(\begin{bmatrix} -\boldsymbol{S}(\boldsymbol{F}_{sg})_1 & \boldsymbol{I} \\ -\boldsymbol{S}(\boldsymbol{F}_{sg})_2 & \boldsymbol{I} \\ -\boldsymbol{S}(\boldsymbol{F}_{sg})_3 & \boldsymbol{I} \end{bmatrix}^T \begin{bmatrix} -\boldsymbol{S}(\boldsymbol{F}_{sg})_1 & \boldsymbol{I} \\ -\boldsymbol{S}(\boldsymbol{F}_{sg})_2 & \boldsymbol{I} \\ -\boldsymbol{S}(\boldsymbol{F}_{sg})_3 & \boldsymbol{I} \end{bmatrix} \right)^{-1} \begin{bmatrix} -\boldsymbol{S}(\boldsymbol{F}_{sg})_1 & \boldsymbol{I} \\ -\boldsymbol{S}(\boldsymbol{F}_{sg})_2 & \boldsymbol{I} \\ -\boldsymbol{S}(\boldsymbol{F}_{sg})_3 & \boldsymbol{I} \end{bmatrix}^T \begin{bmatrix} \boldsymbol{M}_{meas_1} \\ \boldsymbol{M}_{meas_2} \\ \boldsymbol{M}_{meas_3} \end{bmatrix} \tag{5.28}$$

With equations (5.26) and (5.28) the 4 wanted parameters are calculated. There are at least 2 ways to express the forces and moments calculated with this method:

1. Forces and moments expressed in WCS. No matter the pose (position and orientation) of the sensor mounted on the last joint of the robot, the forces and moments will be expressed in the base coordinate system.

2. Forces and moments expressed in SCS. The forces and moments are expressed in the changing coordinate system of the sensor. Equations (5.21) and (5.22) show their mathematical descpription after the compensation.

In order to calculate the forces expressed in WCS the following changes shall be done:

$$\boldsymbol{F}_W = \boldsymbol{R}_S^W \left(\boldsymbol{F}_{meas} - \boldsymbol{F}_{off}\right) - \left[0\ 0\ F_{g_z}\right]^T \tag{5.29}$$

The gravitational vector is always pointed to the $-Z_W$ axis. Therefore the forces reported by the sensor have to be converted into forces expressed in WCS and then subtract the gravitational term. The changes to calculate the moments expressed in WCS are shown in the following equations:

$$\boldsymbol{r}_{cm_W} = \boldsymbol{R}_S^W \boldsymbol{r}_{cm} \tag{5.30}$$

$$\boldsymbol{M}_{comp} = \boldsymbol{r}_{cm_W} \times \left[0\ 0\ F_{g_z}\right]^T \tag{5.31}$$

$$\boldsymbol{M}_W = \boldsymbol{R}_S^W \left(\boldsymbol{M}_{meas} - \boldsymbol{M}_{off}\right) - \boldsymbol{M}_{comp} \tag{5.32}$$

M_{comp} is the moment expressed in WCS exerted by the tool mounted on the sensor. $\boldsymbol{r}_{cm}$ is expressed in SCS but F_{g_z} is expressed in WCS. Again here the measured values and offsets are expressed in SCS. Therefore they have to be converted in WCS and then subtracted from M_{comp} which is already expressed in the same coordinate system.

6 Biomechanical Testing Workflow

The manufacturer of the RX 90-B supplied already a control unit which has a central process that sends control signals to the motors of the robot. It can also receive and process signals in order to design a closed-loop controller.

The control unit is connected via Ethernet to a normal PC where programs in V+ can be written in order to define specific tasks for the robot. The control architecture of the Stäubli is not fast, flexible and robust enough for the purpose of our group.

As already mentioned in section 4.4, an open architecture of the robot was implemented in order to qualify it for the accomplishment of biomechanical tests. To enable a higher frequency, the original control architecture of the robot has been modified. Some functions of the control unit have been replaced by a powerful real-time computer. Its operating system, xPC Target, is a highly specialized operating system that makes the reliable execution of programs in order to meet the hard real-time requirements, such as the calculation of the kinematics, dynamics, Coriolis and centrifugal forces with the high frequency demanded. xPC Target belongs to the family of MATLAB & Simulink. Figure 6.1 shows a graphical representation of the interconnected units.

When working with biological specimens, grasping becomes a critical issue. The specimens were embedded in a resin in order to ensure the stability of the body while the robot performs specific movements. Biological specimens are very special "materials". They are very difficult to represent with models (e.g. in finite element theory). They have a very complex geometry, their properties are not linear, all DoF are coupled, they are anisotropic and their properties change with the time. As is mostly the case, biological materials have tendons, ligaments, muscles and bones. These materials contain certain amount of fat, blood and other substances. This makes them very difficult to be attached to a mechanism.

In the following sections are described the procedures to prepare the system in order to perform biomechanical tests. Descriptions of the GUI and the 3D visualization are given. The procedure to embed and attach the specimen to the robotic tool is described.

6.1 System Preparation

Dealing with a robot requires a depth knowledge of robotics and experience. It would be necessary a long training period for a user who wants to perform only a few experiments with the robot. This in practice is very difficult to carry on. Therefore, it is important for the user to have a tool that can use in a simple way and which contains all the functions necessary to run an experiment. A GUI, as abstract interface between man and machine, is for this purpose developed. This allows a simplified operation of the robot avoiding potential user errors that can lead to uncontrolled behavior of the robot.

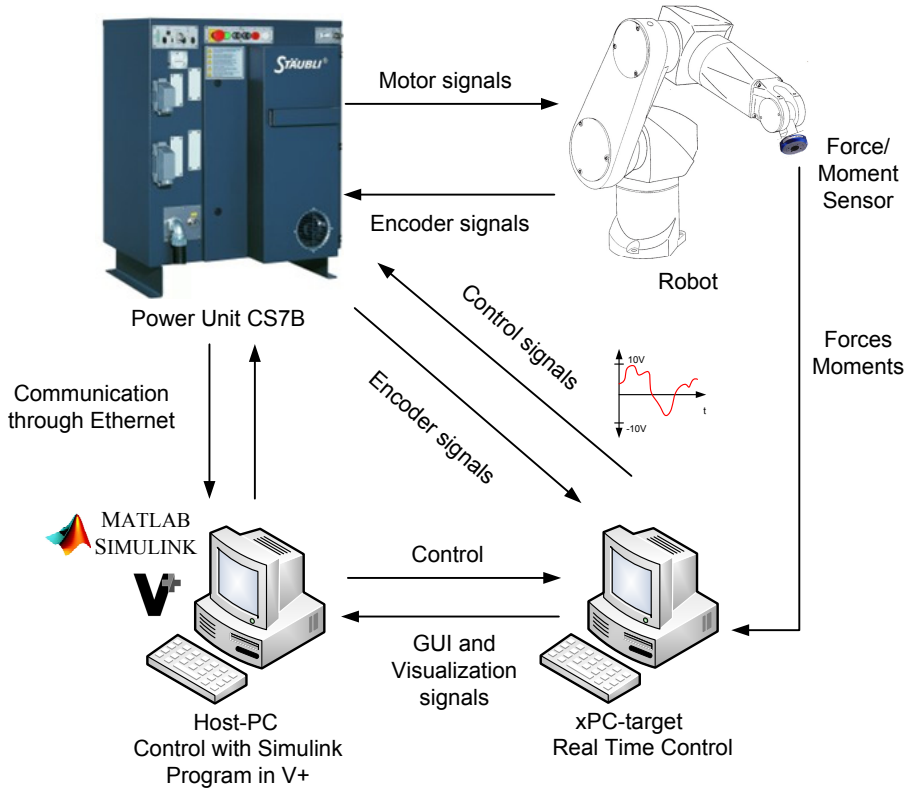

Figure 6.1: System design where four main components are interconnected.

Even if a safety concept has been implemented, a robot remains physically dangerous. Robot, specimen, environment and user can be damaged. During the experiments it is relevant to inspect the movements of the specimen together with the robot from a short distance or different angles. The robot can become unstable and its movements cannot be predicted or controlled anymore. In this case, the danger for the observer increases even more. Therefore a visualization in a 3D space is required. Installing cameras in different angles of the experiment can be very expensive. Thus a virtual world has been developed in order to visualize in 3D the movements of the robot and specimen reducing the danger already mentioned. This 3D representation allows visualization from all angles and distances that would be very difficult or even impossible to reach with normal cameras.

An additional advantage of a 3D virtual world is that the user can plan the procedure of the experiment without moving the robot or working with biological specimens. He can perform simulations and define directions of movement that afterwards will be accomplished by the robot. Thus the danger is minimized, possible errors can be detected in advance and a better protocol can be written.

6.1.1 GUI

The user can operate the robot directly using the user interface. The control of the robot is implemented in real-time. Consequently, the software used to create the user interface enables communication with a real-time application. The GUI offers the possibility to start

or stop the real-time application. It allows also to set user-entered PID parameters in the control of the robot. It reads and displays signals from the sensors (such as forces and moments occurring during the execution of an experiment) in order to provide additional graphical surveillance. It is also important after the completion of individual experiments that the data registered by the robot (e.g. Kinematic variables) and by sensors (e.g. from FTS forces and moments) be saved for an offline analysis. The user interface is designed in such way that the interaction can take place as intuitively as possible and minimize danger to a user or the manipulator itself.

Development

The GUI was developed with a simple design, flexible and also scalable to allow a straightforward extension of existing functionality. The concept Host-Target and the interaction with the GUI is shown in Figure 6.2. The non time-critical tasks run in the host PC, and the time-critical tasks in the real-time computer. Two interfaces must be implemented in order to read and send signals between computers through the GUI.

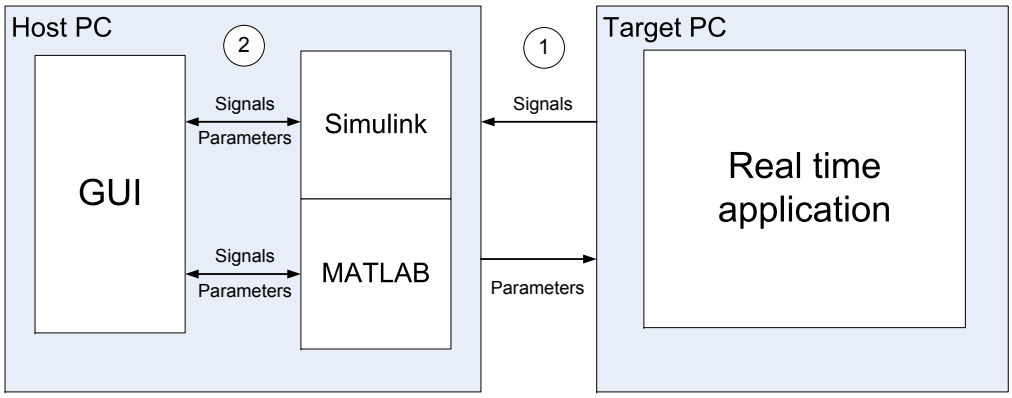

Figure 6.2: Host-Target concept and its interaction with the GUI. Signals in real-time and non real-time are denote with the number 1 and 2 respectively.

The first interface (Figure 6.2 denoted with the "1") takes place due to the separation between the host and target. The signals coming from the sensors installed in the robot (e.g. encoders or FTS) will be received by the target PC. From this computer is possible to read data in order to be graphically represented or saved by the GUI. A high quality graphical representation of variables (e.g. forces, moments) plays in this context an important role. xPC Target is unsuitable as a platform for the use of graphics-based application programs.

The second interface (Figure 6.2 denoted with the "2") occurs in the host and has direct communication between the GUI and MATLAB & Simulink. Thereby several parameters and commands (e.g. start the real-time application or stop the robot in a specific position) can be sent to the target PC in order to control the whole experiment.

The use of a LabVIEW as a program to develop the GUI and using the MATLAB script blocks is the best solution in terms of flexibility, scalability and maintainability. It is possible to take advantage of both software packages to connect the friendly interfaces

and state machine oriented programs of LabVIEW and the computation robustness of MATLAB.

The GUI is divided in 5 states shown in Figure 6.3. In every state take place specific processes where different information (variables) are entered by the user (called user data) or fetched by the GUI itself.

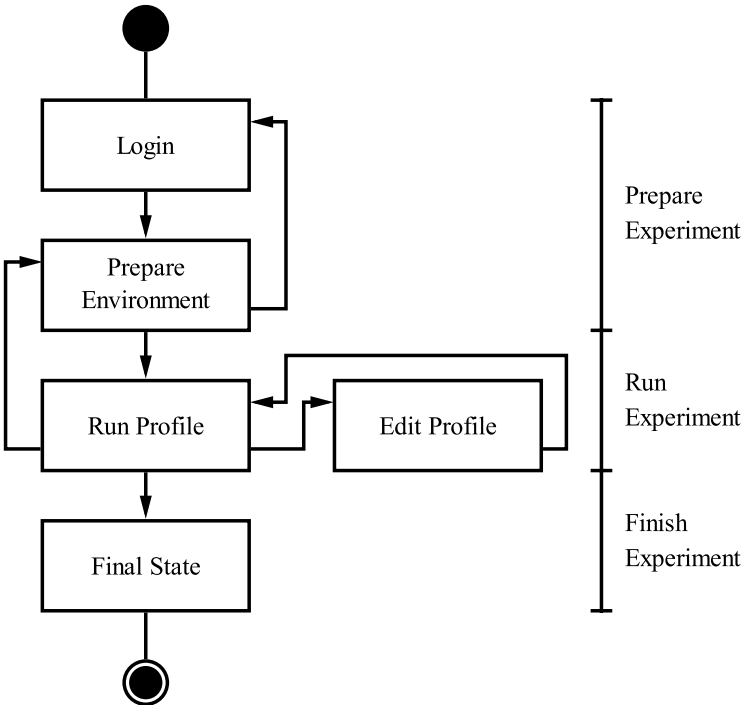

Figure 6.3: Structure of the GUI developed with a State Machine.

The execution of biomechanical tests usually requires to test several specimens. Therefore, it is frequently the case that a user organizes his experiments within several days. Since the robot is to be operated by multiple users, it can happen, that the same person aims to perform similar past experiments. In order to facilitate the process of entering user data (e.g. forces, moments, experiment duration) each time, it should be stored in individual user accounts in order to fetch this information when the GUI is re-started. Therefore, the first step of this interface is to load from individual user names their corresponding data from an existing account or, as a new user, create a new one.

Before the actual experiment can be started, some preliminary steps are necessary. This requires that the right tool be assembled at the end-effector of the robot, or to move it to a predefined position to connect it to the test object. In addition, the sensor to measure the forces and moments that occur during the experiment should be calibrated so that the results are not distorted by interfering influences (see section 5.6). Depending on the type of specimen to be tested different steps may be necessary. Some are obvious and may therefore not be forgotten. Task of the GUI is to ensure that the preliminary steps are carried out, otherwise the robot cannot be used as desired. The individual steps need to be made in the appropriate order and without compromising the functionality of the whole system.

If these preliminary steps are completed, the user can proceed with the actual tests. If the aim is to create special robot-motion profiles in order to investigate biomechanical properties of individual specimens, the user shall submit certain positions either fixed in space, which will drive the robot, or specify how big forces or moments are, in order to be applied by the manipulator. In the first case a profile in position will be generated; in the second in force.

Both types of profiles, position and force, are available in different parts of the control code. What kind of profile should be used depends on the question that lies behind the particular experiment. The GUI should therefore provide the user with the ability to define them. For this purpose, the user can choose between different types of profiles and set their associated parameters. In this way he can create several different profiles according to their individual requirements. If he has in previous sessions already introduced this information, it will be loaded by the user account.

In the next step, the robot should move according to the chosen reference values. It is the responsibility of the control to ensure that the predetermined paths are accurately followed. In this point the communication interface plays an important role. First, the parameters are passed to the controller of the current profile. Then the robot will move following the chosen profile when the operator gives the Start instruction. During this process designated signals are graphically shown so the user has an additional visual window to check whether the robot follows the guidelines or not. If not, the manipulator should be stopped by a command from the user. If the robot has followed the desired profile there is the possibility, given its current position, to proceed directly to a new profile or to finish the experiment. Alternatively, it should be available to bring the manipulator to the starting position, where it can continue with a new profile, or to change specimen. For an offset analysis of the experiments already run, the user can manually save the measured data in a specified directory on the host PC or let the GUI do it automatically. This data must be transferred from the hard disk of the target PC to the host PC.

Thanks to the Matlab interface, it is possible that all the above steps can be executed directly from the user interface.

Operating the GUI

The operation of the GUI is intuitive and user friendly. In order to maintain the scalability, but also to allow flexibility in the modification of different layouts (different experiment scenarios), the entire visible area of the GUI is contained in a tab structure.

Immediately after starting the GUI the state *Login* is activated. All controls, including the preparation of the experiment, are on the first page of the tab structure (Figure 6.4). Since all these steps are performed by the user and cannot be confirmed by a program, a check list is shown to the user so that all the arrangements for the experiment be done before to start the movements of the robot. The user is not allowed to continue if he does not check all the check boxes.

The user can then choose between two kinds of control: position or force control. This choice depends on the goal of the experiments. If the user wants to use the position control, he is asked to introduce proper parameters like final point in Cartesian space and the time to carry on the movement. Assuming that the user has chosen the force control option,

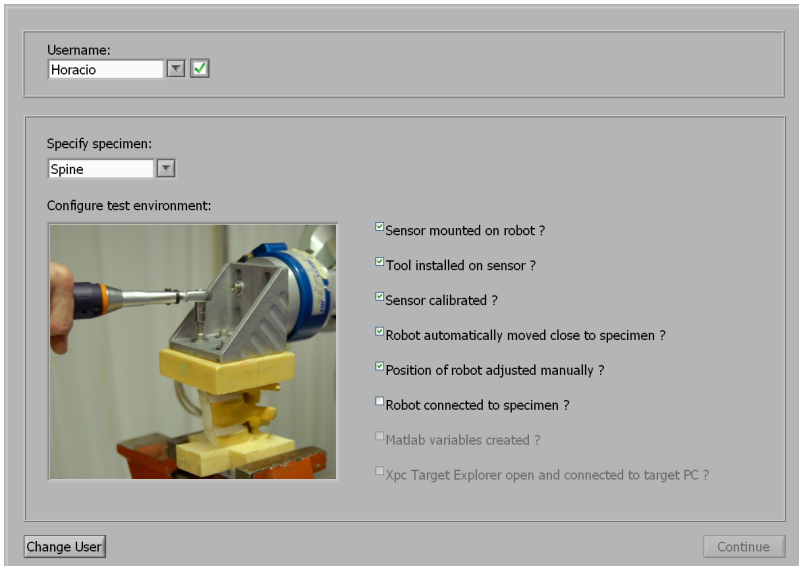

Figure 6.4: Login and check list. First page of the GUI.

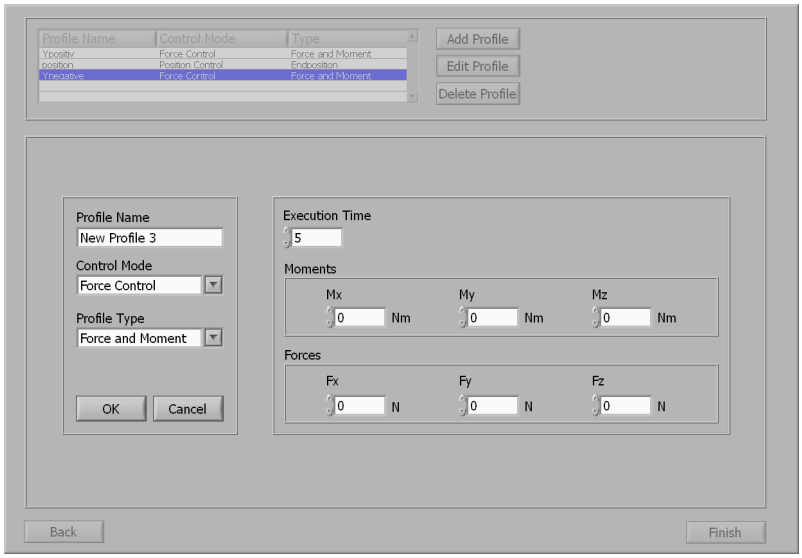

Figure 6.5: Force control. Specific parameters should be here introduced.

proper parameters must be introduced (final forces and moments and the time to complete the movement). Figure 6.5 shows an example when the user has chosen force control.

A list containing different experiments is also shown to the user. Thus several experiments can be configured and be visualized, deleted or edited. Once all configuration for the test and the experiments have been defined with their specific properties, the user can begin with the test. He can choose an experiment from the saved list. By pressing the button *On – Controller* the real-time PC starts and the brakes of the robot can be removed. The button *Home* will produce a movement of the robot under position control to the defined home position (normally this will be the robot position after attaching the specimen). After that, the chosen experiment will be performed and the desired signals will be displayed (e.g. desired forces and moments). Figure 6.6 shows all these options in the GUI.

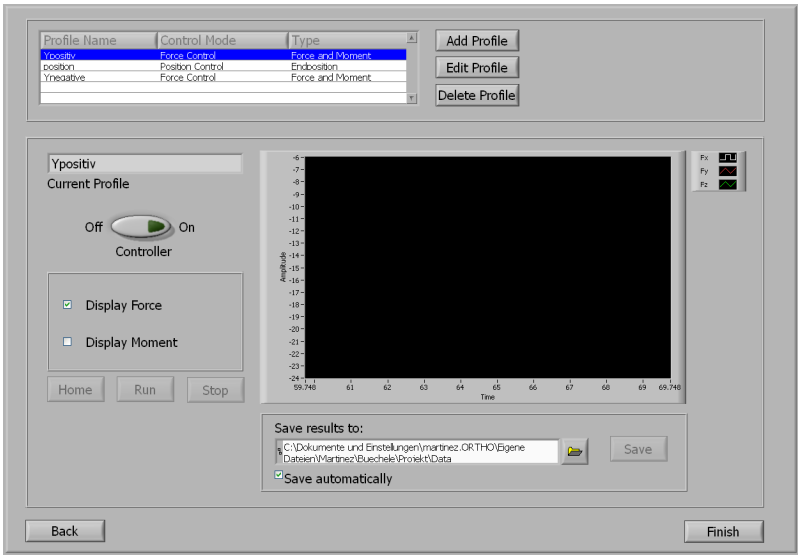

Figure 6.6: Page of the GUI where the experiment can be defined. The controller can be started and specific signals can be graphically represented. Options to save signals collected by the test are shown.

An important implementation was programmed in order to save the experiment data. The user can choose between automatically (in order to reduce possible lost of data) or manually (with the high probability that data will be lost). After accomplishment of all experiments the user can click on the *Finish* button to terminate the application but also to save the introduced user data. This has the objective to save time when the same user loges in again. If this happens, all last data from the experiments will be loaded and will be ready to be performed, changed, expanded or deleted.

6.1.2 3D Visualization

The structure of the system and the possibility to move with the robot a specimen in 6 DoF opens up many possibilities for different experiments. Since the development and coordination of the experiments take place in an interdisciplinary team, it is imperative that both, engineers and physicians, plan appropriate robot motions during the experiments in order to easily understand the procedure and plan in advance specific protocols. A mathematical representation of the trajectory can give only an abstract idea of the possible robot motion sequence. It is in consequence unsuitable for planning and discussion of the experiments. Furthermore, it should be considered in the design of the trajectory to ensure that all obstacles and limitations of the workspace are avoided. Planning mistakes can lead to collision and damage to the robot and the destruction of the specimens. It is, therefore, required a spatial representation of the robot where the experiments can be simulated and visualized not just analytically but graphically in advance.

If the test sequence is set and a trajectory was determined, which could be verified by simulation, it is possible to perform experiments. The motion of the robot is carried out starting from a PC-control station, which is about 3 meters away from the robot. The angle between this spot and the robot is very limited and it is difficult to see the exact end-effector position in the space. To allow a more detailed view of the robot from different

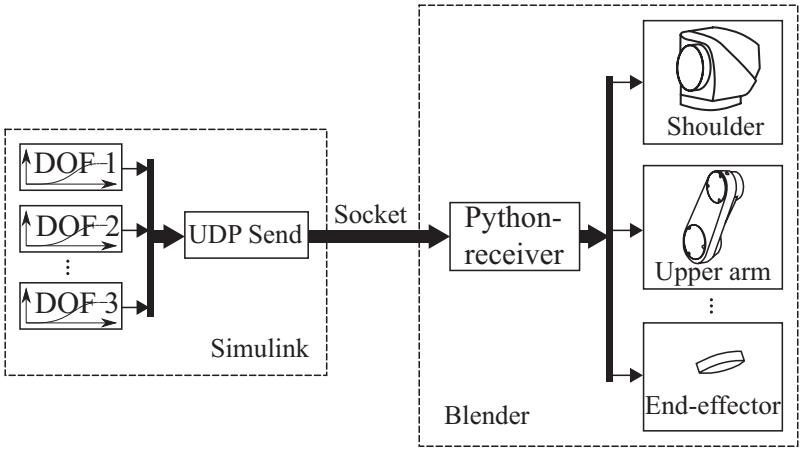

Figure 6.7: Schematic architecture of the serial transmission.

angles, a program is necessary that represents the robot in 3D while it is controlled in real-time.

Development

It is desired to implement the 3D visualization in the open source, cross platform suite of tools for 3D creation called Blender. Blender offers high functionality and is user-friendly. Unlike Simulink 3D Animation, Blender is available for free. The creation of the environment, the addition of new parts (e.g. different specimens or clamps mechanism) and changes in the robot or tools on the end-effector can be easily and with less effort designed, changed and programed in this open source program.

Although Blender is an interactive 3D visualization tool, the communication with other applications has to be considered. However, it is possible to create arbitrary constructs with the object-oriented scripting language Python and be embedded to be sent to another application. There is the possibility to send packages through the network using UDP (User Datagram Protocols). This is suited for the developed system architecture (see section 4.4).

The transmission of Simulink signals can be made in serial mode. In this kind of transmission, all six DoF of the robot are gathered in a large UDP packet and sent in each transmission cycle through a socket. The size of the package results in this case the sum of the UDP header, IP-/Pseudo-Headers and the memory requirements for six MATLAB double variables (Figure 6.7).

The changes of the model in MATLAB & Simulink depend on the installed version and the existing extensions and toolboxes. In version R2010a is the block *UDP send* in the Signal Processing Blockset available. In version R2009a binary UDP packets can be sent with *UDP Send Binary* in the Toolbox xPC Target, *UDP Send and UDP Send Host* in the Instrument Control Toolbox and Target Support Package TC6 (Figure 6.8).

For planning purposes a collision detector was also implemented. The visualization will notify the user with a message when a part of the robot has collided with itself. Boundary

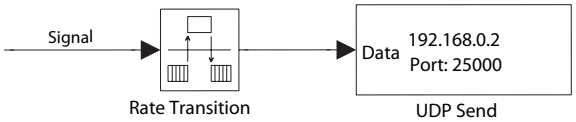

Figure 6.8: Changes in the Simulink model to send UDP packets.

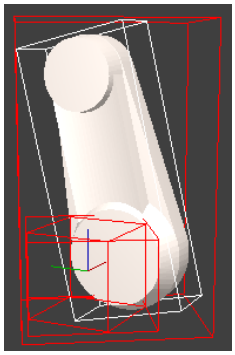

Figure 6.9: Boundary conditions to implement a collision detector.

conditions must be defined for every joint in order to activate specific Blender sensors that detect an impact with other boundaries as shown in Figure 6.9.

This procedure is the same for a simulation and for a real-time environment. With these changes it is possible to visualize in simulation and in real-time the movements of the robot in a 3D environment. A menu with different options for the movement of the camera was developed. Thus the camera in the visualization can be moved to any position in the 3D world. A general view of the visualization is shown in Figure 6.10.

The robot visualization is to be installed on the host computer. It receives the signals, which include the current position of the robot, at intervals from the target computer. It is possible to read the data transmitted directly from the xPC Target computer. The UDP packages are embedded in the Simulink model to be compiled and downloaded in the Target. Thus the transmission rate of UDP packages can be up to 60 Hz which is enough to have a fluent visualization. Ideally, the transfer of frames should be of 60 times per second, because this is the maximum frequency of images that humans can perceive. This implementation does not affect the performance of the controller due to the simple and compact changes that must be done in order to transmit the packages. The image processing and visualization is carried out by the Host computer. Therefore, time critical tasks are not affected.

Operating the 3D visualization

The main menu of the 3D visualization includes useful information for users in five main menu items:

- Start (bottom left): Initiates the robot visualization,
- Quit (bottom right): Ends the visualization and closes the application,
- Experiment settings (center first place): Choice of the experimental setup,

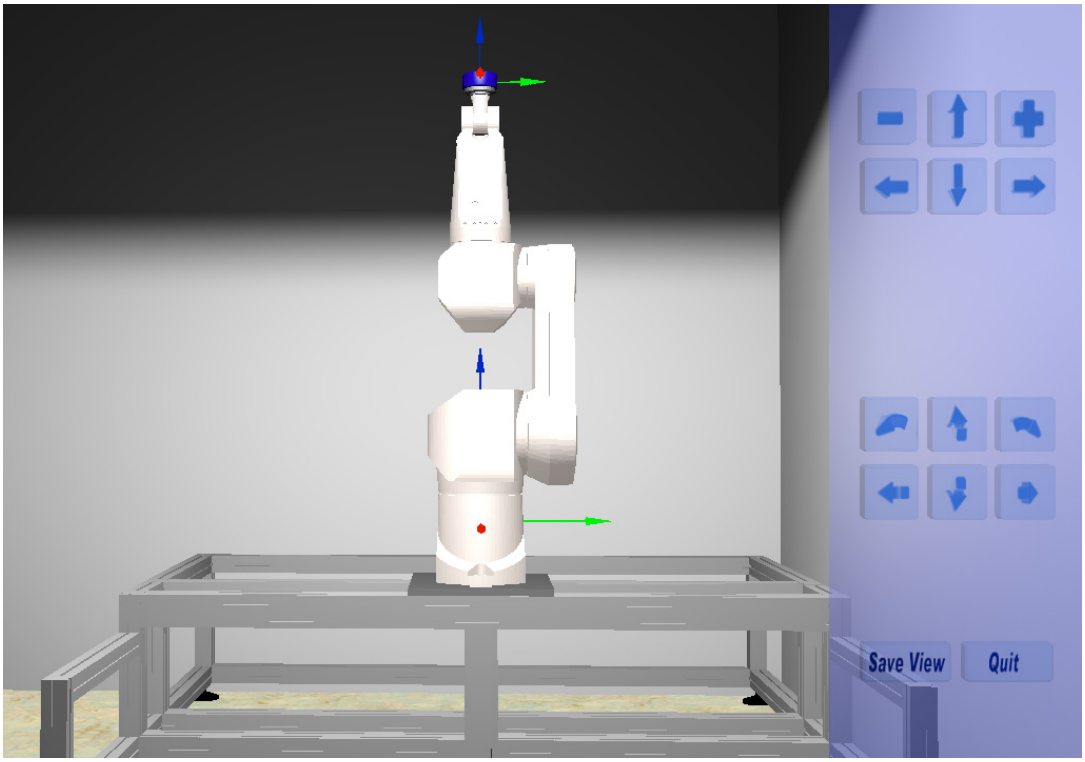

Figure 6.10: General 3D visualization with menu bar for camera movements at the right side.

- Camera Settings (center second place): Setting the camera controls, and
- IP Configuration (center third place): Configuration of the IP address.

When the user clicks on Experiment settings, the selectable test setups are shown. The application includes three different setups:

- Robot: The robot is shown alone in the environment (see Figure 6.11).
- Robot with Specimen: The robot is connected directly with three vertebral body or spine shown in Figure 6.11 (a).
- Robot with specimen and bracket: The robot is in Figure 6.11 (b) visualized with specimen holder (bracket) connected to the spine.

These options were programmed in order to change the initial position of robot if the experiment setup changes (e.g. different tool at the end-effector) or just visualize path planning or to test control architectures.

The camera perspective is arbitrarily changed. To change the perspective, the camera can move in the space. For this process two adjacent usable control concepts have been realized:

- Sidebar menu: Camera with control panel at the right side and
- Sidebar menu hidden: Camera where control panel is not visualized.

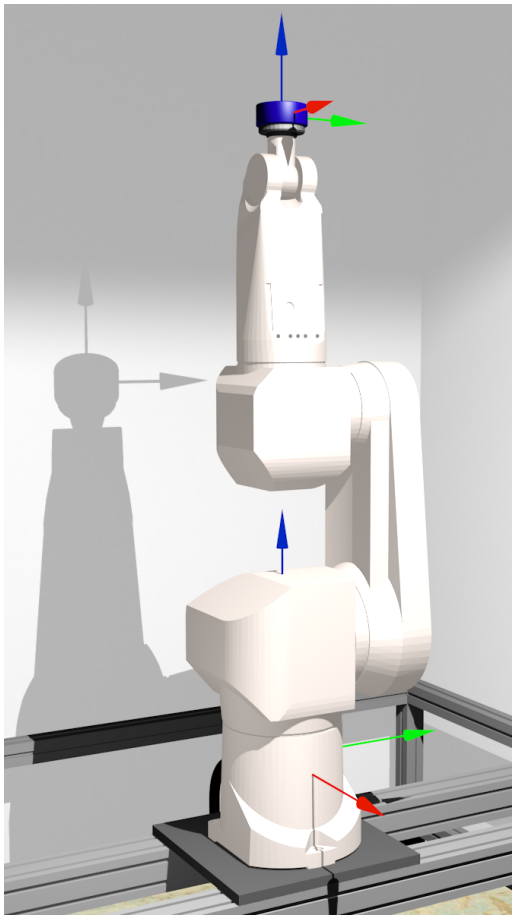

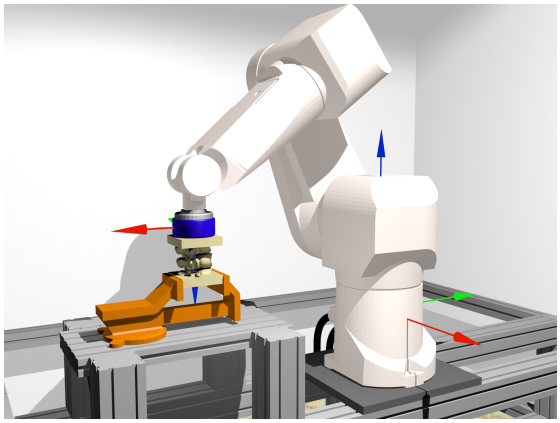

(a) Robot directly connected to specimen.

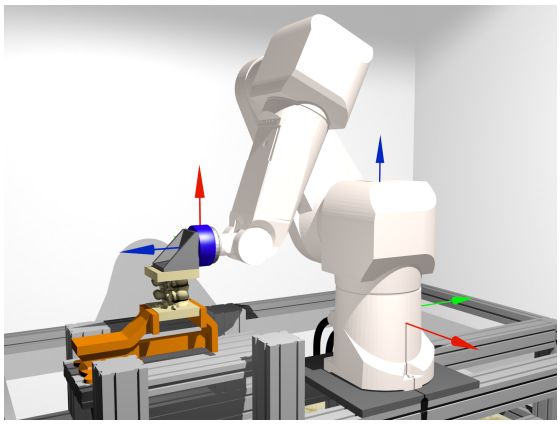

(b) Robot with three vertebral body and bracket (tool to attach the specimen to the sensor)

Figure 6.11: Robot in the environment.

In the control panel, each degree of freedom of the camera is shown by an icon with an arrow. If one of them is clicked, the camera moves along the direction of the arrow. Under the arrow symbols, there are three other functions buttons called *Main Menu*, *Save View* and *Quit*:

- Main Menu: Makes the transition of the program in the main menu,
- Save View: Saves the current camera position and
- Quit: Exits the visualization and closes the application.

The control panel can be hidden or visualized when the key *M* is pressed.

Other functionalities have been programmed. The complete keyboard shortcuts is shown in Table 6.1:

Table 6.1: Keyboard shortcuts to control the movements of the camera.

Function	Key
Translation of the camera - left	←
Translation of the camera - right	→
Translation of the camera - up	↑
Translation of the camera - down	↓
Translation of the camera - zoom in	+
Translation of the camera - zoom out	-
Rotation of the camera - left	SHIFT and ←
Rotation of the camera - right	SHIFT and →
Rotation of the camera - up	SHIFT and ↑
Rotation of the camera - down	SHIFT and ↓
Inclination of the camera - left SHIFT and	+
Inclination of the camera - right SHIFT and	-
Front view	1
Diagonal view	2
Side view	3
Top view	4
Specimen diagonal view	5
Saved custom view	BACKSPACE
Enable or disable the control panel	M
Termination of the application	SPACE

6.2 Embedding Process of Specimens

The protocol to embed three vertebra is described as follows:

1. **Define a plane** where the middle vertebra is horizontal. This can be accomplish with the help of a 3 DoF monopod. It simplifies the modification of the height and two angles of rotation. The process to define a plane can be done with a previous CT and define the plane with needles. The monopod can hold the vertebra by fastening it direct to the specimen as shown in Figures 6.12 and 6.13.

2. **Embed the lower part of the specimen**. A plastic bucket should be sprayed with a parting compound called “ALPA-SEP Super” (Alpina - Technische Produkte, Geretsried, Germany) and after a reaction time of 10 minutes is possible to infuse the fluid resin. This, together with the malleability of the plastic bucket, facilitates the removal of the resin after the solidification process. Figures 6.14 and 6.15 show this process.

3. **Turn around the specimen**. In order to embed the other end of the specimen, the hart resin is attached to the monopod. A metal tool, shown in Figure 6.16, is fixed with three screws to the hart resin. In order to facilitate the process of insertion of the screws it is recommended to bore three small holes. After that three metal screws can be inserted easily. The first horizontal plane (step 1) is kept with the

help of a bubble level shown in Figure 6.17. Thus it is possible to embed the other end of the specimen.

4. **Embed the upper part of the specimen**. Changing the height of the monopod it is possible to introduce the free end of the vertebra inside the bucket. After spraying it with the parting compound and waiting for 10 minutes, the fluid resin can be infused like it is shown in Figure 6.18.

5. **Attach aluminum block**. The dimensions of the resin are big enough to make difficult the process of clamping the specimen for testing. Therefore an aluminum block was constructed and attached to the resin. Again 4 small holes where bore in advance to facilitate the insertion of the 4 screws as shown in Figure 6.19.

6. **The specimen is ready to be tested**. The lower part, where the aluminum block has been attached, can be clamped by a vise. The upper part can be fix to the FTS with 4 screws like Figure 6.20 shows. Thus the specimen is ready to be tested by the robot.

Figure 6.12: Specimen.

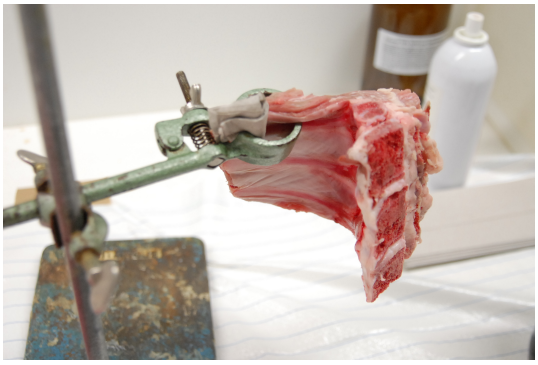

Figure 6.13: Fixation of specimen with the monopod.

Figure 6.14: Embedding the lower part of specimen.

Figure 6.15: Removal of plastic bucket.

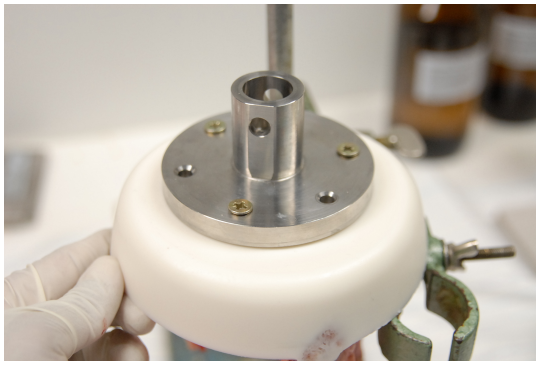

Figure 6.16: Fixation of tool.

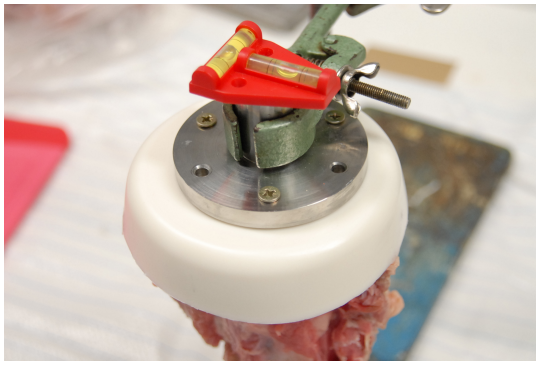

Figure 6.17: Defining a plane.

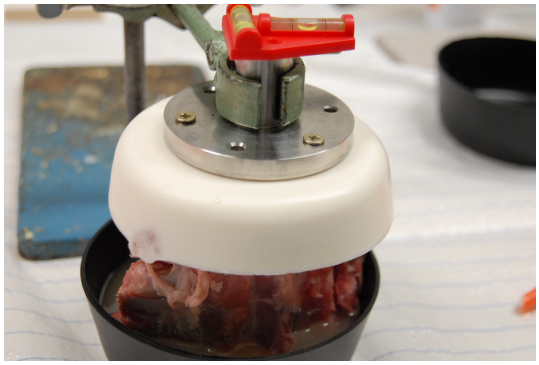

Figure 6.18: Embedding lower part.

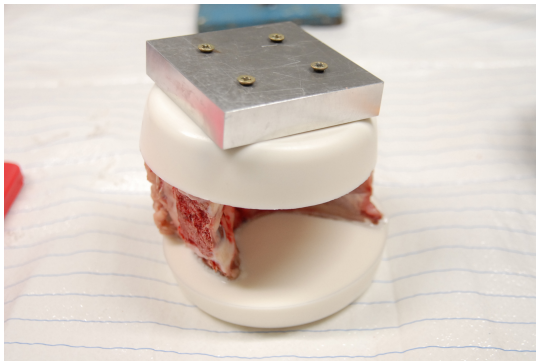

Figure 6.19: Attachment of aluminum block.

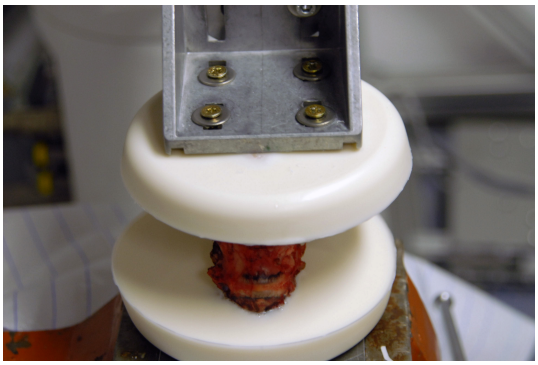

Figure 6.20: Specimen attached to tool.

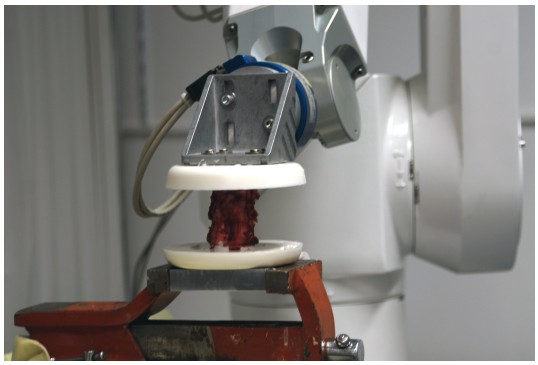

Figure 6.21: Specimen attached to robot.

7 Experiments and Results

The project concept explained in chapter 4 and the control strategies shown in chapter 5 were used in order to perform specific tests with different materials. In this chapter two main experiments are explained:

1. Experiments with non-biological specimens
2. Experiments with biological specimens

The first kind of experiments are all those tests where the materials are non-biological. Here are described all test that were performed to test the control strategies already exposed. The goal of these experiments is to give an idea about the results that may come when biological specimens are under load applied by the robot. These materials do not have a decomposition process and they are isotropic what makes them very suitable to perform the first tests. The second kind of experiments are all those tests with biological specimens. The bodies of study are here cadaveric specimens which undergo a decomposition process and should be tested in the shortest possible time.

7.1 Experiments with non-biological Specimens

In order to perform *in vitro* biomechanical tests it is necessary to load the body or specimen with different forces and moments in a given coordinate system. These loads can be produced by a universal testing machine, or complex system that allow the application of loads in more than one degree of freedom. Several tests define a global and one or more local coordinate systems in order to define the direction of the applied force or moment. These forces and moments may be applied separately or combined. Thus it is possible to create a protocol where the specimen will be tested in order to describe its properties.

Several systems to test spines use robotic arms [60, 143], Stewart platforms [62, 141] or other complex machines [59, 63, 132, 154] to perform the so called "pure moment" approach, a very well accepted method described by Panjabi [119]. This is understood as an applied rotation about a specific axis on the body while five remaining degrees of freedom (DoF) are left unconstrained. Most of the machines that perform such rotations are equipped with a 6 DoF Force Torque Sensor (FTS) in order to report 3 forces and 3 moments in three spatial axes.

In mechanical engineering a moment is defined as the tendency of one or more forces to rotate an object about an axis. Its mathematical quantity is calculated as the product of the force and the perpendicular distance from a point of rotation, to the line of action of the force (equation 7.1).

$$\mathbf{M} = \mathbf{r} \times \mathbf{F} \tag{7.1}$$

where $\times$ is the cross product, $\mathbf{M}$ is the moment, $\mathbf{r}$ is the vector from a fixed point to the position where $\mathbf{F}$, force, is applied. A couple is a distribution of forces with a resultant moment different from zero and resultant in force equal to zero. A couple has the property of being independent of a reference point. The simplest example of a couple consists of two equal but opposite forces whose lines of action do not coincide. The aim of this work is to evaluate different setups with simulations and experiments in order to achieve a "pure moment" and illustrate the difficulties to perform it, and describe finally the impossibilities in the praxis.

All research groups like Wilke [153,154], Goertzen [62] or Gèdet [59] use different machines to apply moments and forces to test specimens. However, all of them use a general setup to test biological specimens (shown in Figure 7.1). A machine (denoted by A) composed of pulleys and cables or orthogonal stepper motors or robotic systems generate specific movements to test the specimen. To measure forces and moments a FTS (denoted by S) is then attached to the machine. In order to attach the tested body to the sensor an interface (denoted by I_1) is needed. This can be a clamp mechanisms or a tool with several screws. The other side of the specimen (denoted by B) has to be fixed to another interface or platform (denoted by I_2). This can be a linear slider, a six axes load cell or just a vise. All these four components introduces errors, artifacts and can lead to false data, wrong conclusions and the impossibility to compare data with other setups.

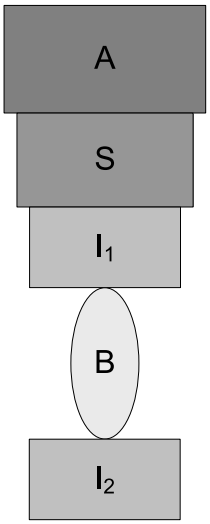

Figure 7.1: General setup to test a specimen. A refers to any mechanism to produce a specific combination of forces and moments. S refers to sensor, I is the interface where a fixation between two different bodies take place. B refers to body to be tested.

7.1.1 Materials and Methods

Two methodologies were used in this work. The first one deals with simulations in order to treat the problem analytically. The second one deals with experiments on physical bodies under strain to compare the results of the simulation.

Simulation

In order to analyze the process of applying a moment on a body it was necessary to perform several simulations. Therefore the software ANSYS® was used to this purpose. Two reference bodies were modeled and loaded with a pure moment to be analyzed with the program tools. Even when it is not necessary to use finite element theory to solve this analytical problem, this software provides a graphical representation of the stress, load and force distribution inside the body.

The material has the following properties: Young module = 1GPa, Poisson ratio = 0.3, moment applied = 5 Nm. Their dimensions are shown in Figure 6.2.

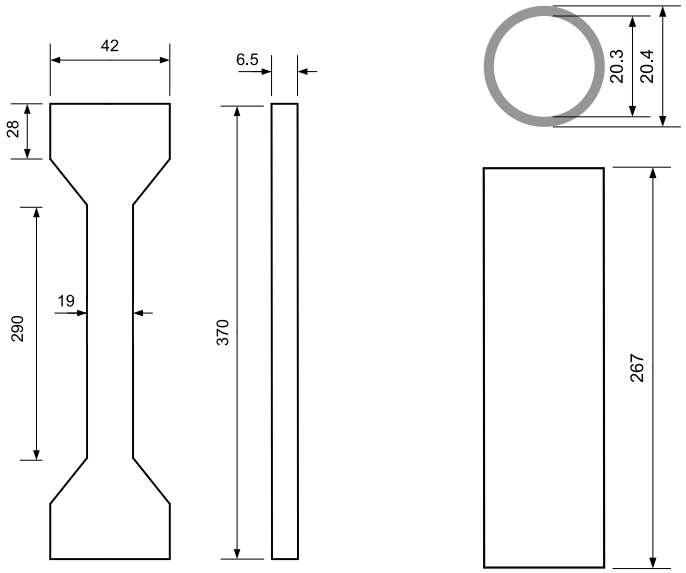

(a) Body 1 (b) Body 2

Figure 7.2: Dimensions in mm of body 1 and body 2.

Test

Two different physical bodies were tested with two different robots. In order to perform the experiments the following materials were used:

- As robots:
  - 12 DoF robot Stäubli RX 90-B
  - 7 DoF DLR Light-Weight Robot III (LWR III)
- Rest of materials:
  - FTS with 12 DoF JR3 Inc., USA
  - Clamp mechanism
  - Two different test bodies

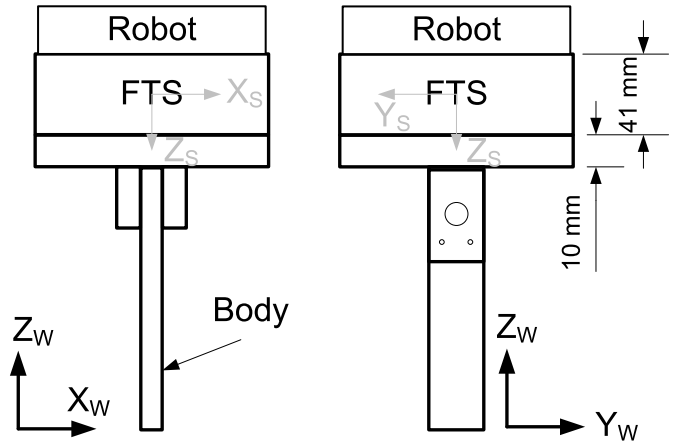

Figure 7.3: Clamp attached to the body with one screw and two metal bars. The global coordinate system is shown in the side view (left) and front view (right). The coordinate system of the sensor is located in the middle of it. Dimensions are given in mm.

- Vise
- Low friction linear slider

The RX 90-B was used in order to load two physical bodies. The FTS was attached to the last degree of freedom of the robot. The RX 90-B was operated under direct force control [83, 134] where the feedback loop is closed with force-moment signals.

In a further approach the robot was operated under hybrid control. Both, position and force reference values can be commanded to the robot [29].

A second robot, a DLR LWR III, was used in oder to load the two bodies of study. The control architecture used was a combination between an impedance control [66] and a direct force control.

A 12 DoF FTS described in section 4.2.5 was used.

Two experimental bodies where chosen in order to perform experiments and to compare the results with the simulations. Both are made of a homogeneous polymer and their dimensions are shown in Figure 6.2. In order to attach the bodies to the sensor a clamp was developed.

Figure 7.3 shows this mechanism. The thickness of the flange is 10 mm. Two holes of 1.5 mm of diameter and one of 5 mm of diameter must be done in order to introduce a screw and two metal bars. This procedure prevents the translation and rotation of the body in the clamp.

A low friction linear slider was used. It contains four linear ball bearing systems which ride on linear rails allowing a free movement in 2 DoF.

A vise was used to attach the test bodies to a fix place.

7.1.2 Experiments

Three different experiments were perform:

- Experiment 1. The RX 90-B under direct force control was used. All bodies were fixed at the lower end with a vise. The upper end was fixed to the FTS with the clamp. In this way, the upper end of the body was free to move in the 6 DoF (3 axes of translation and 3 axes of rotation). A global (world) coordinate system (shown in Figure 7.4) was used. All forces and moments were controlled and measured in the sensor coordinate system. All force-moment profiles have a rise time of 20 seconds. The robot begins the movement from a unloaded initial position. This means that the signals of the FTS are zero at the beginning of the experiment. The two bodies were loaded with the following reference values:
  - Moment about X axis of ± 3 Nm, all other forces and moments equal zero
  - Moment about Y axis of ± 3 Nm, all other forces and moments equal zero
  - Moment about Z axis of ± 3 Nm, all other forces and moments equal zero

  Figure 7.4 shows the setup of this experiment.

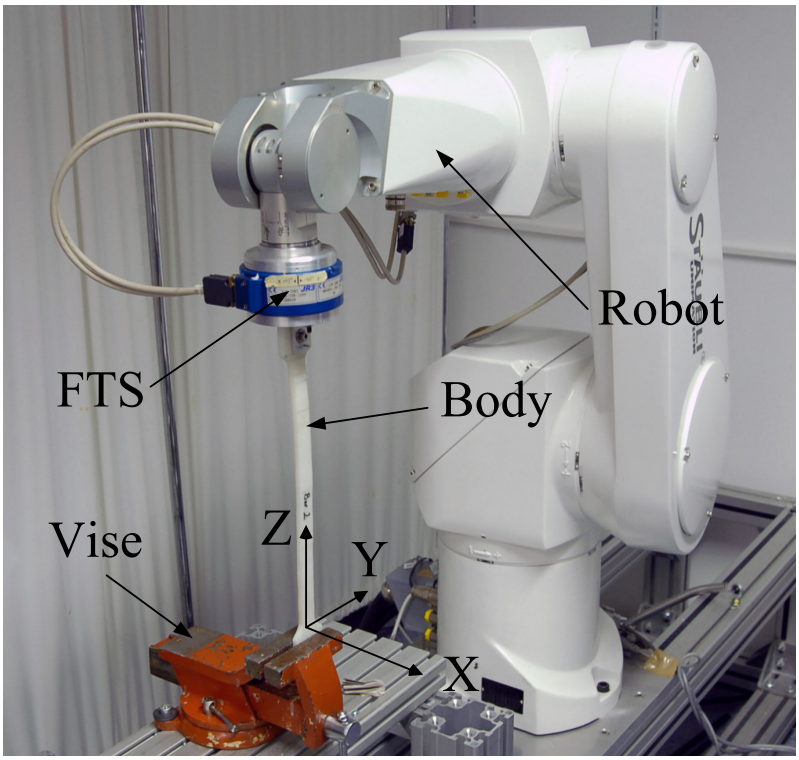

Figure 7.4: Body 1 attached to Stäubli RX90-B.

- Experiment 2. The LWR III under impedance control was used. The reference value in force-moment reaches its desired value after 5 seconds. All other conditions are maintained from experiment 1. Figure 7.5 shows the setup of this experiment.

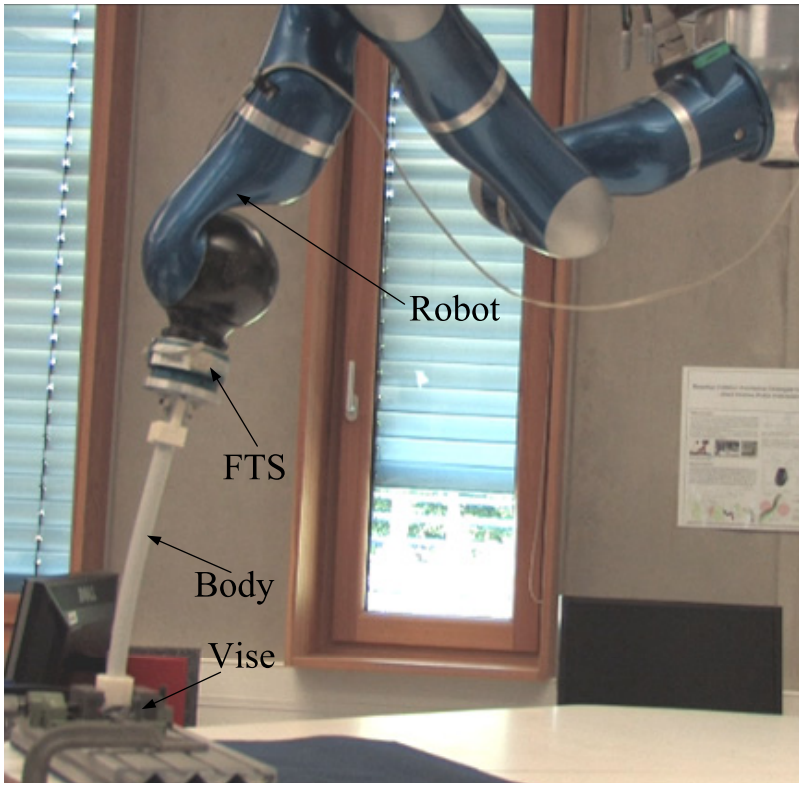

Figure 7.5: Body 2 attached to DLR LWR III.

- Experiment 3. The RX 90-B under hybrid control was used. The movement along Z axis was made under force control while all other movements and rotations axes were made under position control. This allows the movement of the robot along Z axis depending on the force commanded. A rotation was commanded in order to actuate just one joint of the robot until a moment value is sensed. The upper end of the body was attached to the FTS with the clamp. The lower end was attached to the linear slider. In this way the whole construction allows the movement of the body in 4 DoF: 2 DoF of the linear slider, 1 DoF controlled by force (up and down along Z axis) and 1 DoF where only one joint of the robot rotates (rotation about X axis). All reference values reach their desired value after 20 seconds. The robot begins the movement with an unloaded weight in the sensor. The three bodies were loaded with the following reference values:

  – Positive and negative rotation about X axis until a moment of ± 3 Nm is sensed. Force in $Z = 0$

  Figure 7.6 shows the setup of this experiment.

These three experiments are resumed in Table 7.1.

7.1.3 Results

In simulation, a pure moment about $-X$ axis was applied to the first body in the program ANSYS®. Figure 7.7 shows the stress distributed along the body when a pure moment of

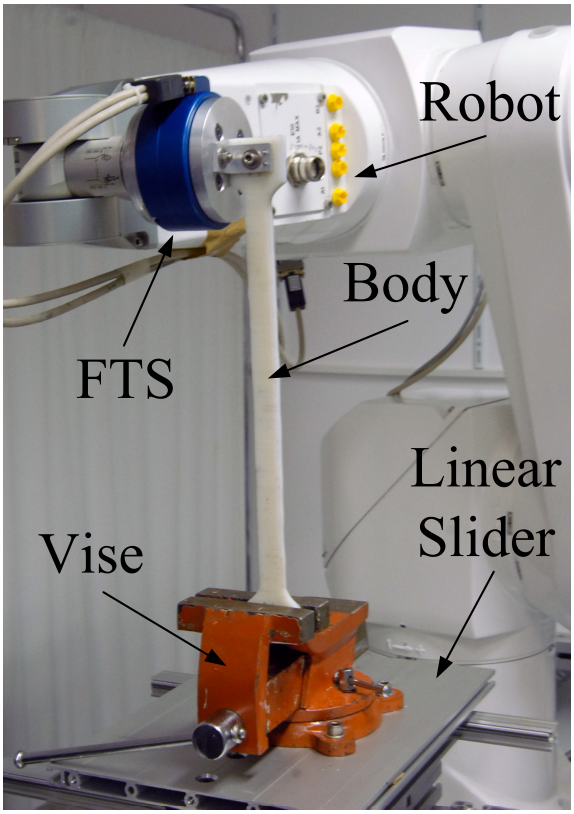

Figure 7.6: Linear slider and Stäubli RX90-B attached to body 1.

Table 7.1: Resume of experiments with non-biological bodies.

Experiment	Robot	Control	Fixation
1	Stäubli RX90	Direct Force Control	Vise
2	DLR LWR III	Impedance	Vise
3	Stäubli RX90	Hybrid	Linear slider

5 Nm is applied. The stress along the body is distributed in such way that in the center of the body are no stresses or strains (the so called neutral axis). Thus, one side of the body is being compressed while the other is tensed. The program shows the absolute value of the stresses and both surfaces appears with the same color along the transversal line.

Figure 7.8 shows the force distribution along a section of the body. The forces actuating on one side of the body have the same magnitude but opposite direction than the forces on the other side of the body.

Figure 7.9 shows a cycle where a positive moment about Z axis was applied to the body 1 in experiment 1.

Table 7.2 shows the results of the two first experiments. It can be seen that in experiment 1 with body 1, when a positive moment was applied about X axis, a force of 2.87 N along Y axis was present. If a point is chosen at the very end of the body (370 mm from body + 10 mm from clamp + 20.5 mm from sensor = 400.5 mm) and calculate the moment

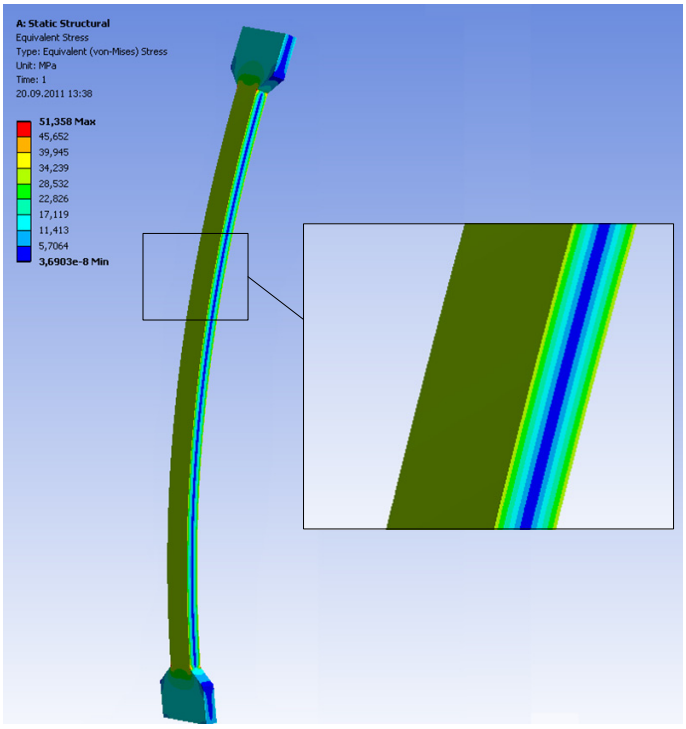

Figure 7.7: Stresses distributed along body 1.

that this force produces, it results 1.15 Nm about X axis which represent the 38.3% of the commanded moment (3 Nm) about the same axis and direction.

The results of the experiment 2 show that the forces are even higher than in experiment 1. When a positive moment was applied about Y axis on body 1 it is possible to see a mean force along X axis of 19.84 N. A moment at the very end of the body (267 mm) induced by this force is equal to 5.90 Nm about -Y axis which is even higher than the moment commanded (+3 Nm given a resultant moment of -2.9 Nm).

Table 7.3 shows the results of experiment 3. Here it was possible to induce just one rotation about X axis. In this way, the robot stops the rotation when a moment of ± 3 Nm is sensed. In the body 1 by a positive rotation, the FTS reported a value of -0.44 N, -1.66 N and 0.62 N in X, Y and Z axes respectively while the mean moment values about Y axis was 0.11 Nm and about Z -0.09 Nm. Taking a point at the very end of the body 1 and calculating the moment induced by the force along Y axis, it results in 0.66 Nm about -X axis. This represents the 22% of the commanded moment.

7.1.4 Discussion

The results of the simulation demonstrate that it is possible, analytically and theoretically, to apply a pure moment on a rigid body. The resultant force is equal to zero and the resultant torque is different from zero. The distribution of the forces are such, that they cancel the resultant force (Figure 7.7). It is important to note that the body in the simulation is free to move. One end of the body is attached and cannot be displaced or rotated. The other end can both translate and rotate.

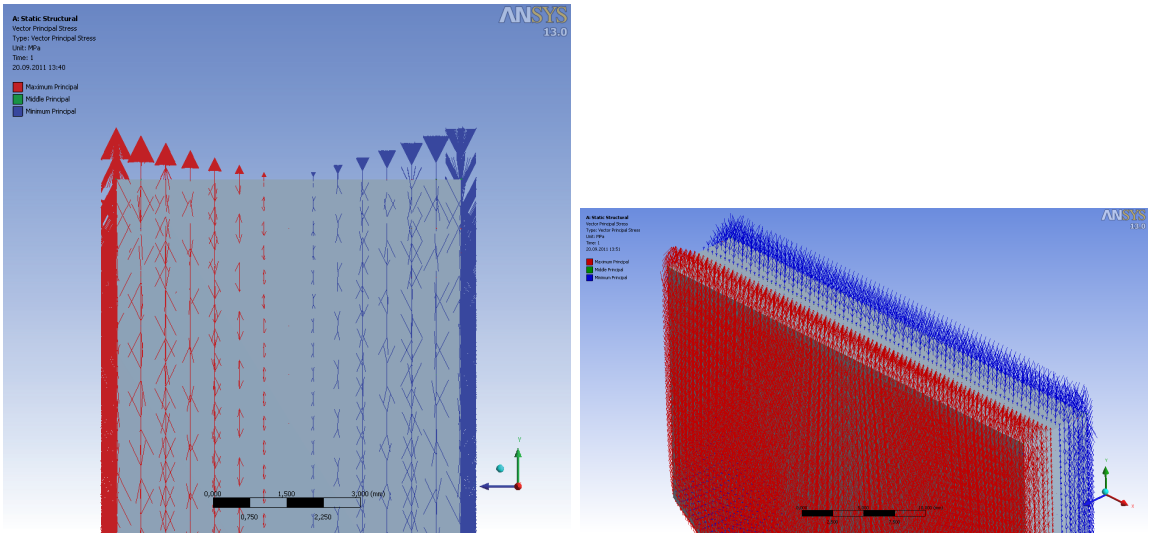

(a) (b)

Figure 7.8: Force distribution in body number 1. a) Front view. b) 3 dimensional view

However, the experiments with the robots and the FTS sensor show that "pure moments" are not possible to apply. The resultant forces that the sensor measures are not zero in any axis. Even the moments about other axis are different from zero. Both bodies are composed of the same material and have simple geometries. In this study an industrial robot was used in experiment 1. It presents massive links and high friction. The usage of a light weight robot in experiment 2, which links are light and the friction is lower than in an industrial robot, showed bigger forces along all axes. Three control approaches (direct force, hybrid and impedance) were used in different combinations to intend to minimize forces in all axes. Direct force control presented apparently low forces (experiment 1). Impedance together with direct force control (experiment 2) brings more stability to the system but higher forces in all axes. Two different interfaces, vise (experiment 1 and 2),

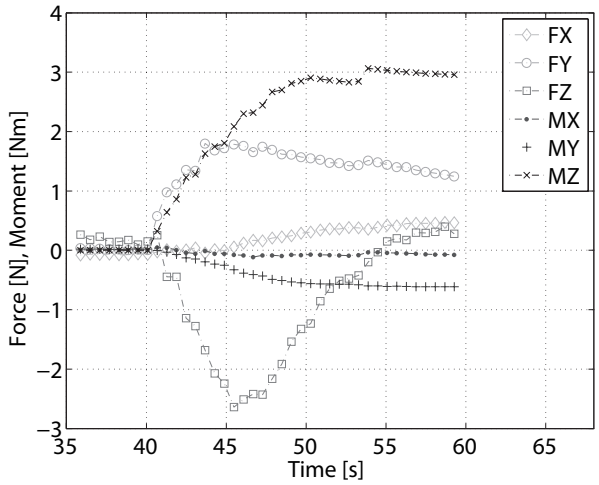

Figure 7.9: Cycle of applying a moment of 3 Nm about Z axis in body 1 under conditions of experiment 1.

Table 7.2: Mean errors of experiment 1 and 2 by positive and negative applied moments about a single axis. Forces are given in [N], moments in [Nm]. The commanded moment is represented by –.

Positive moment						Negative moment					
F_x	F_y	F_z	M_x	M_y	M_z	F_x	F_y	F_z	M_x	M_y	M_z
Experiment 1. Body 1											
-0.57	2.87	-0.53	–	0.24	0.15	-0.60	-3.13	-0.17	–	0.14	-0.19
-3.84	0.90	0.41	-0.02	–	0.18	2.43	0.22	1.66	0.39	–	-0.03
0.17	1.10	-0.63	-0.04	-0.33	–	-0.70	-1.30	-1.22	0.15	-0.02	–
Experiment 1. Body 2											
-0.55	2.64	-1.26	–	0.20	0.04	-0.23	-2.82	0.92	–	-0.02	-0.06
-0.81	0.16	0.85	-0.05	–	0.02	1.35	-0.36	1.07	0.05	–	-0.19
-0.63	0.20	0.24	-0.04	0.10	–	0.63	0.01	1.06	0.14	-0.11	–
Experiment 2. Body 1											
3.68	-7.28	3.03	–	1.15	-0.26	6.42	13.04	12.69	–	1.93	-0.29
19.84	-0.32	4.33	0.16	–	-0.10	-22.92	-3.70	3.44	0.39	–	0.19
18.29	-4.42	1.91	2.54	6.86	–	-19.90	-12.82	-3.25	2.48	-7.29	–
Experiment 2. Body 2											
0.99	-9.13	5.71	–	0.38	-0.01	-1.64	19.10	0.29	–	-0.30	0.03
23.83	-1.12	1.34	0.56	–	0.15	-22.38	-2.88	4.41	0.41	–	-0.13
3.84	4.94	-0.31	-1.85	0.43	–	-0.55	-1.84	-0.64	1.32	0.80	–

Table 7.3: Mean errors of experiment 3 by positive and negative rotation about a single axis. Forces are given in [N], moments in [Nm]. The commanded moment is denoted by –.

Positive rotation						
Body	F_x	F_y	F_z	M_x	M_y	M_z
1	-0.44	-1.66	0.62	–	0.11	-0.09
2	-0.09	0.40	1.13	–	-0.03	-0.01
Negative rotation						
1	0.58	0.62	1.32	–	-0.20	0.14
2	0.16	-1.08	1.16	–	-0.07	-0.01

and linear slider (experiment 3) were used to fix the specimen. The usage of a vise brings the advantage of constraining the lower end of the specimen, allowing the upper end to move in 6 DoFs. The linear slider together with the robotic setup constrained the overall movement of the specimen in only 4 DoFs. However, with none of these setups was possible to apply a pure moment.

In all experiments can be seen that forces and moments in all axes are present. Some forces produce a moment even higher than the commanded moment. It was expected that in experiment 3 the low friction linear slider would reduce these forces. However it is possible to see that forces and moments are present in all axes.

This problem can have several reasons. The first one is the way how the force is measured. The forces and moments are calculated with strain gages attached to a cross. This means

that these kind of sensors are not capable to measure a specific distribution of forces.

Other source of error is the clamp to attach any body to the sensor. This will bring no linearities and will also prevent to apply a specific distribution of forces on the body.

The friction of the linear slider cannot be completely eliminated. Such system have to move masses (panel, linear slider, vise) and their inertia plays an important role when trying to avoid these forces.

The control approach and its frequency influences also the results. The performance of the controller affects directly the movements of the end-effector.

The sources of error are resumed in Table 7.4.

Table 7.4: Summary of sources of error in a spine testing apparatus.

Component	Error description	Evaluation of introduced error
A	Precision in the movement. Allows quasistatic and dynamic testing possibilities	Low
S	It cannot sense a distribution of forces. It is not possible to sense force or moment in a direct way	High
I_1	It brings non linearities in the way of fixation.	High
I_2	Friction, movement of massive bodies and inertias. It constraints the motion of the specimen	Middle
Controller frequency	It can produce slow reactions of the robot and therefore forces and moments may be present even if the commanded value is zero	High
Control approach	It can bring instabilities to the system. Its performance is directly related to the accuracy in following defined force and position profiles	Very high
Distance	Distance between sensor and the point of interest brings an extra undesired moment	Very high

These experiments show that it is not possible in reality to apply a pure moment on a rigid body. Therefore, it is only possible to induce a moment about an axis and to minimize forces and torques in all others. This is a very important parameter when testing specimens. The location where the forces and moments are measured has to be given and the distance from this position to the specimen. If a 2 or more DoF sensor is used, all forces and moments should be reported.

The rotation of a single axis of a defined coordinate system of a body should not be confused with the term pure moment.

7.2 Experiments with Biological Specimens

Biomechanical tests methods normally consist in applying a moment in a specimen about a specific axis while the rest of degrees of freedom are unconstrained. As it is already demonstrated, pure moments are not possible to be applied. Therefore, in this study are

reported the moment commanded and the forces and moments are induced along and about other axis while testing. Other authors have already used a robot to load biological specimens (see section 3.1). Some groups apply a position control [143], others apply a hybrid control [60] where at least one of the axis is controlled under position control. In order to achieve the predefine loads, the need of a stiffness matrix is needed which has to be updated during each iteration [60, 141, 147]. The experiments in this study exposed present a new methodology where direct force control (section 5.5) was applied.

7.2.1 Materials and methods

A fresh porcine lumbar spine L3-L5 was used. All muscle tissues were removed while leaving intact all ligaments and bony tissue. Both sides of the spine (L3 and L5) were embedded in resin (section 6.2) and attached to the vise from the lower side and to the sensor with a bracket from the upper side (Figure 7.10).

A gravity compensation of the tool shown in section 5.6 was used. Figure 7.10 shows the specimen after applying the embedded process described in section 6.2.

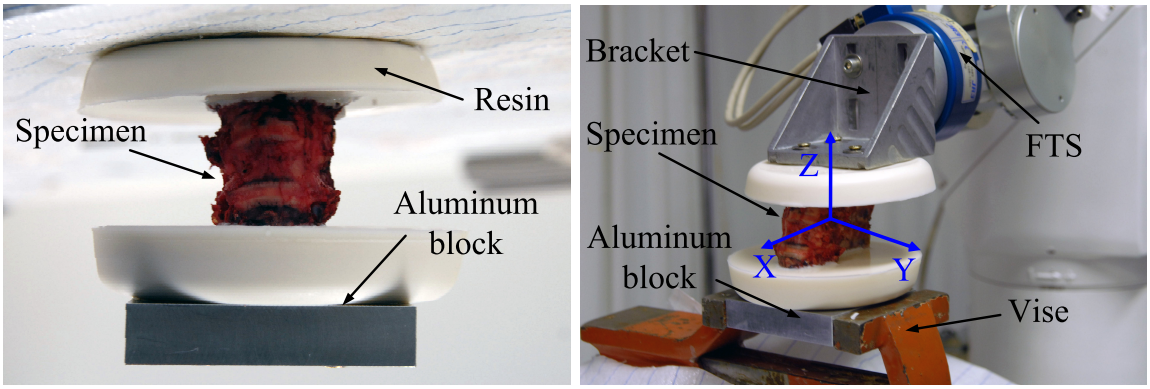

(a) (b)

Figure 7.10: a) Porcine spine L2 with aluminum block. b) Specimen attached to the vise and to the robot.

The 6 DoF robot Stäubli RX90-B under force control was used. The global coordinate system of the spine was aligned with the WCS of the robot as in [157] and shown in Figure 7.11. This is to maintain a plane where the spine can move. The specimen was fixed at the lower end with a vise. The upper end was fixed to the FTS with the clamp. In this way, the spine was free to move in the 6 DoF. The WCS was used in order to control and measure all forces and moments. The force rate in all movements was of 0.075 $^{\mathrm{Nm}}/_{\mathrm{s}}$. The robot begins the movement from an unloaded initial position. After closing the vise, forces around 5 N and moments around 1 Nm were reported. The first movement of the robot is to the position and orientation where the signals of the FTS are zero. Thus a initial position inside the neutral zone is defined. The specimen was loaded with the following reference values:

- Moment about X_W axis (lateral bending, LB) of ± 3 Nm, all other forces and moments equal zero

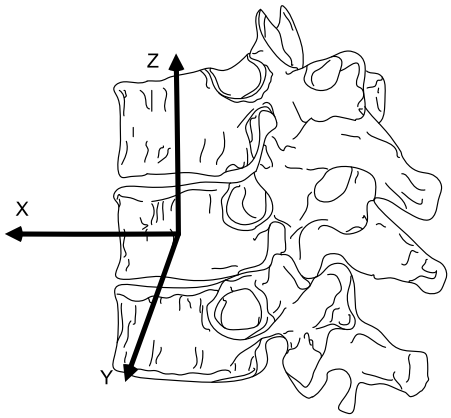

Figure 7.11: Coordinate system of the spine is aligned with the WCS of the robot (see also Figure 7.12).

- Moment about Y_W axis (flexion extension, FE) of $\pm 2\,\mathrm{Nm}$, all other forces and moments equal zero
- Moment about Z_W axis (axial rotation, AR) of $\pm 2\,\mathrm{Nm}$, all other forces and moments equal zero

The distance between the specimen and the FTS can be seen in Figure 7.12. This experiment was three times repeated and the third cycle was reported.

7.2.2 Results

Figure 7.13 shows the sequence of the moments applied on the spine. It can be seen that the maximum forces arise when there is a change in the direction of the commanded moment. The moments about the unconstrained axis stay below the 36% of the commanded value. Figure 7.14 shows the moment-angle curve by FE of the porcine spine. This curve shows the typical hysteresis behaviour. Table 7.5 shows maximum values of forces and moments.

Table 7.5: Maximum and minimum values of force and moment in [N] and [Nm] respectively during the test. The dashes "-" indicate the commanded moment.

	F_x	F_y	F_z	M_x	M_y	M_z
Max	3.67	3.55	11.49	–	0.68	1.71
Min	-5.25	-4.37	-2.86	–	-0.31	-1.58
Max	7.17	4.61	6.37	0.93	–	0.72
Min	-3.52	-4.05	-7.42	-0.62	–	-1.49
Max	7.6	6.80	8.96	0.98	0.76	–
Min	-11.47	-6.05	-4.62	-0.73	-1.24	–

Figures 7.15 and 7.16 show the sequence of FE, LB and AR angles when performing a FE movement. Their peak values are found when the commanded moment reaches its

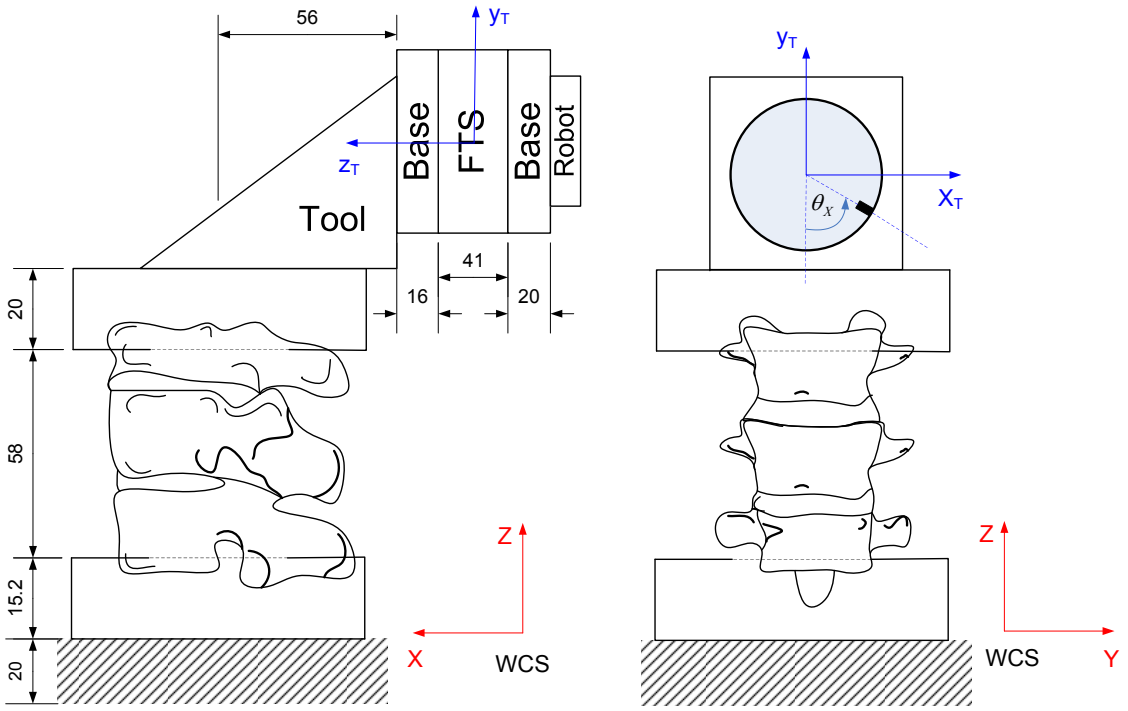

Figure 7.12: Sketch of the tool mounted on the FTS and the distance between specimen and force/torque sensor. All dimensions are given in mm.

maximum value. It can be seen than the FE angle changes in a window of 28.24° having 12.65° as maximum value and -15.6° as minimum. In lateral bending the window is 15.9° having 5.5° and -10.4° as maximum and minimum value respectively. In axial rotation the window is 18.1° with 4.7° and -13.4° as maximum and minimum value respectively. Table 7.6 shows the maximum and minimum values of the angles for every commanded movement.

Table 7.6: Maximum and minimum values of the angles [deg] in FE, LB and AR. The left column represents the commanded movement and the upper row stands for angles measured during the commanded movement.

	FE		LB		AR	
	Max	Min	Max	Min	Max	Min
FE	12.65	-15.60	5.55	-10.71	4.75	-13.95
LB	4.47	-4.34	16.34	-17.44	9.57	-10.51
AR	5.16	-9.94	18.57	-15.23	20.53	-18.97

7.2.3 Discussion

Previous experiments with robots use position control or have to calculate a dynamic stiffness matrix which values have to be determine in each time step. Thus it results in

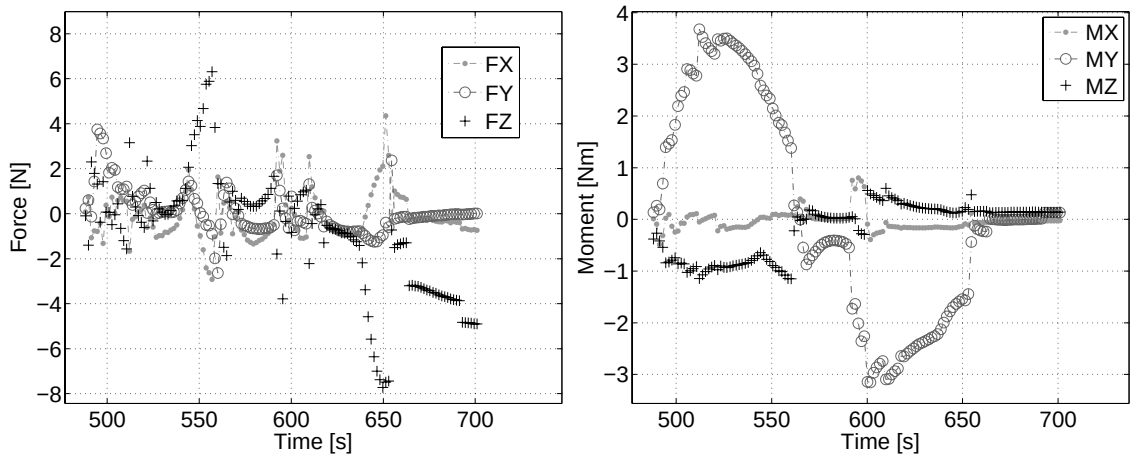

(a) (b)

Figure 7.13: Forces and moments of the third cycle moving the specimen in FE (moment about Y axis). a) Forces. b) Moments.

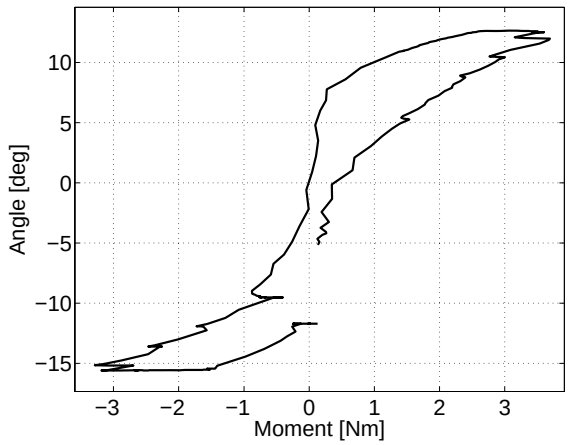

Figure 7.14: Moment-angle response of the motion segment in FE.

a movement with discrete values rather than a continuous. The main disadvantage of these architectures is that the trajectory in position coordinates must be known in advance to ensure proper moments of the robots. This data is very specific for every joint and cannot be found in the literature with high accuracy. The model of the manipulator to test biological specimens can be calculated with enough precision but a detailed description of the particular specimen is difficult to obtain. In such cases the usage of a mere position control for applying loads is a candidate to fail.

Goertzen [62] tested a rabbit lumbar spine with a Stewart platform using a velocity-based force control. He reported forces and moments in the unconstrained axes. However, the control does not show an ability to maintain zero target loads on the unconstrained axes. The forces that act along X and Z reach a maximum value of $\pm 1.5\,\mathrm{N}$ and $\pm 2.5\,\mathrm{N}$ respectively. The distance between the FTS and the specimen was not reported. It is supposed that the forces were measured in the sensor coordinate system. If we take a small distance from the sensor to a point inside the spine, for example 10 cm, we have a

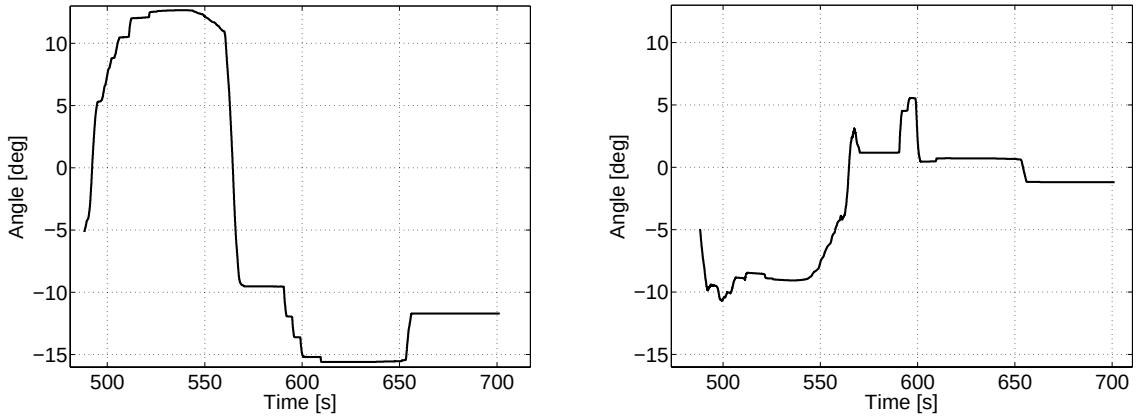

(a) Flexion extension (b) Lateral bending

Figure 7.15: a) Angle of flexion extension movement. b) Angle of lateral bending when a FE movement was commanded.

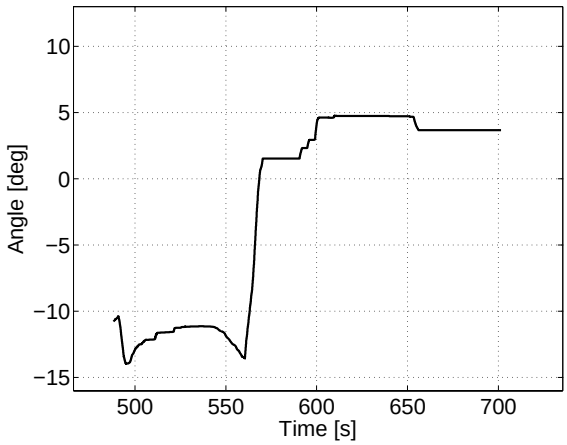

Figure 7.16: Angle of axial rotation when a FE was commanded.

vector of 0.1 m multiplied by 2.5 N gives a moment of 0.25 Nm, which approximates to the commanded moment.

Stokes [141] used a Stewart platform to apply displacements (translations and rotations) to a porcine lumbar spine. By lateral bending and no axial preloaded setup he found a non-smooth hysteresis curve with maximal values of approximately ±1.5 Nm and ±4.5°. Goertzen in [63] tested a porcine cervical spine with a own developed spine tester under position control. He loaded the specimens with ±2 Nm and found a maximum angle by a FE movement of 23.9°. Stokes applied a rotation and measured the moments rather than applying a moment and measure the change in translation and orientation. Goertzen used a porcine cervical spine and not like in this study a thoracic. He used a position control and stopped when a moment of ±2 Nm was sensed. For a flexion extension movement we applied ±3 Nm and the ROM in this particular moment was of 28.24°, which compares well with his results. Comparison with other robotic biomechanical results is limited due to lacks of data and very different setups in the experiments.

As it is already shown, a pure moment cannot be applied. Forces and moments in the

unconstrained axes will arise. The movements of the spine are therefore not constrained to a single plane even when the commanded moment was given about a single axis. Movements of FE will lead to low deviations in lateral bending and in axial rotation. The angles shown in Figure 7.15 do not begin with 0° due to the neutral zone where the spine can move without reporting forces and moments. The third cycle is reported. This leads to a previous movement of the spine under load where the specimen did not return to the exact position (0°) where it began. It returned to a position where moments and forces were zero, that is, to a pose inside the neutral zone. This zone has a high complex geometry and should be treated in a 3-dimensional space, considering all three angles (flexion extension, lateral bending and axial rotation). This phenomenon can be seen also in Figure 7.14 where there is a gap between -12° and -5° when the moment zero is. The hysteresis curve shows a non-smooth line. This can be explained by the moments registered by the FTS. Figure 7.13 shows some peaks at the times 520, 570 and 580. These are reported and plotted together with the angles that this moment produce. All degrees of freedom of the spine are coupled and constraining forces and moments appear.

Direct force control of 6 axes developed in this methodology shows a successful and robust procedure to perform biomechanical tests. Using direct force control in a 6 DoF serial robot opens new possibilities. The specimen can move in the free space without any restriction. The unconstrained axes are actively controlled and not passively avoided. This gives the big advantage that the setup does not have to move big masses and does not have to deal with friction effects due to possible constructions (e.g. gimbal joint, linear slider).

This experiment setup allows a biological and therefore realistic movement in vitro. Three angles for every movement of the spine can be given due to the kinematics of the robot. The controller works with a frequency of 0.5 kHz which enhance the performance of the force control due to the inner feedback loop coming from the FTS [138] giving as a result a high-performance motion control.

8 Conclusion and Future Work

A new system to perform biomechanical tests in 6 DoF is presented which provides a solid foundation to perform complex, robust and scalable biomechanical experiments. A 6 DoF robot and a 12 DoF sensor have been used and a high-performance real-time control has been developed in order to carry on complex tests in biological specimens.

A safety concept was developed providing the protection of damage for the user, for the specimen, for the environment and for the robot itself. Limits in every joint of the robot were defined as well as a 3D box (in Cartesian space) where the robot can safely move and stopping if any of these borders are exceeded.

A modularization of the different tasks as well as a strategic distribution of them in the system architecture, depending on their role within the system, give enough flexibility to adapt it to any kind of specimen or to modify it in order to achieve its best performance. A modular structure, together with a strategic distribution of the modules provides flexibility for the adaptation to different sizes and kinds of specimens. It provides as well scalability, where new sensors, control architectures, and experiment setups can be changed without a big effort and expense of time.

Basic functions have been implemented within the new proposed system to cover different fundamental demands directly related to the robotic arm, such as motion control in the joint space, in the Cartesian space, current commanded motion in both joint and Cartesian space, and interaction control like hybrid control and direct force control to load specimens exerting desired forces and/or moments along/about single axes or in a combination of them. A frequency of 0.5 KHz was achieved providing robustness of any contact control approach.

Using the damped least squares method to calculate the inverse of the Jacobian matrix makes the system robust in the presence of singular configurations of the robot. During the test unexpected high velocities and position deviations in singularities are avoided with this method, providing safety to the specimen and to the user.

The interaction with the framework through a GUI provides a friendly, intuitive and easy way to use the system in order to achieve specific biomechanical experiments. The user is able to operate the robot directly through the user interface. The interaction offers the possibility of starting and stopping the real-time application, configure test parameters (e.g. desired forces and moments to be applied or constants to tune the position or force controllers) as well as read and display signals from the sensors (such as forces and moments occurring during the execution of an experiment) in order to provide additional graphical supervision. It provides also the possibility to automatically save data after the completion of individual experiments. The user interface is designed in such way that the interaction can take place as intuitively as possible and minimize danger to a user or the manipulator itself, restricting the change of certain main parameters responsible for the right performance of the robot.

The system is able to display a virtual 3D environment where the robot and the specimen can be seen, providing a visibility of the test from a close perspective and different angles without being in the range where the robot can move. Since the development and coordination of the experiments take place in an interdisciplinary team, it is imperative that both, engineers and physicians, plan appropriate robot motions during the experiments in order to easily understand the procedure and plan in advance specific protocols in a simulation environment provided from this system architecture.

The control architectures were tested with non-biological and biological materials. Direct force control depends directly on the frequency of the controller due to the feedback inner loop implemented with force/torque signals. The system stability is the main concern when using this control. The direct force control developed in this project was robust enough to ensure stability when testing both types of materials avoiding the vibration of the robot in contact with stiff materials and unknown properties (e.g. compliance) of the biological specimens. It has the advantage that all axes are controlled given a reference value and not passively avoided (like in the case of a linear slider). The system has the advantage to avoid the friction of a complex machine during the movement. It avoids also the movement of big masses and their inertia to compensate or equilibrate the setup for the specimens.

The attachment of bones, muscles, tendons, ligaments and adipose tissues to the testing machine was ensure using a polyurethane resin. It was shown that during all biomechanical experiments, the resin was a reliable chemical mixture to ensure the fixation of biological specimens.

It took approximately 700 seconds (11.6 minutes) to test biological specimens. The time to perform every test was fast enough in order to minimize the changes in the properties of the biological specimen. The system is able to perform different experiments in different time intervals. It has been shown that the biological specimen can be moved in the free space without any restriction. With these experiments it is possible to calculate all those parameters to describe the viscoelastic properties of the specimens (e.g. NZ, EZ, ROM and NZS). The movement of the spine are not constrained to a single plane even when the commanded moment was given about a single axis. Movements of flexion extension will lead to low deviations in lateral bending and axial rotation. This experiment setup allows a biological and therefore realistic movement in vitro of biological specimens.

The contribution of this work is a proposal of a system architecture which makes possible to accomplish high complex test in human and animal joints.

Future Work

A better knowledge of the specimens can provide very useful information to the robot controller. Because every human or animal joint is different, the design of a model that suits all joints becomes very difficult. However, it is possible to gain information about the kinematics of the specimen tracking its movements with an optical navigation system. Thus the possibility to describe a ROM before using the robot to apply loads can be very useful to define clinically relevant movements and their directions when testing specimens with a serial robot. Using information of the navigation system directly in the control architecture is not possible due to the different frequencies of both systems (60 Hz for navigation system and 0.5 KHz for robot). However, this information can be firstly acquired and afterwards

be loaded to describe relevant movements inside the coordinates of the robot. An optical navigation system should be calibrated and be synchronized with the robot. The process of data acquirement should be fast enough to reduce the decomposition process of biological specimens.

Other control strategies can be useful or even more suitable depending on the specific goal of the experiment. Impedance control (see section 5.5) can be one of them. Even if impedance control does not provide the possibility to have a closed-loop in force/moment it can be very useful if it is desired to control the interaction between specimen and robot. A combination between impedance and direct force control can provide more stability to the robot and therefore it would reduce the required time for the experiments. Parallel control [27] can be very useful if the kinematic of the specimen is known, opening the possibility to combine both quantities, position and force, to be passed to the controller. The force control action prevails over the position control action: this means that, when deviations from the planned task occur, priority over position errors is given in weight force errors. Dominance of the force control loop over the position control loop is aimed at obtaining certain deviations from the position trajectory and movement corrections of unplanned contact forces in every situation [134].

The FTS described in section 4.2.5 provides 6 DoF more than conventional force-torque sensors. Linear and rotational accelerations can be used in the control architecture to achieve better results when moving specimens. Even if the movements of the robot are relative slow compared with industrial applications (e.g. automobile industry), an inverse dynamic control together with an acceleration sensor can provide better and smoother movements when testing biological specimens.

A Appendix. Direct Kinematics

When creating a geometric model a body-fixed coordinate system of each link of the robot is assigned, whose position and orientation with respect to a fixed reference coordinate system by the generalized coordinates is uniquely determined. For a known geometry of the connecting links, the coordinates of any point on the robot, relative to the fixed reference and depending on the generalized coordinates, can be determined. Here is explain the procedure to create a geometric model of the Stäubli RX robot 90-B.

The modified Denavit-Hartenberg convention was used in this work. Using the definition of the homogeneous transformations of the form:

$$\boldsymbol{A}_i^{i-1}(q_i) = \boldsymbol{A}_{i'}^{i-1}\boldsymbol{A}_i^{i'} = \begin{bmatrix} \cos\theta_i & -\sin\theta_i & 0 & a_i \\ \cos\alpha_i \sin\theta_i & \cos\alpha_i \cos\theta_i & -\sin\alpha_i & -\sin\theta_i d_i \\ \sin\alpha_i \sin\theta_i & \sin\alpha_i \cos\theta_i & \cos\alpha_i & \cos\alpha_i d_i \\ 0 & 0 & 0 & 1 \end{bmatrix}$$

where

$$\boldsymbol{A}_i^{i-1}(q_i) = \begin{bmatrix} \boldsymbol{R}_i^{i-1} & \boldsymbol{p}_i^{i-1} \\ \boldsymbol{0}^T & 1 \end{bmatrix}$$

and using the DH parameters: where

Table A.1: Denavit-Hartenberg parameters of the Stäubli robot RX 90-B.

Transformation	α [rad]	a[m]	d[m]	θ[rad]
foot $\rightarrow$ 1	0	0	0.42	θ_1
1 $\rightarrow$ 2	$-\pi/2$	0	0	θ_2 - $\pi/2$
2 $\rightarrow$ 3	0	0.45	0	θ_3 + $\pi/2$
3 $\rightarrow$ 4	$\pi/2$	0	0.45	θ_4
4 $\rightarrow$ 5	$-\pi/2$	0	0	θ_5
5 $\rightarrow$ 6	$\pi/2$	0	0	θ_6

$$\boldsymbol{q}(\theta) = \begin{bmatrix} \theta_1 \\ \theta_2 - \frac{\pi}{2} \\ \theta_3 + \frac{\pi}{2} \\ \theta_4 \\ \theta_5 \\ \theta_6 \end{bmatrix} \tag{A.1}$$

Thus, it is possible to write the homogeneous transformation:

$$\boldsymbol{A}_6^f(\boldsymbol{q}) = \boldsymbol{A}_1^f(q_1)\boldsymbol{A}_2^1(q_2)\boldsymbol{A}_3^2(q_3)\boldsymbol{A}_4^3(q_4)\boldsymbol{A}_5^4(q_5)\boldsymbol{A}_6^5(q_6)$$

Thus the geometric model results in:

$$
\begin{aligned}
\boldsymbol{A}^f_{6_{11}} &= -s_6(s_1c_4 + s_4c_1c_{23}) - c_6(s_5c_1s_{23} + c_5(s_1s_4 - c_1c_4c_{23})) \\
\boldsymbol{A}^f_{6_{12}} &= s_6(s_5c_1s_{23} + c_5(s_1s_4 - c_1c_4c_{23})) - c_6(s_1c_4 + s_4c_1c_{23}) \\
\boldsymbol{A}^f_{6_{13}} &= c_1c_5s_{23} - s_5(s_1s_4 - c_1c_4c_{23}) \\
\boldsymbol{A}^f_{6_{14}} &= 0.45c_1(c_2 + s_{23}) \\
\boldsymbol{A}^f_{6_{21}} &= s_6(c_1c_4 - s_1s_4c_{23}) - c_6(s_1s_5s_{23} - c_5(s_4c_1 + s_1c_4c_{23})) \\
\boldsymbol{A}^f_{6_{22}} &= c_6(c_1c_4 - s_1s_4c_{23}) + s_6(s_1s_5s_{23} - c_5(s_4c_1 + s_1c_4c_{23})) \\
\boldsymbol{A}^f_{6_{23}} &= s_1c_5s_{23} + s_5(s_4c_1 + s_1c_4c_{23}) \\
\boldsymbol{A}^f_{6_{24}} &= 0.45s_1(c_2 + s_{23}) \\
\boldsymbol{A}^f_{6_{31}} &= s_4s_6s_{23} - c_6(s_5c_{23} + c_4c_5s_{23}) \\
\boldsymbol{A}^f_{6_{32}} &= s_4c_6s_{23} + s_6(s_5c_{23} + c_4c_5s_{23}) \\
\boldsymbol{A}^f_{6_{33}} &= c_5c_{23} - s_5c_4s_{23} \\
\boldsymbol{A}^f_{6_{34}} &= 0.42 + 0.45c_{23} - 0.45s_2 \\
\boldsymbol{A}^f_{6_{41}} &= 0 \\
\boldsymbol{A}^f_{6_{42}} &= 0 \\
\boldsymbol{A}^f_{6_{43}} &= 0 \\
\boldsymbol{A}^f_{6_{44}} &= 1
\end{aligned}
$$

where the letters s and c stand for sin and cos respectively. The subindex indicates the respectively q_i. Double subindex indicates the sum of the respectively q_i.

B Derivation of the Equation of Motion

Here is described the approach to the development of the dynamic model of the industrial robot Stäubli RX 90-B. It explains how the equations of motion, describing the relationship between the moments in the axes of the robotic arm and its movements, can be calculated using the Lagrange method. Particular attention is paid to the determination of the expressions for the kinetic and potential energy of the robotic arm.

When determining the equation of motion using Lagrange's equations, the *Lagrangian* must be first formulated. The Lagrangian is defined as the difference of the kinetic energy and potential energy of a mechanism:

$$\mathcal{L} = \mathcal{T} - \mathcal{U}$$

where $\mathcal{T}$ is the total kinetic energy and $\mathcal{U}$ is the potential energy of the system.

In Lagrange equations an expression for the moments $\boldsymbol{\tau}$ in the axis of the robotic arm can then be determined:

$$\frac{d}{dt}\frac{\partial \mathcal{L}}{\partial \dot{q}_i} - \frac{\partial \mathcal{L}}{\partial q_i} = \tau_i \text{ for } i = 1, \ldots, 6$$

The kinetic energy of the robotic arm is made up of the sum of the kinetic energy of the links $\mathcal{T}_{l_i}$ and rotors $\mathcal{T}_{m_i}$:

$$\mathcal{T} = \sum_{i=1}^{6} (\mathcal{T}_{l_i} + \mathcal{T}_{m_i}) \tag{B.1}$$

In the classical form, both links and motors will be separately considered. However, a more realistic approach is when the link and the motor mounted on it are considered as a unit. Figure B.1 shows a schematic sketch of such an augmented link with the forces and moments acting.

The plotted quantities have the following meanings:

- $\boldsymbol{f}_i$ Force that link i-1 exerts on link i
- $-\boldsymbol{f}_{i+1}$ Force exerted by link i+1 on link i
- $\boldsymbol{r}_{i,C_i}$ Vector from the point of force application $\boldsymbol{f}_i$ to the center of gravity
- $\boldsymbol{r}_{i+1,C_i}$ Vector from the point of force application $-\boldsymbol{f}_{i+1}$ to the center of gravity
- $\boldsymbol{\mu}_i$ Moment that link i-1 exerts on link i
- $-\boldsymbol{\mu}_{i+1}$ Moment that link i+1 exerts on link i
- $\dot{\boldsymbol{p}}_{C_i}$ Velocity of the overall center of gravity
- $\boldsymbol{\omega}_i$ Angular velocity of the connection element i

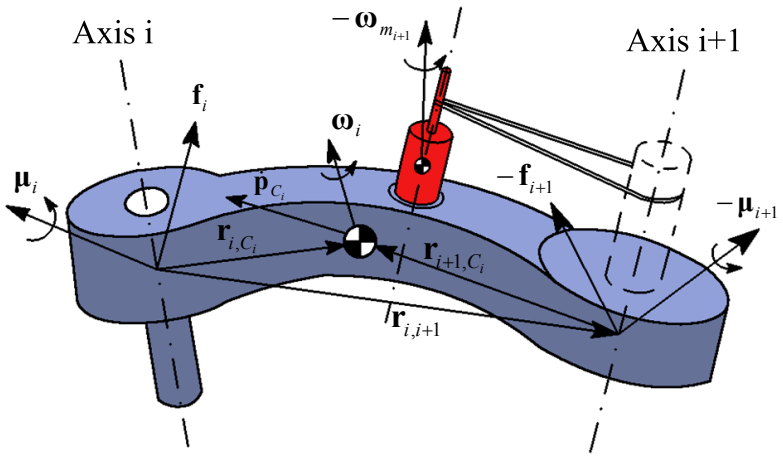

Figure B.1: Schematic sketch of an augmented link. Modified according to Sciavicco [134].

- $\boldsymbol{\omega}_{m_{i+1}}$ Angular velocity of the motor mounted on the connection element i

Furthermore it will be used for the force and torques:

- m_i Combined mass of link i and the motor mounted on it
- $\boldsymbol{g}_0$ Vector of gravitational force
- $\bar{\boldsymbol{I}}_{\boldsymbol{i}}$ Augmented inertia tensor of link i
- $\boldsymbol{I}_{m_{i+1}}$ Inertia tensor of the motor mounted on the connection element i
- $\ddot{\boldsymbol{p}}_{C_i}$ Acceleration the overall center of gravity
- $\dot{\boldsymbol{\omega}}_i$ Angular acceleration of link i

Thus equation (B.1) can be rewritten as:

$$\mathcal{T}_i = \mathcal{T}_{l_i} + \mathcal{T}_{m_{i+1}} \tag{B.2}$$

where

$$\mathcal{T}_{l_i} = \frac{1}{2} m_{l_i} \dot{\boldsymbol{p}}_{l_i}^T \dot{\boldsymbol{p}}_{l_i} + \frac{1}{2} \boldsymbol{\omega}_i^T \boldsymbol{I}_{l_i} \boldsymbol{\omega}_i \tag{B.3}$$

$$\mathcal{T}_{m_{i+1}} = \frac{1}{2} m_{m_{i+1}} \dot{\boldsymbol{p}}_{m_{i+1}}^T \dot{\boldsymbol{p}}_{m_{i+1}} + \frac{1}{2} \boldsymbol{\omega}_{m_{i+1}}^T \boldsymbol{I}_{m_{i+1}} \boldsymbol{\omega}_{m_{i+1}} \tag{B.4}$$

In a first step, the expression for the kinetic energy $\mathcal{T}_i$ is determined on the center of gravity of augmented link i. The position vector $\boldsymbol{p}_{C_i}$ to the center of gravity of an augmented link is defined by:

$$\boldsymbol{p}_{C_i} = \frac{m_{l_i} \boldsymbol{p}_{l_i} + m_{m_{i+1}} \boldsymbol{p}_{m_{i+1}}}{m_{l_i} + m_{m_{i+1}}} \tag{B.5}$$

Furthermore, the vector from the center of gravity of the augmented link i to the center of gravity of link i and the vector from center of gravity of the augmented link to the rotor

i+1 are defined respectively as:

$$\boldsymbol{r}_{C_i,l_i} = \boldsymbol{p}_{l_i} - \boldsymbol{p}_{C_i} \tag{B.6}$$
$$\boldsymbol{r}_{C_i,m_{i+1}} = \boldsymbol{p}_{m_{i+1}} - \boldsymbol{p}_{C_i} \tag{B.7}$$

The linear velocities of the center of gravity of link i and rotors i+1 relative to the center of gravity of the augmented link i are therefore:

$$\begin{aligned}\dot{\boldsymbol{p}}_{l_i} &= \dot{\boldsymbol{p}}_{C_i} + \boldsymbol{\omega}_i \times \boldsymbol{r}_{C_i,l_i} = \dot{\boldsymbol{p}}_{C_i} + \boldsymbol{S}(\boldsymbol{\omega}_i)\boldsymbol{r}_{C_i,l_i} \\ &= \dot{\boldsymbol{p}}_{C_i} - \boldsymbol{S}(\boldsymbol{r}_{C_i,l_i})\boldsymbol{\omega}_i \end{aligned} \tag{B.8}$$
$$\begin{aligned}\dot{\boldsymbol{p}}_{m_{i+1}} &= \dot{\boldsymbol{p}}_{C_i} + \boldsymbol{\omega}_i \times \boldsymbol{r}_{C_i,m_{i+1}} = \dot{\boldsymbol{p}}_{C_i} + \boldsymbol{S}(\boldsymbol{\omega}_i)\boldsymbol{r}_{C_i,m_{i+1}} \\ &= \dot{\boldsymbol{p}}_{C_i} - \boldsymbol{S}(\boldsymbol{r}_{C_i,m_{i+1}})\boldsymbol{\omega}_i \end{aligned} \tag{B.9}$$

Using Equations (B.3) and (B.8), $\mathcal{T}_{l_i}$ can be redefined as:

$$\begin{aligned}\mathcal{T}_{l_i} &= \frac{1}{2} m_{l_i} \dot{\boldsymbol{p}}_{C_i}^T \dot{\boldsymbol{p}}_{C_i} + \dot{\boldsymbol{p}}_{C_i}^T \boldsymbol{S}(\boldsymbol{\omega}_i) m_{l_i} \boldsymbol{r}_{C_i,l_i} \\ &+ \frac{1}{2} m_{l_i} \boldsymbol{\omega}_i^T \boldsymbol{S}^T(\boldsymbol{r}_{C_i,l_i}) \boldsymbol{S}(\boldsymbol{r}_{C_i,l_i}) \boldsymbol{\omega}_i + \frac{1}{2} \boldsymbol{\omega}_i^T \boldsymbol{I}_{l_i} \boldsymbol{\omega}_i \end{aligned} \tag{B.10}$$

With the Steiner theorem, the moment of inertia of link i with respect to $\boldsymbol{p}_{C_i}$ is:

$$\bar{\boldsymbol{I}}_{l_i} = \boldsymbol{I}_{l_i} + m_{l_i} \boldsymbol{S}^T(\boldsymbol{r}_{C_i,l_i}) \boldsymbol{S}(\boldsymbol{r}_{C_i,l_i}) \tag{B.11}$$

Using equation (B.10) for $\mathcal{T}_{l_i}$ applies:

$$\mathcal{T}_{l_i} = \frac{1}{2} m_{l_i} \dot{\boldsymbol{p}}_{C_i}^T \dot{\boldsymbol{p}}_{C_i} + \dot{\boldsymbol{p}}_{C_i}^T \boldsymbol{S}(\boldsymbol{\omega}_i) m_{l_i} \boldsymbol{r}_{C_i,l_i} + \frac{1}{2} \boldsymbol{\omega}_i^T \bar{\boldsymbol{I}}_{l_i} \boldsymbol{\omega}_i \tag{B.12}$$

The part of the kinetic energy $\mathcal{T}_{m_{i+1}}$ of the rotor i+1 of the augmented links with $\boldsymbol{p}_{C_i}$ as reference can be formulated with the help of equations (B.4) and (B.9):

$$\begin{aligned}\mathcal{T}_{m_{i+1}} &= \frac{1}{2} m_{m_{i+1}} \dot{\boldsymbol{p}}_{C_i}^T \dot{\boldsymbol{p}}_{C_i} + \dot{\boldsymbol{p}}_{C_i}^T \boldsymbol{S}(\boldsymbol{\omega}_i) m_{m_{i+1}} \boldsymbol{r}_{C_i,m_{i+1}} \\ &+ \frac{1}{2} m_{m_{i+1}} \boldsymbol{\omega}_i^T \boldsymbol{S}^T(\boldsymbol{r}_{C_i,m_{i+1}}) \boldsymbol{S}(\boldsymbol{r}_{C_i,m_{i+1}}) \boldsymbol{\omega}_i \\ &+ \frac{1}{2} \boldsymbol{\omega}_{m_{i+1}}^T \boldsymbol{I}_{m_{i+1}} \boldsymbol{\omega} m_{m_{i+1}} \end{aligned} \tag{B.13}$$

with

$$\boldsymbol{\omega}_{m_{i+1}} = \boldsymbol{\omega}_i + \boldsymbol{z}_{m_{i+1}} k_{r_{i+1}} q_{m_{i+1}} \tag{B.14}$$

and

$$\bar{\boldsymbol{I}}_{m_{i+1}} = \boldsymbol{I}_{m_{i+1}} + m_{m_{i+1}} \boldsymbol{S}^T(\boldsymbol{r}_{C_i,m_{m_{i+1}}}) \boldsymbol{S}(\boldsymbol{r}_{C_i,m_{m_{i+1}}}) \tag{B.15}$$

$\mathcal{T}_{m_{i+1}}$ can be redefined as:

$$\begin{aligned}\mathcal{T}_{m_{i+1}} &= \frac{1}{2} m_{m_{i+1}} \dot{\boldsymbol{p}}_{C_i}^T \dot{\boldsymbol{p}}_{C_i} + \dot{\boldsymbol{p}}_{C_i}^T \boldsymbol{S}(\boldsymbol{\omega}_i) m_{m_{i+1}} \boldsymbol{r}_{C_i,m_{i+1}} + \frac{1}{2} \boldsymbol{\omega}_i^T \bar{\boldsymbol{I}}_{m_{i+1}} \boldsymbol{\omega}_i \\ &+ \frac{1}{2} \boldsymbol{z}_{m_{i+1}} k_{r_{i+1}} \dot{q}_{i+1} \boldsymbol{I}_{m_{i+1}} \boldsymbol{\omega}_i + \frac{1}{2} \boldsymbol{\omega}_i^T \boldsymbol{I}_{m_{i+1}} \boldsymbol{z}_{m_{i+1}} k_{r_{i+1}} \dot{q}_{i+1} \end{aligned} \tag{B.16}$$

$$+\frac{1}{2}k_{r_{i+1}}^2\dot{q}_{i+1}^2\boldsymbol{z}_{m_{i+1}}^T\boldsymbol{I}_{m_{i+1}}\boldsymbol{z}_{m_{i+1}}$$

To obtain an expression for the kinetic energy $\mathcal{T}_i$ of the augmented link, $\mathcal{T}_{l_i}$ of link i and $\mathcal{T}_{m_{i+1}}$ of rotor i+1 are added from the equations (B.12) and (B):

$$\begin{aligned}\mathcal{T}_i &= \frac{1}{2}m_i\dot{\boldsymbol{p}}_{C_i}^T\dot{\boldsymbol{p}}_{C_i} + \frac{1}{2}\boldsymbol{\omega}_i^T\bar{\boldsymbol{I}}_i\boldsymbol{\omega}_i \\ &+\frac{1}{2}\boldsymbol{z}_{m_{i+1}}k_{r_{i+1}}\dot{q}_{i+1}\boldsymbol{I}_{m_{i+1}}\boldsymbol{\omega}_i + \frac{1}{2}\boldsymbol{\omega}_i^T\boldsymbol{I}_{m_{i+1}}\boldsymbol{z}_{m_{i+1}}k_{r_{i+1}}\dot{q}_{i+1} \\ &+\frac{1}{2}k_{r_{i+1}}^2\dot{q}_{i+1}^2\boldsymbol{z}_{m_{i+1}}^T\boldsymbol{I}_{m_{i+1}}\boldsymbol{z}_{m_{i+1}}\end{aligned} \tag{B.17}$$

where $\bar{\boldsymbol{I}}_i = \bar{\boldsymbol{I}}_{l_i} + \bar{\boldsymbol{I}}_{m_{i+1}}$ and $m_i = m_{l_i} + m_{m_{i+1}}$ and correspond to the inertia tensor and mass of the augmented link respectively. In addition, the multiplication of the $\boldsymbol{z}_{m_{i+1}}$ with the inertia tensor of the rotors (which is a diagonal matrix) can be expressed as:

$$\boldsymbol{I}_{m_{i+1}}\boldsymbol{z}_{m_{i+1}} = I_{m_{i+1}\,zz}\boldsymbol{z}_{m_{i+1}} \tag{B.18}$$

where the subindex $_{zz}$ indicates the element of the third column and the third row of the inertia tensor. Now the expression for the kinetic energy $\mathcal{T}_i$ of the augmented link is:

$$\begin{aligned}\mathcal{T}_i &= \frac{1}{2}m_i\dot{\boldsymbol{p}}_{C_i}^T\dot{\boldsymbol{p}}_{C_i} + \frac{1}{2}\boldsymbol{\omega}_i^T\bar{\boldsymbol{I}}_i\boldsymbol{\omega}_i \\ &+\frac{1}{2}k_{r_{i+1}}\dot{q}_{i+1}I_{m_{i+1}\,zz}\boldsymbol{z}_{m_{i+1}}^T\boldsymbol{\omega}_i + \frac{1}{2}k_{r_{i+1}}\dot{q}_{i+1}I_{m_{i+1}\,zz}\boldsymbol{\omega}_i^T\boldsymbol{z}_{m_{i+1}} \\ &+\frac{1}{2}k_{r_{i+1}}^2\dot{q}_{i+1}^2I_{m_{i+1}\,zz}\boldsymbol{z}_{m_{i+1}}^T\boldsymbol{z}_{m_{i+1}}\end{aligned} \tag{B.19}$$

If the reference point relative to the center of gravity of the augmented link i $\boldsymbol{p}_{C_i}^i$ is again shifted to $\boldsymbol{r}_{i,C_i}^i$, the linear velocity $\dot{\boldsymbol{p}}_{C_i}^i$ of the center of gravity in the body-fixed coordinate system i is:

$$\dot{\boldsymbol{p}}_{C_i}^i = \dot{\boldsymbol{p}}_i^i + \boldsymbol{\omega}_i^i \times \boldsymbol{r}_{i,C_i}^i \tag{B.20}$$

where $\boldsymbol{r}_{i,C_i}^i = \boldsymbol{p}_{C_i}^i - \boldsymbol{p}_i^i$.

The linear velocity $\dot{\boldsymbol{p}}_{C_i}$ of the center of gravity of the augmented link and its angular velocity $\boldsymbol{\omega}_i$ can now be calculated with the help of the Jacobian matrix $\boldsymbol{J}^{C_i}(\boldsymbol{q})$ and the angular velocities $\dot{\boldsymbol{q}}$ in the robot axes:

$$\begin{bmatrix}\dot{\boldsymbol{p}}_{C_i}\\ \boldsymbol{\omega}_i\end{bmatrix} = \boldsymbol{J}^{(C_i)}(\boldsymbol{q})\dot{\boldsymbol{q}} = \begin{bmatrix}\boldsymbol{J}_P^{(C_i)}\\ \boldsymbol{J}_O^{(C_i)}\end{bmatrix}\dot{\boldsymbol{q}} \tag{B.21}$$

The Jacobian matrices of the augmented links i have the following structure:

$$\boldsymbol{J}_P^{(C_i)} = \begin{bmatrix}\boldsymbol{\jmath}_{P1}^{(C_i)} & \cdots & \boldsymbol{\jmath}_{Pi}^{(C_i)} & \boldsymbol{0} & \cdots & \boldsymbol{0}\end{bmatrix} \tag{B.22}$$

$$\boldsymbol{J}_O^{(C_i)} = \begin{bmatrix}\boldsymbol{\jmath}_{O1}^{(C_i)} & \cdots & \boldsymbol{\jmath}_{Oi}^{(C_i)} & \boldsymbol{0} & \cdots & \boldsymbol{0}\end{bmatrix} \tag{B.23}$$

with the columns:

$$\begin{bmatrix} \boldsymbol{\jmath}_{Pj}^{(C_i)} \\ \boldsymbol{\jmath}_{Oj}^{(C_i)} \end{bmatrix} = \begin{bmatrix} \boldsymbol{z}_j \times (\boldsymbol{p}_{C_i} - \boldsymbol{o}_j) \\ \boldsymbol{z}_j \end{bmatrix} \tag{B.24}$$

With the above considerations and equation (B) can be applied for the kinetic energy of the augmented link i:

$$\begin{aligned} \mathcal{T}_i = & \frac{1}{2} m_i \dot{\boldsymbol{q}}^T \boldsymbol{J}_P^{(C_i)^T} \boldsymbol{J}_P^{(C_i)} \dot{\boldsymbol{q}} + \frac{1}{2} \dot{\boldsymbol{q}}^T \boldsymbol{J}_O^{(C_i)^T} \boldsymbol{R}_i \bar{\boldsymbol{I}}_i^i \boldsymbol{R}_i^T \boldsymbol{J}_O^{(C_i)} \dot{\boldsymbol{q}} \\ & + \frac{1}{2} k_{r_{i+1}} \dot{q}_{i+1} I_{m_{i+1}\,zz} \boldsymbol{z}_{m_{i+1}}^T \boldsymbol{J}_O^{(C_i)} \dot{\boldsymbol{q}} + \frac{1}{2} k_{r_{i+1}} \dot{q}_{i+1} I_{m_{i+1}\,zz} \dot{\boldsymbol{q}}^T \boldsymbol{J}_O^{(C_i)^T} \boldsymbol{z}_{m_{i+1}} \\ & + \frac{1}{2} k_{r_{i+1}}^2 \dot{q}_{i+1}^2 I_{m_{i+1}\,zz} \end{aligned} \tag{B.25}$$

In addition, this last equation can be reformulated using $\dot{q}_{i+1} = [0 \ \cdots \ 1 \ \cdots \ 0]^T \dot{\boldsymbol{q}} = \boldsymbol{e}_{i+1}^T \dot{\boldsymbol{q}}$:

$$\begin{aligned} \mathcal{T}_i = & \frac{1}{2} m_i \dot{\boldsymbol{q}}^T \boldsymbol{J}_P^{(C_i)^T} \boldsymbol{J}_P^{(C_i)} \dot{\boldsymbol{q}} + \frac{1}{2} \dot{\boldsymbol{q}}^T \boldsymbol{J}_O^{(C_i)^T} \boldsymbol{R}_i \bar{\boldsymbol{I}}_i^i \boldsymbol{R}_i^T \boldsymbol{J}_O^{(C_i)} \dot{\boldsymbol{q}} \\ & + \frac{1}{2} k_{r_{i+1}} I_{m_{i+1}\,zz} \dot{\boldsymbol{q}}^T \boldsymbol{e}_{i+1} \boldsymbol{z}_{m_{i+1}}^T \boldsymbol{J}_O^{(C_i)} \dot{\boldsymbol{q}} \\ & + \frac{1}{2} k_{r_{i+1}} I_{m_{i+1}\,zz} \dot{\boldsymbol{q}}^T \boldsymbol{J}_O^{(C_i)^T} \boldsymbol{z}_{m_{i+1}} \boldsymbol{e}_{i+1}^T \dot{\boldsymbol{q}} \\ & + \frac{1}{2} k_{r_{i+1}}^2 I_{m_{i+1}\,zz} \dot{\boldsymbol{q}}^T \boldsymbol{e}_{i+1} \boldsymbol{e}_{i+1}^T \dot{\boldsymbol{q}} \end{aligned} \tag{B.26}$$

This makes possible to express the kinetic energy of the robotic arm in the form $\mathcal{T} = \frac{1}{2} \dot{\boldsymbol{q}}^T \boldsymbol{B}(\boldsymbol{q}) \dot{\boldsymbol{q}}$, where $\boldsymbol{B}(\boldsymbol{q})$ is a (6×6) inertia matrix which is symmetric, configuration dependent and positive definite. It is calculated as:

$$\begin{aligned} \boldsymbol{B}(\boldsymbol{q}) = & \sum_{i=0}^{6} (m_i \boldsymbol{J}_P^{(C_i)^T} \boldsymbol{J}_P^{(C_i)} + \boldsymbol{J}_O^{(C_i)^T} \boldsymbol{R}_i \bar{\boldsymbol{I}}_i^i \boldsymbol{R}_i^T \boldsymbol{J}_O^{(C_i)} \\ & + k_{r_{i+1}} I_{m_{i+1}\,zz} \boldsymbol{e}_{i+1} \boldsymbol{z}_{m_{i+1}}^T \boldsymbol{J}_O^{(C_i)} + k_{r_{i+1}} I_{m_{i+1}\,zz} \boldsymbol{J}_O^{(C_i)^T} \boldsymbol{z}_{m_{i+1}} \boldsymbol{e}_{i+1}^T \\ & k_{r_{i+1}}^2 I_{m_{i+1}\,zz} \boldsymbol{e}_{i+1} \boldsymbol{e}_{i+1}^T) \end{aligned} \tag{B.27}$$

The potential energy is determined with the position vector of center of gravity:

$$\mathcal{U} = -\sum_{i=i}^{n} m_{l_i} \boldsymbol{g}_0^T \boldsymbol{p}_{C_i} \tag{B.28}$$

Thus for the vector $\boldsymbol{g}(\boldsymbol{q})$ of the dynamic model applies:

$$\boldsymbol{g}_i(\boldsymbol{q}) = -\sum_{i=i}^{6} m_{l_i} \boldsymbol{g}_0^T \boldsymbol{\jmath}_{Pi}^{(C_i)}(\boldsymbol{q}) \tag{B.29}$$

The industrial robot Stäubli RX 90-B has the special feature that the motors 1 and 2 are mounted on the first link, the motors 3 and 4 on the third link and the motors 5 and 6 on the fourth link. In addition, axes 5 and 6 are through a common gearbox coupled. Based on this, the presented formulas can not be directly applied on the Stäubli robot RX

90-B. Therefore, the following kinetic energy formulas are separately described for each augmented link of the robot:

- Link 1

$$
\begin{aligned}
&m_1 = m_{l_1} + m_{m_1} + m_{m_2} \\
&\bar{\boldsymbol{I}}_1 = \bar{\boldsymbol{I}}_{l_1} + \bar{\boldsymbol{I}}_{m_1} + \bar{\boldsymbol{I}}_{m_2} \\
&\boldsymbol{\omega}_{m_1} = \boldsymbol{\omega}_1 - k_{r_1}\dot{q}_1\boldsymbol{z}_1 \\
&\boldsymbol{\omega}_{m_2} = \boldsymbol{\omega}_1 - k_{r_2}\dot{q}_2\boldsymbol{z}_2 \\
&\mathcal{T}_1 = \frac{1}{2}m_1\dot{\boldsymbol{q}}^T{\boldsymbol{J}_P^{(C_1)}}^T\boldsymbol{J}_P^{(C_1)}\dot{\boldsymbol{q}} + \frac{1}{2}\dot{\boldsymbol{q}}^T{\boldsymbol{J}_O^{(C_1)}}^T\boldsymbol{R}_1\bar{\boldsymbol{I}}_1^1\boldsymbol{R}_1^T\boldsymbol{J}_O^{(C_1)}\dot{\boldsymbol{q}} \\
&-\frac{1}{2}k_{r_1}I_{{m_1}_{zz}}\dot{\boldsymbol{q}}^T\boldsymbol{e}_1\boldsymbol{z}_1^T\boldsymbol{J}_O^{(C_1)}\dot{\boldsymbol{q}} - \frac{1}{2}k_{r_1}I_{{m_1}_{zz}}\dot{\boldsymbol{q}}^T{\boldsymbol{J}_O^{(C_1)}}^T\boldsymbol{z}_1\boldsymbol{e}_1^T\dot{\boldsymbol{q}} \\
&+\frac{1}{2}k_{r_1}^2I_{{m_1}_{zz}}\dot{\boldsymbol{q}}^T\boldsymbol{e}_1\boldsymbol{e}_1^T\dot{\boldsymbol{q}} \\
&+\frac{1}{2}k_{r_2}I_{{m_2}_{zz}}\dot{\boldsymbol{q}}^T\boldsymbol{e}_2\boldsymbol{z}_2^T\boldsymbol{J}_O^{(C_1)}\dot{\boldsymbol{q}} + \frac{1}{2}k_{r_2}I_{{m_2}_{zz}}\dot{\boldsymbol{q}}^T{\boldsymbol{J}_O^{(C_1)}}^T\boldsymbol{z}_2\boldsymbol{e}_2^T\dot{\boldsymbol{q}} \\
&+\frac{1}{2}k_{r_2}^2I_{{m_2}_{zz}}\dot{\boldsymbol{q}}^T\boldsymbol{e}_2\boldsymbol{e}_2^T\dot{\boldsymbol{q}}
\end{aligned}
\tag{B.30}
$$

- Link 2

$$
\begin{aligned}
&m_2 = m_{l_2} \\
&\bar{\boldsymbol{I}}_2 = \bar{\boldsymbol{I}}_{l_2} \\
&\mathcal{T}_2 = \frac{1}{2}m_2\dot{\boldsymbol{q}}^T{\boldsymbol{J}_P^{(C_2)}}^T\boldsymbol{J}_P^{(C_2)}\dot{\boldsymbol{q}} + \frac{1}{2}\dot{\boldsymbol{q}}^T{\boldsymbol{J}_O^{(C_2)}}^T\boldsymbol{R}_2\bar{\boldsymbol{I}}_2^2\boldsymbol{R}_2^T\boldsymbol{J}_O^{(C_2)}\dot{\boldsymbol{q}}
\end{aligned}
\tag{B.31}
$$

- Link 3

$$
\begin{aligned}
&m_3 = m_{l_3} + m_{m_3} + m_{m_3} \\
&\bar{\boldsymbol{I}}_3 = \bar{\boldsymbol{I}}_{l_3} + \bar{\boldsymbol{I}}_{m_3} + \bar{\boldsymbol{I}}_{m_3} \\
&\boldsymbol{\omega}_{m_3} = \boldsymbol{\omega}_3 - k_{r_3}\dot{q}_3\boldsymbol{z}_3 \\
&\boldsymbol{\omega}_{m_4} = \boldsymbol{\omega}_4 - k_{r_4}\dot{q}_4\boldsymbol{z}_4 \\
&\mathcal{T}_3 = \frac{1}{2}m_3\dot{\boldsymbol{q}}^T{\boldsymbol{J}_P^{(C_3)}}^T\boldsymbol{J}_P^{(C_3)}\dot{\boldsymbol{q}} + \frac{1}{2}\dot{\boldsymbol{q}}^T{\boldsymbol{J}_O^{(C_3)}}^T\boldsymbol{R}_3\bar{\boldsymbol{I}}_3^3\boldsymbol{R}_3^T\boldsymbol{J}_O^{(C_3)}\dot{\boldsymbol{q}} \\
&-\frac{1}{2}k_{r_3}I_{{m_3}_{zz}}\dot{\boldsymbol{q}}^T\boldsymbol{e}_3\boldsymbol{z}_3^T\boldsymbol{J}_O^{(C_3)}\dot{\boldsymbol{q}} - \frac{1}{2}k_{r_3}I_{{m_3}_{zz}}\dot{\boldsymbol{q}}^T{\boldsymbol{J}_O^{(C_3)}}^T\boldsymbol{z}_3\boldsymbol{e}_3^T\dot{\boldsymbol{q}} \\
&+\frac{1}{2}k_{r_3}^2I_{{m_3}_{zz}}\dot{\boldsymbol{q}}^T\boldsymbol{e}_3\boldsymbol{e}_3^T\dot{\boldsymbol{q}} \\
&+\frac{1}{2}k_{r_4}I_{{m_4}_{zz}}\dot{\boldsymbol{q}}^T\boldsymbol{e}_4\boldsymbol{z}_4^T\boldsymbol{J}_O^{(C_3)}\dot{\boldsymbol{q}} + \frac{1}{2}k_{r_4}I_{{m_4}_{zz}}\dot{\boldsymbol{q}}^T{\boldsymbol{J}_O^{(C_3)}}^T\boldsymbol{z}_4\boldsymbol{e}_4^T\dot{\boldsymbol{q}} \\
&+\frac{1}{2}k_{r_4}^2I_{{m_4}_{zz}}\dot{\boldsymbol{q}}^T\boldsymbol{e}_4\boldsymbol{e}_4^T\dot{\boldsymbol{q}}
\end{aligned}
\tag{B.32}
$$

- Link 4

$$
\begin{aligned}
&m_4 = m_{l_4} + m_{m_5} + m_{m_6} \\
&\bar{\boldsymbol{I}}_4 = \bar{\boldsymbol{I}}_{l_4} + \bar{\boldsymbol{I}}_{m_5} + \bar{\boldsymbol{I}}_{m_6}
\end{aligned}
$$

$$
\begin{aligned}
&\boldsymbol{\omega}_{m_5} = \boldsymbol{\omega}_4 - k_{r_5}\dot{q}_5\boldsymbol{z}_4 \\
&\boldsymbol{\omega}_{m_6} = \boldsymbol{\omega}_4 - k_{r_6}(\dot{q}_5 + \dot{q}_6)\boldsymbol{z}_4 \\
&\mathcal{T}_4 = \frac{1}{2}m_4\dot{\boldsymbol{q}}^T\boldsymbol{J}_P^{(C_4)^T}\boldsymbol{J}_P^{(C_4)}\dot{\boldsymbol{q}} + \frac{1}{2}\dot{\boldsymbol{q}}^T\boldsymbol{J}_O^{(C_4)^T}\boldsymbol{R}_4\bar{\boldsymbol{I}}_4^4\boldsymbol{R}_4^T\boldsymbol{J}_O^{(C_4)}\dot{\boldsymbol{q}} \\
&-\frac{1}{2}k_{r_5}I_{m_5\,zz}\dot{\boldsymbol{q}}^T\boldsymbol{e}_5\boldsymbol{z}_4^T\boldsymbol{J}_O^{(C_4)}\dot{\boldsymbol{q}} - \frac{1}{2}k_{r_5}I_{m_5\,zz}\dot{\boldsymbol{q}}^T\boldsymbol{J}_O^{(C_4)^T}\boldsymbol{z}_4\boldsymbol{e}_5^T\dot{\boldsymbol{q}} \\
&+\frac{1}{2}k_{r_5}^2I_{m_5\,zz}\dot{\boldsymbol{q}}^T\boldsymbol{e}_5\boldsymbol{e}_5^T\dot{\boldsymbol{q}} \\
&-\frac{1}{2}k_{r_6}I_{m_6\,zz}\dot{\boldsymbol{q}}^T\boldsymbol{e}_5\boldsymbol{z}_4^T\boldsymbol{J}_O^{(C_4)}\dot{\boldsymbol{q}} - \frac{1}{2}k_{r_6}I_{m_6\,zz}\dot{\boldsymbol{q}}^T\boldsymbol{J}_O^{(C_4)^T}\boldsymbol{z}_4\boldsymbol{e}_5^T\dot{\boldsymbol{q}} \\
&+\frac{1}{2}k_{r_6}^2I_{m_6\,zz}\dot{\boldsymbol{q}}^T\boldsymbol{e}_5\boldsymbol{e}_5^T\dot{\boldsymbol{q}} \\
&-\frac{1}{2}k_{r_6}I_{m_6\,zz}\dot{\boldsymbol{q}}^T\boldsymbol{e}_6\boldsymbol{z}_4^T\boldsymbol{J}_O^{(C_4)}\dot{\boldsymbol{q}} - \frac{1}{2}k_{r_6}I_{m_6\,zz}\dot{\boldsymbol{q}}^T\boldsymbol{J}_O^{(C_4)^T}\boldsymbol{z}_4\boldsymbol{e}_6^T\dot{\boldsymbol{q}} \\
&+\frac{1}{2}k_{r_6}^2I_{m_6\,zz}\dot{\boldsymbol{q}}^T\boldsymbol{e}_6\boldsymbol{e}_6^T\dot{\boldsymbol{q}} \\
&+\frac{1}{2}k_{r_6}^2I_{m_6\,zz}\dot{\boldsymbol{q}}^T\boldsymbol{e}_5\boldsymbol{e}_6^T\dot{\boldsymbol{q}} + \frac{1}{2}k_{r_6}^2I_{m_6\,zz}\dot{\boldsymbol{q}}^T\boldsymbol{e}_6\boldsymbol{e}_5^T\dot{\boldsymbol{q}}
\end{aligned}
\tag{B.33}
$$

- Link 5

$$
\begin{aligned}
&m_5 = m_{l_5} \\
&\bar{\boldsymbol{I}}_5 = \bar{\boldsymbol{I}}_{l_5} \\
&\mathcal{T}_5 = \frac{1}{2}m_5\dot{\boldsymbol{q}}^T\boldsymbol{J}_P^{(C_5)^T}\boldsymbol{J}_P^{(C_5)}\dot{\boldsymbol{q}} + \frac{1}{2}\dot{\boldsymbol{q}}^T\boldsymbol{J}_O^{(C_5)^T}\boldsymbol{R}_5\bar{\boldsymbol{I}}_5^5\boldsymbol{R}_5^T\boldsymbol{J}_O^{(C_4)}\dot{\boldsymbol{q}}
\end{aligned}
\tag{B.34}
$$

- Link 6

$$
\begin{aligned}
&m_6 = m_{l_6} \\
&\bar{\boldsymbol{I}}_6 = \bar{\boldsymbol{I}}_{l_6} \\
&\mathcal{T}_6 = \frac{1}{2}m_6\dot{\boldsymbol{q}}^T\boldsymbol{J}_P^{(C_6)^T}\boldsymbol{J}_P^{(C_6)}\dot{\boldsymbol{q}} + \frac{1}{2}\dot{\boldsymbol{q}}^T\boldsymbol{J}_O^{(C_6)^T}\boldsymbol{R}_6\bar{\boldsymbol{I}}_6^6\boldsymbol{R}_6^T\boldsymbol{J}_O^{(C_6)}\dot{\boldsymbol{q}}
\end{aligned}
\tag{B.35}
$$

With the help of these last 6 equation ((B.30)-(B.35)) the $\boldsymbol{B}(\boldsymbol{q})$ matrix can be obtained factoring $\dot{\boldsymbol{q}}^T$ and $\dot{\boldsymbol{q}}$ and adding all the $\boldsymbol{B}_i(\boldsymbol{q})$ parts of every augmented link:

$$
\boldsymbol{B}(\boldsymbol{q}) = \sum_{i=1}^{6}\boldsymbol{B}_i(\boldsymbol{q}) \tag{B.36}
$$

The equation of motion can be then rewritten in the compact form:

$$
\boldsymbol{B}(\boldsymbol{q})\ddot{\boldsymbol{q}} + \boldsymbol{C}(\boldsymbol{q},\dot{\boldsymbol{q}})\dot{\boldsymbol{q}} + \boldsymbol{F}_v\dot{\boldsymbol{q}} + \boldsymbol{F}_s sgn(\dot{\boldsymbol{q}}) + \boldsymbol{g}(\boldsymbol{q}) = \boldsymbol{\tau} - \boldsymbol{J}^T(\boldsymbol{q})\boldsymbol{h} \tag{B.37}
$$

where the acceleration, quadratic velocity and configuration dependent terms are separated. The viscous and Coulomb friction effects are taken into account by the matrices $\boldsymbol{F}_v$ and $\boldsymbol{F}_s$ respectively. $sgn(\dot{\boldsymbol{q}})$ denotes the $(6times1)$ vector whose components are given by the sign functions of the single joint velocities. $\boldsymbol{g}$ is the vector of gravity, $\boldsymbol{\tau}$ is the vector of the actuation torques. If the end-effector is in contact with the environment, a portion of $\boldsymbol{\tau}$ is used to balance the torques induced by the contact. Such torques are given by $\boldsymbol{J}^T(\boldsymbol{q})\boldsymbol{h}$

where $\boldsymbol{h}$ is the vector of forces and moments exerted by the end-effector. The matrix $\boldsymbol{C}$ is the matrix that contains the Coriolis and centrifugal effects. Several forms of this matrix exist. Using Christoffel symbols, a particular solution that shows special properties, affects the model. The Christoffel symbols are coordinate-space expressions for the Levi-Civita connection (covariant derivative: derivative along vector fields).

Thus the matrix $\boldsymbol{C}$ can be calculated with the following formula:

$$\sum_{j=1}^{6} c_{ij} q_j = \sum_{j=1}^{6} \sum_{k=1}^{6} h_{ijk} \dot{q}_k \dot{q}_j = \sum_{j=1}^{6} \sum_{k=1}^{6} \left(\frac{\partial b_{ij}}{\partial q_k} - \frac{1}{2} \frac{\partial b_{jk}}{\partial q_i} \right) \dot{q}_k \dot{q}_j \tag{B.38}$$

The splitting of the first term in this equation yields:

$$\sum_{j=1}^{6} c_{ij} q_j = \frac{1}{2} \sum_{j=1}^{6} \sum_{k=1}^{6} \frac{\partial b_{ij}}{\partial q_k} \dot{q}_k \dot{q}_j + \frac{1}{2} \sum_{j=1}^{6} \sum_{k=1}^{6} \left(\frac{\partial b_{ik}}{\partial q_j} - \frac{1}{2} \frac{\partial b_{jk}}{\partial q_i} \right) \dot{q}_k \dot{q}_j \tag{B.39}$$

The elements c_{ij} of the matrix $\boldsymbol{C}$ are given by:

$$c_{ij} = \sum_{k=1}^{6} c_{ijk} \dot{q}_k \tag{B.40}$$

with:

$$c_{ijk} = \frac{1}{2} \left(\frac{\partial b_{ij}}{\partial q_k} + \frac{\partial b_{ik}}{\partial q_j} - \frac{\partial b_{jk}}{\partial q_i} \right) \tag{B.41}$$

The coefficients of equation (B.41) are called Christoffel symbols of the first type. Due to the symmetry of the matrix $\boldsymbol{B}$ it can be written:

$$c_{ijk} = c_{ikj} \tag{B.42}$$

It can be shown that with the solution of the matrix $\boldsymbol{C}$ presented above and equations (B.41) and (B.42) the matrix

$$\boldsymbol{N}(\boldsymbol{q},\dot{\boldsymbol{q}}) = \dot{\boldsymbol{B}}(\boldsymbol{q}) - 2\boldsymbol{C}(\boldsymbol{q},\dot{\boldsymbol{q}}) \tag{B.43}$$

skew-symmetric is [134]. Thus it applies for an arbitrary vector $\boldsymbol{w}$ of dimension (n×1):

$$\boldsymbol{w}^T \boldsymbol{N}(\boldsymbol{q},\dot{\boldsymbol{q}}) \boldsymbol{w} = \boldsymbol{0} \tag{B.44}$$

This is an important property of the equation of motion and can be used for the design of various control strategies.

C Quaternions

There are several ways to represent the orientation of a rigid body with respect to a reference frame.Instead of rotating an object through a series of successive rotations like the Euler angles does, a quaternion rotates the object through a single arbitrary rotation axis. The representation of the quaternion consists of a combination of three parameters (also called vector part: ϵ_x, ϵ_y and ϵ_z) and a real number (also called scalar part: η):

$$\boldsymbol{\phi} = \begin{bmatrix} \eta \\ \boldsymbol{\epsilon} \end{bmatrix} = \begin{bmatrix} \eta \\ \epsilon_x \\ \epsilon_y \\ \epsilon_z \end{bmatrix} \tag{C.1}$$

There is not a direct way to calculate the quaternion given the vector $\boldsymbol{q}$. Therefore the direct kinematics should be first computed. The homogeneous matrix $\boldsymbol{A}$ results from the DK. Given its rotation matrix (3×3) $\boldsymbol{R}$ the quaternion can be calculated with the following algorithm [36]:

```
function Quat = HM2Quaternion(R)
    Tr = trace(R);
    q0 = 0;qx = 0;qy=0;qz=0;

    if (Tr ≥ 0.0)
            r = sqrt(1.0 + Tr);
            s = 0.5 / r;
            q0 = 0.5 * r;
            qx = (R(3,2) - R(2,3)) * s;
            qy = (R(1,3) - R(3,1)) * s;
            qz = (R(2,1) - R(1,2)) * s;
    else
        maxCase = 0; % i,j,k = x,y,z

        if (R(2,2) > R(1,1))
            maxCase = 1; % i,j,k = y,z,x
        end
        if ((maxCase == 0 && R(3,3) > R(1,1)) || (maxCase == 1 ...
            && R(3,3) > R(2,2)))
            maxCase = 2;% i,j,k = z,x,y
        end
        if maxCase == 0
            r = sqrt(R(1,1) - R(2,2) - R(3,3) + 1.0);
            s = 0.5 / r;
            qx = 0.5 * r;
            qy = (R(1,2) + R(2,1)) * s;
            qz = (R(3,1) + R(1,3)) * s;
            q0 = (R(3,2) - R(2,3)) * s;
        elseif maxCase == 1
```

```
29              r = sqrt(R(2,2) - R(3,3) - R(1,1) + 1.0);
30              s = 0.5 / r;
31              qy = 0.5 * r;
32              qz = (R(2,3) + R(3,2)) * s;
33              qx = (R(1,2) + R(2,1)) * s;
34              q0 = (R(1,3) - R(3,1)) * s;
35          elseif maxCase == 2
36              r = sqrt(R(3,3) - R(1,1) - R(2,2) + 1.0);
37              s = 0.5 / r;
38              qz = 0.5 * r;
39              qx = (R(3,1) + R(1,3)) * s;
40              qy = (R(2,3) + R(3,2)) * s;
41              q0 = (R(2,1) - R(1,2)) * s;
42          end
43      end
44      Quat = [q0,qx,qy,qz];
```

It is desired to calculate the error using quaternion theory [41,107,137,168]. The quaternion $\boldsymbol{\phi}$ can be interpreted as a complex number with η being the real part and $\boldsymbol{\epsilon}$ the complex part. Hence, the complex conjugate of $\boldsymbol{\phi}$ is defined as:

$$\bar{\boldsymbol{\phi}} = \begin{bmatrix} \eta \\ -\boldsymbol{\epsilon} \end{bmatrix} \tag{C.2}$$

Therefore, the inverse rotation matrix can be expressed as:

$$\boldsymbol{R}^{-1}(\boldsymbol{\phi}) = \boldsymbol{R}^{T}(\boldsymbol{\phi}) = \boldsymbol{R}(\bar{\boldsymbol{\phi}}) \tag{C.3}$$

Since successive rotations involves multiplication between two rotation matrices and quaternion multiplication is equivalent to orthogonal matrix multiplication, it can be stated that:

$$\boldsymbol{R}(\boldsymbol{\phi}_1)\boldsymbol{R}(\boldsymbol{\phi}_2) = \boldsymbol{R}(\boldsymbol{\phi}_1\boldsymbol{\phi}_2) \tag{C.4}$$

where the quaternion multiplication is defined as:

$$\boldsymbol{\phi}_1\boldsymbol{\phi}_2 = \begin{bmatrix} \eta_1 & -\boldsymbol{\epsilon}_1^T \\ \boldsymbol{\epsilon}_1 & \eta_1\boldsymbol{I} + \boldsymbol{S}(\boldsymbol{\epsilon}_1) \end{bmatrix} \begin{bmatrix} \eta_2 \\ \boldsymbol{\epsilon}_2 \end{bmatrix} \tag{C.5}$$

where $\boldsymbol{I}$ is the (3×3) identity matrix and the operator $\boldsymbol{S}(\cdot)$ is described in equation (5.20). Now, the control objective is to make the error equal zero, i.e. $\boldsymbol{R}_r = \boldsymbol{R}_a$. Thus, the error in terms of rotation matrices is defined as:

$$\boldsymbol{R}_e = \boldsymbol{R}_r^{-1}\boldsymbol{R}_a = \boldsymbol{R}_r^{T}\boldsymbol{R}_a \tag{C.6}$$

From equation (C.3) and (C.5) and applying the quaternion representation, the error lies as $\boldsymbol{R}_e = \boldsymbol{R}(\boldsymbol{\phi}_e)$ where:

$$\boldsymbol{\phi}_e = \bar{\boldsymbol{\phi}}_r\boldsymbol{\phi}_a = \begin{bmatrix} \eta_r & -\boldsymbol{\epsilon}_r^T \\ \boldsymbol{\epsilon}_r & \eta_r\boldsymbol{I} + \boldsymbol{S}(\boldsymbol{\epsilon}_r) \end{bmatrix} \begin{bmatrix} \eta_a \\ \boldsymbol{\epsilon}_a \end{bmatrix} \tag{C.7}$$

An error equal to zero is expressed in quaternion notation as follows:

$$\boldsymbol{\phi}_e = \begin{bmatrix} \eta_e \\ \boldsymbol{\epsilon}_e \end{bmatrix} = \begin{bmatrix} \pm 1 \\ \mathbf{0} \end{bmatrix} \tag{C.8}$$

The orientation error can be then expressed as a 3-terms vector taken from $\boldsymbol{\epsilon}_e$. The sign of the error is obtained by the scalar product of $\boldsymbol{\phi}_r$ and $\boldsymbol{\phi}_a$.

D Simulink Models

The control architectures used in this project are described in chapter Chapter 5. However, a realistic implementation is not obvious. Therefore a clear development in Simulink of the control actions is here presented. All signals and their dimensions are denoted with numbers,in case of column vectors, and with numbers between brackets, in case of matrices.

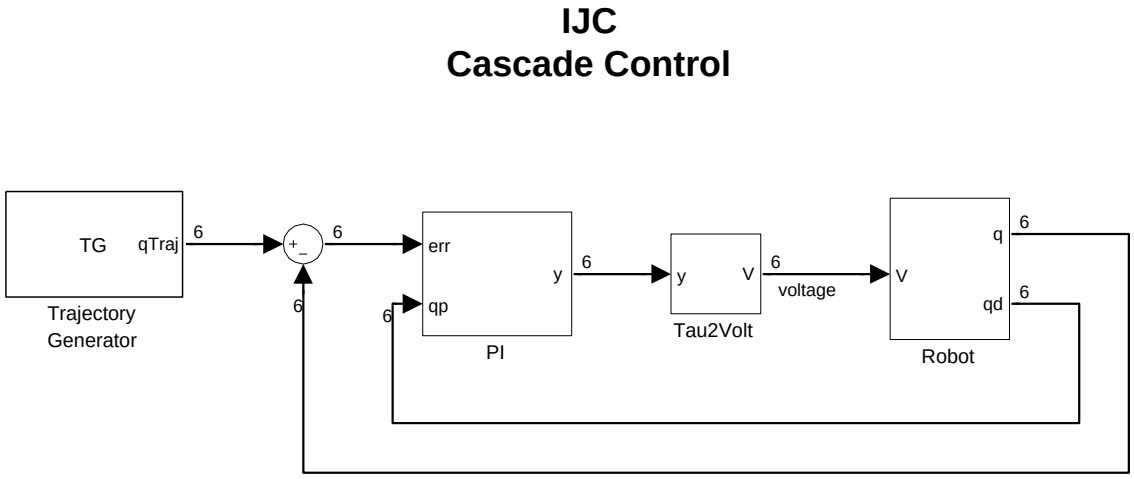

Figure D.1: Independent Joint Control architecture. The block *Trajectory Generator* computes a vector (6×1) in real time for each reference value of every link of the robot ($\boldsymbol{q}_r$). This value is compared with the actual value ($\boldsymbol{q}_a$). The error is propagated to the PI Cascade controller, where the actual values of the velocity ($\dot{\boldsymbol{q}}_a$)are considered to calculate an output. This output is converted to voltage values, which are given to each link of the robot (motors).

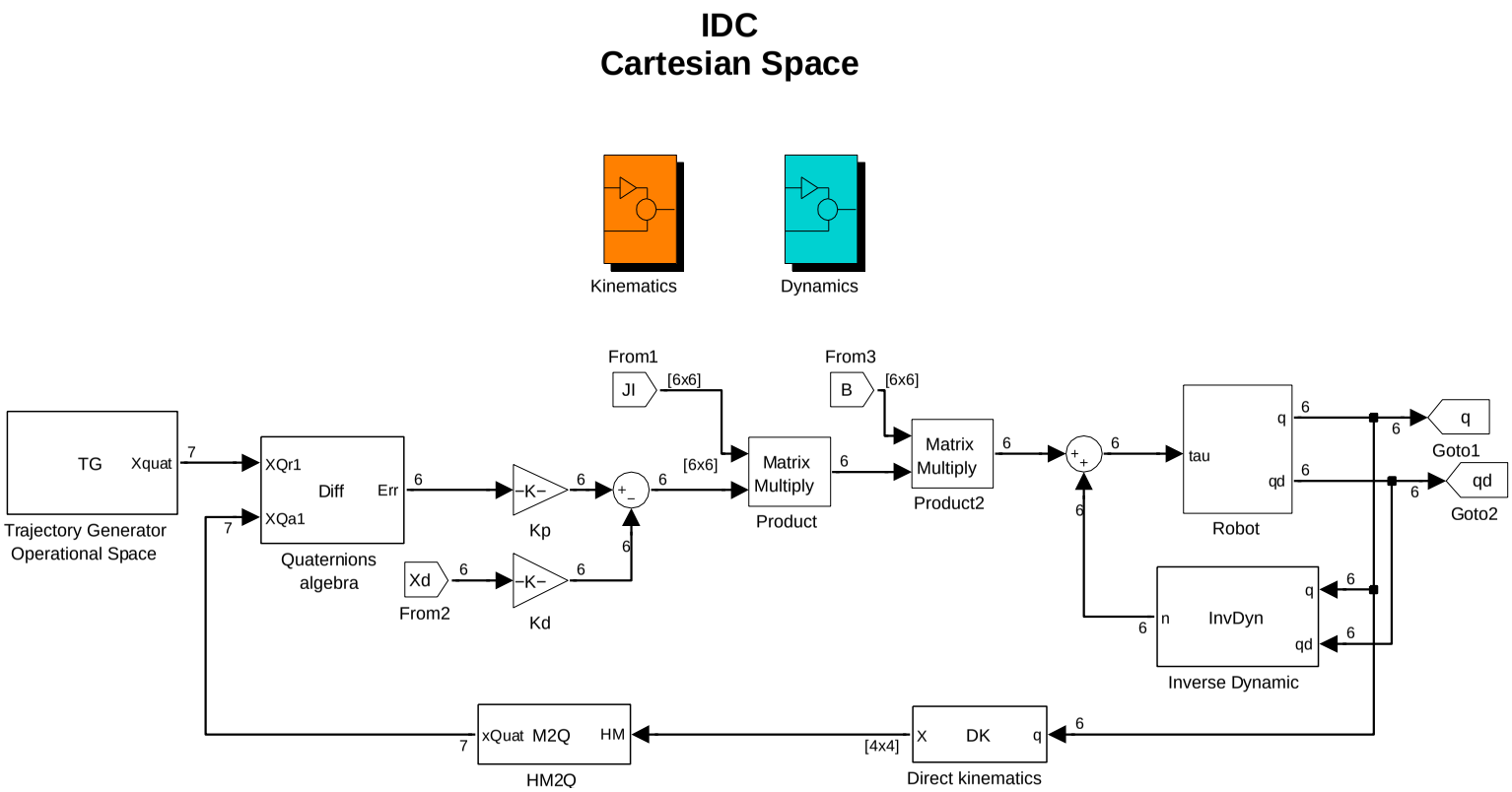

Figure D.2: Inverse Dynamics Cartesian Space Control architecture. The block *Trajectory Generator Operational Space* computes a vector (7×1) $\boldsymbol{X}_{\phi_r}$ in real time, where three values correspond to the position reference in Cartesian space ($\boldsymbol{p}_r$) and the rest four elements correspond to the quaternion ($\boldsymbol{\phi}_r$) for each reference value of every link of the robot ($\boldsymbol{q}_r$). This value is compared with the actual value ($\boldsymbol{X}_{\phi_a}$) generating an error with dimensions (6×1). The error is propagated to the PD controller. Afterwards, the differential inverse kinematics is computed with the inverse of the Jacobian matrix, $\boldsymbol{J}^{-1}$ and multiplied by the inertia matrix $\boldsymbol{B}$. This output, together with the calculation of the rest of the equation of motion, is given to the robot as a voltage values for every link. Two blocks have the task to compute the kinematics and the dynamics of the robot. Here are used the blocks *Go to* and *From* to represent the models in a clear form.

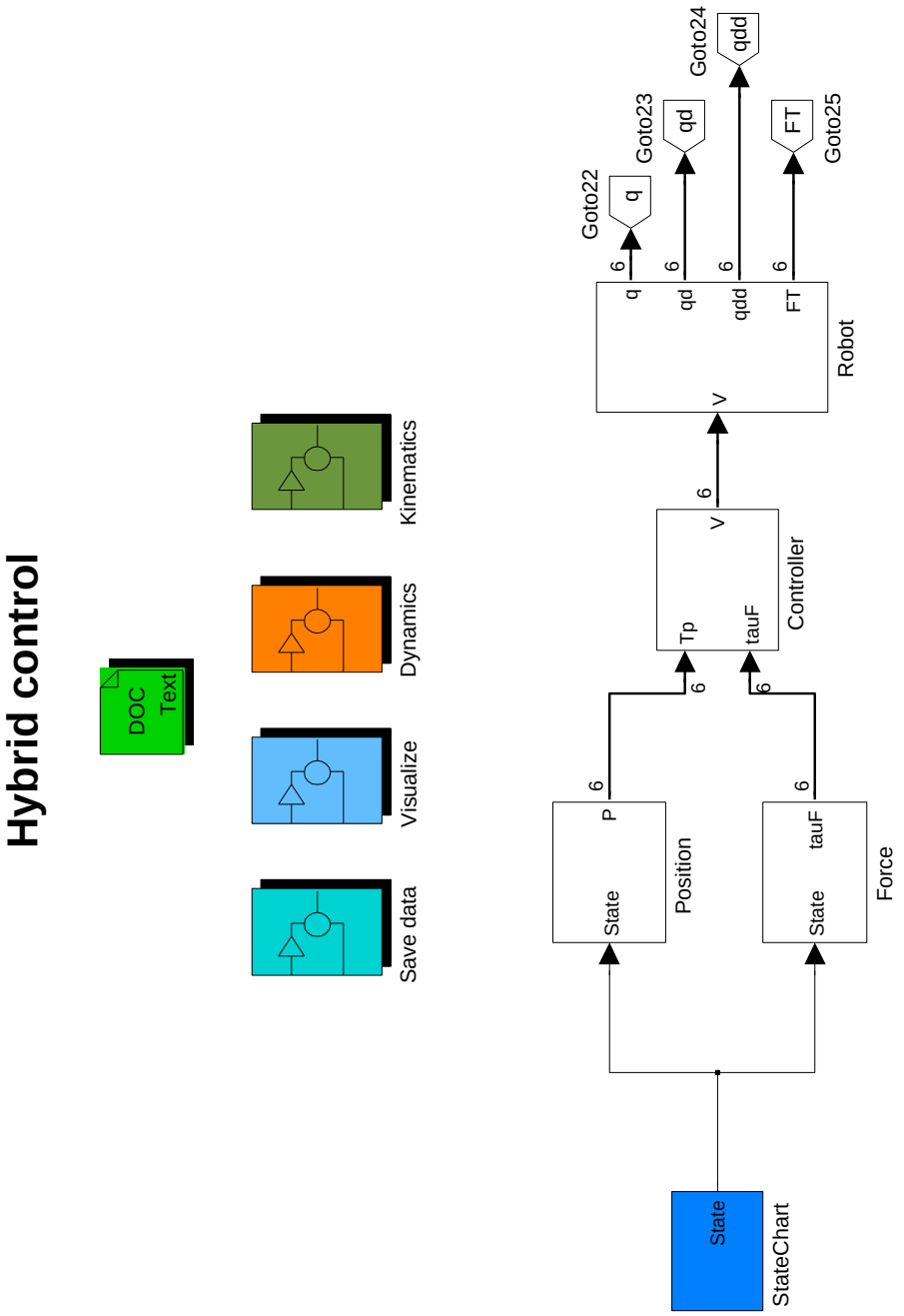

Figure D.3: Hybrid Control architecture. The block *State Chart* choses the task to perform. This command is passed to the different trajectory generators (given in position or in force coordinates) where an error will be calculated. This values are the inputs for the controllers where the inverse kinematics is computed and its output converted to corresponding voltages for every link of the robot. Two blocks have the task to compute the kinematics and the dynamics of the robot. Here are used the blocks *Go to* and *From* to represent the models in a clear form.

Bibliography

[1] Steven D. Abramowitch, Christos D. Papageorgiou, Richard E. Debski, Theodore D. Clineff, and Savio L-Y. Woo. A biomechanical and histological evaluation of the structure and function of the healing medial collateral ligament in a goat model. *Knee Surgery, Sports Traumatology, Arthroscopy*, 11:155–162, 2003. 10.1007/s00167-002-0336-5.

[2] C.H. An, C.G. Atkeson, and J. Hollerbach. *Model-Based Control of a Robot Manipulator*. The MIT Press Series in Artificial Intelligence. MIT Press, 1988.

[3] Chae An and J. Hollerbach. Kinematic stability issues in force control of manipulators. In *Proc. IEEE Int. Conf. Robotics and Automation*, volume 4, pages 897–903, 1987.

[4] R. J. Anderson and M. W. Spong. Hybrid impedance control of robotic manipulators. *IEEE J JRA*, 4(5):549–556, 1988.

[5] M. H. Ang and V. D. Tourassis. General-purpose inverse kinematics transformations for robotic manipulators. *Journal of Robotic Systems*, 4:527–549, 1987.

[6] A. Angermann. *Matlab, Simulink, Stateflow: Grundlagen, Toolboxen, Beispiele.* Oldenbourg, 2005.

[7] B. Armstrong, O. Khatib, and J. Burdick. The explicit dynamic model and inertial parameters of the puma 560 arm. In *Proc. IEEE Int. Conf. Robotics and Automation*, volume 3, pages 510–518, 1986.

[8] P. R. Belanger. Estimation of angular velocity and acceleration from shaft encoder measurements. In *Proc. Conf. IEEE Int Robotics and Automation*, pages 585–592, 1992.

[9] T. Bence. *Biomechanische Untersuchungen zu Veränderungen der Wirbelsäulensegment-Steifigkeit im Bereich des thorakolumbalen Übergangs nach operativen Versorgungen.* PhD thesis, Klinik für Orthopädie und Sportorthopädie am Klinikum rechts der Isar Technische Universität München, 2006.

[10] G. Bergmann, F. Graichen, A. Bender, A. Rohlmann, A. Halder, A. Beier, and P. Westerhoff. In vivo gleno-humeral joint loads during forward flexion and abduction. *Journal of Biomechanics*, 44(8):1543 – 1552, 2011.

[11] V Bühren. Verletzungen der brust- und lendenwirbelsäule. *Der Unfallchirurg*, 72(7), 2003.

[12] M. Blauth, L. Bastian, C. Knop, U. Lange, G. Tusch, and . Classification of thoracic and lumbar injuries: An analysis of interobserver reliability. *Der Orthopäde*, 28:662–681, 1999. 10.1007/PL00003655.

[13] D.V. Boguszewski, J. T. Shearn, C. T. Wagner, and Butler D. L. Effect of anterior translation on anterior knee force in a porcine model. In *Summer Bioengineering Conference*, Marriott Resort, Marco Island, Florida, USA, 2008. ASME.

[14] W. Börm and F. Meyer. *Spinale Neurochirurgie: Operatives Management von Wirbelsäulenerkrankungen*. Schattauer, 2008.

[15] H. Bruyninckx and J. De Schutter. Symbolic differentiation of the velocity mapping for a serial kinematic chain. *Mechanism and Machine Theory*, 31(2):135–148, 1996.

[16] S. Buchmann. *Biomechanische In-vitro-Testung eines Wirbelkörperersatzes am thorakolumbalen Übergang in Verbindung mit verschiedenen Stabilisierungsmethoden am bovinen Tiermodell*. PhD thesis, Klinikum rechts der Isar. Technische Universität München, 2008.

[17] Statistisches Bundesamt. Fallpauschalenbezogene krankenhausstatistik (drg-statistik) operationen und prozeduren der vollstationären patientinnen und patienten in krankenhäusern - ausführliche darstellung, Oktober 2010.

[18] S. R. Buss. Introduction to inverse kinematics with jacobian transpose, pseudoinverse and damped least squares methods. Technical report, Department of Mathematics University of California, San Diego, La Jolla, CA 92093-0112, October 2009.

[19] Samuel R. Buss. Introduction to inverse kinematics with jacobian transpose, pseudoinverse and damped least squares methods. Technical report, IEEE Journal of Robotics and Automation, 2004.

[20] F. Caccavale, S. Chiaverini, and B. Siciliano. Second-order kinematic control of robot manipulators with jacobian damped least-squares inverse: theory and experiments. *IEEE J MECH*, 2(3):188–194, 1997.

[21] F. Caccavale, C. Natale, B. Siciliano, and L. Villani. Six-dof impedance control based on angle/axis representations. *IEEE J RA*, 15(2):289–300, 1999.

[22] Gregory Carlin, Glen Livesay, Christopher Harner, Yasuyuki Ishibashi, Hyoung Kim, and Savio Woo. In-situ forces in the human posterior cruciate ligament in response to posterior tibial loading. *Annals of Biomedical Engineering*, 24:193–197, 1996. 10.1007/BF02667348.

[23] Raúl Armando Castillo Cruces. *Concept and Design of a Cooperative Robotic Assistant Surgery System*. PhD thesis, Universität Siegen, 2008.

[24] Ben S. Cazzolato, John Costi, Boyin Ding, and Richard Stanley. Hexapod robot control system for biomechanics testing, 2010.

[25] Kyong-Sok Chang and O. Khatib. Operational space dynamics: efficient algorithms for modeling and control of branching mechanisms. In *Proc. IEEE Int. Conf. Robotics and Automation ICRA '00*, volume 1, pages 850–856, 2000.

[26] M.W. Chapman. *Chapman's orthopaedic surgery*. Number Bd. 1-4 in Doody's all reviewed collection. Lippincott Williams & Wilkins, 2001.

[27] S. Chiaverini and L. Sciavicco. The parallel approach to force/position control of robotic manipulators. *IEEE J RA*, 9(4):361–373, 1993.

[28] S. Chiaverini, B. Siciliano, and O. Egeland. Review of the damped least-squares inverse kinematics with experiments on an industrial robot manipulator. *IEEE J CST*, 2(2):123–134, 1994.

[29] J.J. Craig. *Introduction to robotics: mechanics and control*. Addison-Wesley series in electrical and computer engineering: control engineering. Pearson/Prentice Hall, 2005.

[30] E. B Dam, M. Koch, and Lillholm M. Quaternions, interpolation and animation. Technical report, Department of Computer Science, University of Copenhagen, Universitetsparken, Universitetsparken 1 DK-2100 Kbh Denmark, July 1998.

[31] Nathan Delson and Harry West. Bracing to increase the natural frequency of a manipulator: Analysis and design. *The International Journal of Robotics Research*, 12(6):560–571, 1993.

[32] Mahendra Dhanu Singh, Kusnadi Liem, Vladimirs Leontjievs, and Andres Kecskemethy. A fluidic-muscle driven force-controlled parallel platform for physical simulation of virtual spatial force-displacement laws. *Meccanica*, 46:171–182(12), February 2011.

[33] A. Disch, K. Schaser, I. Melcher, A. Luzzati, F. Feraboli, and W. Schmoelz. En bloc spondylectomy reconstructions in a biomechanical in-vitro study. *Eur Spine J*, 17:715–725, 2008.

[34] B. W. Drake and T. C. S. Hsia. Implementation of a unified robot kinematics and inverse dynamics algorithm on a dsp chip. *IEEE J IE*, 40(2):273–281, 1993.

[35] S. Dutre, H. Bruyninckx, and J. De Schutter. The analytical jacobian and its derivative for a parallel manipulator. In *Proc. Conf. IEEE Int Robotics and Automation*, volume 4, pages 2961–2966, 1997.

[36] D.H. Eberly and K. Shoemake. *Game physics*. Interactive 3D technology series. Elsevier/Morgan Kaufmann, 2004.

[37] P. Eysel. *Die ventrale Instrumentation der Rumpfwirbelsäule*. Enke, 1998.

[38] YC Fangt, CC Hsieh, MJ Kim, JJ Chang, and TC Woo. Real time motion fairing with unit quaternions. *Computer-Aided Design*, 30(3):191 – 198, 1998. Motion Design and Kinematics.

[39] R. Featherstone. Position and velocity transformations between robot end-effector coordinates and joint angles. *The International Journal of Robotics Research*, 2(2):35–45, 1983.

[40] William D. Fisher and M. Shahid Mujtaba. Hybrid position/force control: a correct formulation. *Int. J. Rob. Res.*, 11:299–311, August 1992.

[41] O.-E. Fjellstad and T. I. Fossen. Quaternion feedback regulation of underwater vehicles. In *Proc. Third IEEE Conf. Control Applications*, pages 857–862, 1994.

[42] G.F. Franklin, J.D. Powell, and M.L. Workman. *Digital control of dynamic systems*. Addison-Wesley world student series. Addison-Wesley, 1998.

[43] Kyle David Fraysur. A passive pure moment protocol for testing spine segments: development and application. Master's thesis, University of Tennessee Health Science Center, 2010.

[44] M. Frey, R. Burgkart, F. Regenfelder, and R. Riener. Optimised robot-based system for the exploration of elastic joint properties. *Medical and Biological Engineering and Computing*, 42:674–678, 2004. 10.1007/BF02347550.

[45] Martin Frey, Robert Riener, Christian Michas, Felix Regenfelder, and Rainer Burgkart. Elastic properties of an intact and acl-ruptured knee joint: measurement, mathematical modelling, and haptic rendering. *Journal of Biomechanics*, 39(8):1371–82, 2006.

[46] H. Fujie, K. Mabuchi, S.L. Woo, G.A. Livesay, S. Arai, and Y. Tsukamoto. The use of robotics technology to study human joint kinematics: a new methodology. *J Biomech Eng*, 115(3):211–7, 1993.

[47] Hiromichi Fujie, Glen A. Livesay, Masahiro Fujita, and Savio L-Y. Woo. Forces and moments in six-dof at the human knee joint: Mathematical description for control. *Journal of Biomechanics*, 29(12):1577 – 1585, 1996.

[48] Hiromichi Fujie, Glen A. Livesay, Savio L-Y. Woo, Shinji Kashiwaguchi, and Gail Blomstrom. The use of a universal force-moment sensor to determine in-situ forces in ligaments: A new methodology. *Journal of Biomechanical Engineering*, 117(1):1–7, 1995.

[49] Hiromichi Fujie, Takeshi Sekito, and Akiyuki Orita. A novel robotic system for joint biomechanical tests: Application to the human knee joint. *Journal of Biomechanical Engineering*, 126(1):54–61, 2004.

[50] Y. Fung. *Biomechanics: mechanical properties of living tissues*. Biomechanics / Y. C. Fung. Springer-Verlag, 1993.

[51] M. Gautier. Numerical calculation of the base inertial parameters of robots. In *Proc. Conf. IEEE Int Robotics and Automation*, pages 1020–1025, 1990.

[52] M. Gautier and W. Khalil. A direct determination of minimum inertial parameters of robots. In *Proc. Conf. IEEE Int Robotics and Automation*, pages 1682–1687, 1988.

[53] M. Gautier and W. Khalil. On the identification of the inertial parameters of robots. In *Proc. 27th IEEE Conf. Decision and Control*, pages 2264–2269, 1988.

[54] M. Gautier and W. Khalil. Identification of the minimum inertial parameters of robots. In *Proc. Conf. IEEE Int Robotics and Automation*, pages 1529–1534, 1989.

[55] M. Gautier and W. Khalil. Direct calculation of minimum set of inertial parameters of serial robots. *IEEE J RA*, 6(3):368–373, 1990.

[56] M. Gautier and W. Khalil. Exciting trajectories for the identification of base inertial parameters of robots. In *Proc. 30th IEEE Conf. Decision and Control*, pages 494–499, 1991.

[57] M. Gautier, W. Khalil, and P. P. Restrepo. Identification of the dynamic parameters of a closed loop robot. In *Proc. Conf. IEEE Int Robotics and Automation*, volume 3, pages 3045–3050, 1995.

[58] M. Gautier, W. Khalil, and P. P. Restrepo. Identification of the dynamic parameters of a closed loop robot. In *Proc. Conf. IEEE Int Robotics and Automation*, volume 3, pages 3045–3050, 1995.

[59] Philippe Gèdet, Paul A. Thistlethwaite, and Stephen J. Ferguson. Minimizing errors during in vitro testing of multisegmental spine specimens: Considerations for component selection and kinematic measurement. *Journal of Biomechanics*, 40(8):1881 – 1885, 2007.

[60] Lars G. Gilbertson, Todd C. Doehring, and James D. Kang. New methods to study lumbar spine biomechanics: Delineation of in vitro load-displacement characteristics by using a robotic/ufs testing system with hybrid control. *Operative Techniques in Orthopaedics*, 10(4):246 – 253, 2000.

[61] Lars G. Gilbertson, Todd C. Doehring, Glen A. Livesay, Theodore W. Rudy, James D. Kang, and Savio L-Y. Woo. Improvement of accuracy in a high-capacity, six degree-of-freedom load cell: Application to robotic testing of musculoskeletal joints. *Annals of Biomedical Engineering*, 27:839–843, 1999. 10.1114/1.236.

[62] Darrell J. Goertzen and Gregory N. Kawchuk. A novel application of velocity-based force control for use in robotic biomechanical testing. *Journal of Biomechanics*, 42(3):366 – 369, 2009.

[63] Darrell J Goertzen, Chris Lane, and Thomas R Oxland. Neutral zone and range of motion in the spine are greater with stepwise loading than with a continuous loading protocol. An in vitro porcine investigation. *Journal of Biomechanics*, 37(2):257 – 261, 2004. Spinal Biomechanics.

[64] Henry Gray. *Anatomy of the human body, by Henry Gray. 20th ed., thoroughly rev. and re-edited by Warren H. Lewis.* Philadelphia: Lea & Febiger, 1918., 1918.

[65] J.G. Heller, T.A. Zdeblick, D.A. Kunz, R. McCabe, and M.E. Cooke. Spinal instrumentation for metastatic disease: in vitro biomechanical analysis. *J Spinal Disord*, 6(1):17–22, 1993.

[66] N. Hogan. Impedance control - An approach to manipulation. I - Theory. II - Implementation. III - Applications. *ASME Transactions Journal of Dynamic Systems and Measurement Control B*, 107:1–24, March 1985.

[67] J. Hoogen. *Regelung eines Industrieroboters zur haptischen Interaktion mit einem virtuellen Kniegelenk*. PhD thesis, Technische Universität München, 2004.

[68] Jens Hoogen, Robert Riener, and Günther Schmidt. Control aspects of a robotic haptic interface for kinesthetic knee joint simulation. *Control Engineering Practice*, 10(11):1301 – 1308, 2002.

[69] Ryan A. Howard, Joshua M. Rosvold, Shon P. Darcy, David T. Corr, Nigel G. Shrive, Janet E. Tapper, Janet L. Ronsky, Jillian E. Beveridge, Linda L. Marchuk, and Cyril B. Frank. Reproduction of in vivo motion using a parallel robot. *Journal of Biomechanical Engineering*, 129(5):743–749, 2007.

[70] Jun Hu, Qianqian Cao, and Fang Liu. A planning algorithm of trajectory and feedrate generation of spatial motion. In *Proc. Int. Conf. Mechatronics and Automation ICMA 2009*, pages 1572–1577, 2009.

[71] R. Hu and P. C. Müller. Independent joint control: Estimation and compensation of coupling and friction effects in robot position control. *Journal of Intelligent & Robotic Systems*, 15:41–51, 1996. 10.1007/BF00435726.

[72] Qingjiu Huanga and R. Enomoto. Hybrid position, posture, force and moment control of robot manipulators. In *Proc. IEEE Int. Conf. Robotics and Biomimetics ROBIO 2008*, pages 1444–1450, 2009.

[73] Yasuyuki Ishibashi, Theodore W. Rudy, Glen A. Livesay, Jeffrey D. Stone, Freddie H. Fu, and Savio L. Y. Woo. The effect of anterior cruciate ligament graft fixation site at the tibia on knee stability: Evaluation using a robotic testing system. *Arthroscopy: The Journal of Arthroscopic & Related Surgery*, 13(2):177 – 182, 1997.

[74] F. Janabi-Sharifi, V. Hayward, and C.-S. J. Chen. Discrete-time adaptive windowing for velocity estimation. *IEEE J CST*, 8(6):1003–1009, 2000.

[75] Robert P. Juad, Cary D. Perttunen, and Cedric W. Mousseau. Simultaneous force, torque, position, and orientation control of a robot manipulator on a constrained surface incorporating force sensor feedback. In *Proc. American Control Conf*, pages 453–458, 1987.

[76] Akihiro Kanamori, Masataka Sakane, Jennifer Zeminski, Theodore W. Rudy, and Savio L-Y. Woo. In-situ force in the medial and lateral structures of intact and acl-deficient knees. *Journal of Orthopaedic Science*, 5:567–571, 2000. 10.1007/s007760070007.

[77] R Kelly. Point-to-point robot control under actuator constraints. *Control Engineering Practice*, 5:1555–1562, 1997.

[78] R. Kelly, V. Santibáñez, and Loría. *Control of Robot Manipulators in Joint Space*. Springer, 2006.

[79] A. Kettler, E. Hartwig, M. Schultheiß, L. Claes, and H.-J. Wilke. Mechanically simulated muscle forces strongly stabilize intact and injured upper cervical spine specimens. *Journal of Biomechanics*, 35(3):339 – 346, 2002.

[80] W. Khalil and É. Dombre. *Modeling, identification & control of robots*. Kogan Page Science Paper Edition. Kogan Page Science, 2004.

[81] W. Khalil, M. Gautier, and P. Lemoine. Identification of the payload inertial parameters of industrial manipulators. In *Proc. IEEE Int Robotics and Automation Conf*, pages 4943–4948, 2007.

[82] W. Khalil, J. Kleinfinger, and M. Gautier. Reducing the computational burden of the dynamic models of robots. In *Proc. IEEE Int. Conf. Robotics and Automation*, volume 3, pages 525–531, 1986.

[83] O. Khatib. A unified approach for motion and force control of robot manipulators: The operational space formulation. *IEEE J JRA*, 3(1):43–53, 1987.

[84] O. Khatib and J. Burdick. Motion and force control of robot manipulators. In *Proc. IEEE Int. Conf. Robotics and Automation*, volume 3, pages 1381–1386, 1986.

[85] S. P. Kühnel. *Untersuchungen an der gesunden, der degenerativ veränderten und der operativ fusionierten Lendenwirbelsäule*. PhD thesis, Ludwig-Maximilians-Universität zu München, 2007.

[86] P. Klein and P. Sommerfeld. *Biomechanik der menschlichen Gelenke: Grundlagen, Becken und untere Extremität*. Biomechanik der menschlichen Gelenke. Elsevier, Urban & Fischer, 2004.

[87] C. Knop, U. Lange, L. Bastian, and M. Blauth. Three-dimensional motion analysis with synex. comparative biomechanical test series with a new vertebral body replacement for the thoracolumbar spine. *Eur Spine J*, 9(6):472–85, 2000.

[88] E. Kreund. The structure of decoupled non-linear systems. *International Journal of Control*, 21(3):443–450, 1975.

[89] D.N. Kunz, R.P. McCabe, T.A. Zdeblick, and R. Vanderby Jr. A multi-degree of freedom system for biomechanical testing. *J Biomech Eng*, 116(3):371–3, 1994.

[90] I. Kutzner, B. Heinlein, F. Graichen, A. Bender, A. Rohlmann, A. Halder, A. Beier, and G. Bergmann. Loading of the knee joint during activities of daily living measured in vivo in five subjects. *Journal of Biomechanics*, 43(11):2164 – 2173, 2010.

[91] L. Lamport. *LATEX: a document preparation system: user's guide and reference manual*. Number S. 2. Addison-Wesley Pub. Co., 1994.

[92] Donghun Lee and Jihun Park. Estimation of camera parameters from a single moving camera using quaternion-based interpolation of 3d trajectory. In *Proc. Computer Graphics, Imaging and Visualisation CGIV '07*, pages 77–80, 2007.

[93] Simon Lenschow, Thore Zantop, Andre Weimann, Thomas Lemburg, Michael Raschke, Michael Strobel, and Wolf Petersen. Joint kinematics and in situ forces after single bundle pcl reconstruction: a graft placed at the center of the femoral attachment does not restore normal posterior laxity. *Archives of Orthopaedic and Trauma Surgery*, 126:253–259, 2006. 10.1007/s00402-005-0062-9.

[94] Guoan Li, Thomas J. Gill, Louis E. DeFrate, Shay Zayontz, Vaida Glatt, and Bertram Zarins. Biomechanical consequences of pcl deficiency in the knee under simulated muscle loads an in vitro experimental study. *Journal of Orthopaedic Research*, 20(4):887–892, 2002.

[95] D.P. Lindsey, K.E. Swanson, P. Fuchs, K.Y. Hsu, J.F. Zucherman, and S.A. Yerby. The effects of an interspinous implant on the kinematics of the instrumented and adjacent levels in the lumbar spine. *Spine*, 28(19):2192–7, 2003.

[96] Glen Livesay, Hiromichi Fujie, Shinji Kashiwaguchi, Duane Morrow, Freddie Fu, and Savio Woo. Determination of the in situ; forces and force distribution within the human anterior cruciate ligament. *Annals of Biomedical Engineering*, 23:467–474, 1995. 10.1007/BF02584446.

[97] JiaHsuan Lo, Otto Müller, Markus Wünschel, Steffen Bauer, and Nikolaus Wülker. Forces in anterior cruciate ligament during simulated weight-bearing flexion with anterior and internal rotational tibial load. *Journal of Biomechanics*, 41(9):1855 – 1861, 2008.

[98] R. D. Lorenz and K. W. Van Patten. High-resolution velocity estimation for all-digital, ac servo drives. *IEEE J IA*, 27(4):701–705, 1991.

[99] J. Luh, M. Walker, and R. Paul. Resolved-acceleration control of mechanical manipulators. *IEEE J AC*, 25(3):468–474, 1980.

[100] Ming Luo, Baohai Wu, Dinghua Zhang, Shan Li, and Ying Zhang. Toolpath generation for four-axis rough milling of sculptured surface turbine blade. In *Proceedings of the First International Conference on Intelligent Robotics and Applications: Part II*, ICIRA '08, pages 887–895, Berlin, Heidelberg, 2008. Springer-Verlag.

[101] J.T. Lysack, J.P. Dickey, G.A. Dumas, and D. Yen. A continuous pure moment loading apparatus for biomechanical testing of multi-segment spine specimens. *J Biomech*, 33(6):765–70, 2000.

[102] Donghai Ma and J. M. Hollerbach. Identifying mass parameters for gravity compensation and automatic torque sensor calibration. In *Proc. Conf. IEEE Int Robotics and Automation*, volume 1, pages 661–666, 1996.

[103] K Mabuchi and H Fujie. Use of robotics technology to measure friction in animal joints. *Clinical Biomechanics*, 11(3):121 – 125, 1996.

[104] F. Magerl, M. Aebi, S. Gertzbein, J. Harms, and S. Nazarian. A comprehensive classification of thoracic and lumbar injuries. *European Spine Journal*, 3:184–201, 1994. 10.1007/BF02221591.

[105] N. Marcassus, P. O. Vandanjon, A. Janot, and M. Gautier. Minimal resolution needed for an accurate parametric identification - application to an industrial robot arm. In *Proc. IEEE/RSJ Int. Conf. Intelligent Robots and Systems IROS 2007*, pages 2455–2460, 2007.

[106] Marko Munih Matjaz Mihelj. Open architecture xpc target based robot controllers for industrial and research manipulators. In *Proc. ICRA 2010 Workshop on Innovative Robot Control Architectures for Demanding (Research) Applications*, June 2010.

[107] R. A. Mayo. Relative quaternion state transistion relation. *Journal of Guidance, Control, and Dynamics*, 2:44–48, 1979.

[108] T. Morita, F. Kuribara, Y. Shiozawa, and S. Sugano. A novel mechanism design for gravity compensation in three dimensional space. In *Proc. IEEE/ASME Int. Conf. Advanced Intelligent Mechatronics AIM 2003*, volume 1, pages 163–168, 2003.

[109] Ephrat Most. Development of a 6-dof robotic test system for studying the biomchanics of total knee replacement. Master's thesis, Massachusetts Institute of Technology, June 2000.

[110] Trevor N. Mudge and Jerry L. Turney. Unifying robot arm control. *IEEE J IA*, (6):1554–1563, 1984.

[111] R.M. Murray, Z. Li, and S.S. Sastry. *A mathematical introduction to robotic manipulation*. CRC Press, 1994.

[112] A. Nachemson. Disc pressure measurements. *Spine*, 1981.

[113] A. Nachemson and J. M. Morris. In vivo measurements of intradiscal pressure: Discometry, a method for the determination of pressure in the lower lumbar discs. *Journal of Bone and Joint Surgery (Am.)*, 46A:1077–1092, 1964.

[114] C. Natale. *Interaction control of robot manipulators: six degrees-of-freedom tasks*. Springer tracts in advanced robotics. Springer, 2003.

[115] C. Natale, B. Siciliano, and L. Villani. Control of moment and orientation for a robot manipulator in contact with a compliant environment. In *Proc. IEEE Int Robotics and Automation Conf*, volume 2, pages 1755–1760, 1998.

[116] B. Nemec and L. Zlajpah. On adaptive control of force controlled manipulators-implementation and experimental results. In *Proc. Conf. IEEE Int Robotics and Automation*, pages 1882–1888, 1992.

[117] F.H. Netter, F.H. Netter, and J.T. Hansen. *Atlas der Anatomie des Menschen*. Thieme, 2006.

[118] D. Omrcen. Measuring of knee movement using industrial robot. Technical report, Intitut Jozef Stefan, 2002.

[119] M. M. Panjabi. Biomechanical evaluation of spinal fixation devices: I. a conceptual framework. *Spine*, 13:1129–1134, 1988.

[120] Manohar M. Panjabi, Martin H. Krag, and Vijay K. Goel. A technique for measurement and description of three-dimensional six degree-of-freedom motion of a body joint with an application to the human spine. *Journal of Biomechanics*, 14(7):447 – 449, 451–460, 1981.

[121] M.M. Panjabi. The stabilizing system of the spine. part ii. neutral zone and instability hypothesis. *J Spinal Disord*, 5(4):390–6; discussion 397, 1992.

[122] Christos D. Papageorgiou, Jorge E. Gil, Akihiro Kanamori, James A. Fenwick, Savio L-Y. Woo, and Freddie H. Fu. The biomechanical interdependence between the anterior cruciate ligament replacement graft and the medial meniscus. *The American Journal of Sports Medicine*, 29(2):226–231, 2001.

[123] Richard P. Paul and Bruce Shimano. Kinematic control equations for simple manipulators. In *Proc. IEEE Conf. Decision and Control including the 17th Symp. Adaptive Processes*, volume 17, pages 1398–1406, 1978.

[124] R.P. Paul. *Robot manipulators: mathematics, programming, and control : the computer control of robot manipulators*. MIT Press series in artificial intelligence. MIT Press, 1981.

[125] Eshuis Peter. Knee modelling. Technical report, AnyBody Research Project, Aalborg University, 2004.

[126] M. Ponikvar, M. Munih, J. Hoogen, G. Schmidt, and R. Riener. Haptic environment for analysis of smooth arm movements. In *International Conference on Advanced Robotics*, pages 173–178, 2003.

[127] M. H. Raibert and J. J. Craig. Hybrid position/force control of manipulators. *Journal of Dynamic Systems Measurement and Control-transactions of The Asme*, 103, 1981.

[128] Antonius Rohlmann, Lars Bauer, Thomas Zander, Georg Bergmann, and Hans-Joachim Wilke. Determination of trunk muscle forces for flexion and extension by using a validated finite element model of the lumbar spine and measured in vivo data. *Journal of Biomechanics*, 39(6):981 – 989, 2006.

[129] T. W. Rudy, G. A. Livesay, S. L-Y. Woo, and F. H. Fu. A combined robotic/universal force sensor approach to determine in situ forces of knee ligaments. *Journal of Biomechanics*, 29(10):1357–1360, 1996.

[130] Masataka Sakane, Ross J. Fox, Savio L-Y. Woo Glen, A. Livesay, Guoan Li, and Freddie H. Fu. In situ forces in the anterior cruciate ligament and its bundles in response to anterior tibial loads. *Journal of Orthopaedic Research*, 15(2):285–293, 1997.

[131] W. Schmoelz, J. Huber, T. Nydegger, L. Claes, and H. Wilke. Influence of a dynamic stabilisation system on load bearing of a bridged disc: an in vitro study of intradiscal pressure. *European Spine Journal*, 15:1276–1285, 2006. 10.1007/s00586-005-0032-5.

[132] W. Schmoelz, U. Onder, A. Martin, and A. von Strempel. Non-fusion instrumentation of the lumbar spine with a hinged pedicle screw rod system: an in vitro experiment. *Eur Spine J*, 18:1478–1485, 2009.

[133] Udo Schumacher. *Prometheus - Lernatlas der Anatomie*. Thieme Georg Verlag, sep 2007.

[134] L. Sciavicco and B. Siciliano. *Modelling and control of robot manipulators*. Advanced textbooks in control and signal processing. Springer, 2000.

[135] Robert Scott. *A three-dimensional Mathematical Model of the Human Knee Joint*. PhD thesis, Massachusetts Institute of Technology, 1990.

[136] H. Seraji. Adaptive independent joint control of manipulators: theory and experiment. In *Proc. Conf. IEEE Int Robotics and Automation*, pages 854–861, 1988.

[137] S W Shepperd. Quaternion from rotation matrix. *Journal of Guidance, Control, and Dynamics*, 1:223–224, 1978.

[138] B. Siciliano and O. Khatib. *Springer handbook of robotics*. Springer, 2008.

[139] B. Siciliano, L. Sciavicco, and L. Villani. *Robotics: modelling, planning and control*. Advanced textbooks in control and signal processing. Springer, 2009.

[140] M.W. Spong and M. Vidyasagar. *Robot Dynamics And Control*. Wiley India Pvt. Ltd., 2008.

[141] I.A. Stokes, M. Gardner-Morse, D. Churchill, and J.P. Laible. Measurement of a spinal motion segment stiffness matrix. *J Biomech*, 35(4):517–21, 2002.

[142] STÄUBLI FAVERGES. *Roboterarm - Baureihe RX90B*, 2000.

[143] R.E. Thompson, T.M. Barker, and M.J. Pearcy. Defining the neutral zone of sheep intervertebral joints during dynamic motions: an in vitro study. *Clin Biomech (Bristol, Avon)*, 18(2):89–98, 2003.

[144] A. Tilli and M. Montanari. A low-noise estimator of angular speed and acceleration from shaft encoder measurements. *Journal Automatika*, 3-4:169–176, 2001.

[145] Oguzhan Turan. *Biomechanischer Vergleich Expandierbarer Cages in einem Korporektomiemodell an der humanen Halswirbelsäule*. PhD thesis, Chartié. Universitätsmedizin Berlin, 2009.

[146] T. M. Vogrin, J. Höher, A. Årøen, S. L-Y. Woo, and C. D. Harner. Effects of sectioning the posterolateral structures on knee kinematics and in situ forces in the posterior cruciate ligament. *Knee Surgery, Sports Traumatology, Arthroscopy*, 8:93–98, 2000. 10.1007/s001670050193.

[147] Matthew R Walker and James P Dickey. New methodology for multi-dimensional spinal joint testing with a parallel robot. *Medical & Biological Engineering & Computing*, 45(3):297–304, 2007.

[148] Yasuhiko Watanabe, Andrew Van Scyoc, Eiichi Tsuda, Richard E. Debski, and Savio L-Y. Woo. Biomechanical function of the posterior horn of the medial meniscus: a human cadaveric study. *Journal of Orthopaedic Science*, 9:280–284, 2004. 10.1007/s00776-004-0781-8.

[149] N. Wen, F. Lavaste, J. J. Santin, and J. P. Lassau. Three-dimensional biomechanical properties of the human cervical spine in vitro. *European Spine Journal*, 2:12–15, 1993. 10.1007/BF00301049.

[150] P. Westerhoff, F. Graichen, A. Bender, A. Halder, A. Beier, A. Rohlmann, and G. Bergmann. In vivo measurement of shoulder joint loads during activities of daily living. *Journal of Biomechanics*, 42(12):1840 – 1849, 2009.

[151] A.A. White and M.M. Panjabi. *Clinical biomechanics of the spine*. Lippincott, 1990.

[152] D. Whitney. Historical perspective and state of the art in robot force control. In *Proc. IEEE Int. Conf. Robotics and Automation*, volume 2, pages 262–268, 1985.

[153] H. Wilke, J. Drumm, K. Häussler, C. Mack, W. Steudel, and A. Kettler. Biomechanical effect of different lumbar interspinous implants on flexibility and intradiscal pressure. *Eur Spine J*, 17:1049–1056, 2008.

[154] H.J. Wilke, L. Claes, H. Schmitt, and S. Wolf. A universal spine tester for in vitro experiments with muscle force simulation. *Eur Spine J*, 3(2):91–7, 1994.

[155] H.J. Wilke, P. Neef, M. Caimi, T. Hoogland, and L.E. Claes. New in vivo measurements of pressures in the intervertebral disc in daily life. *Spine*, 24(8):755–62, 1999.

[156] H.J. Wilke, P. Neef, M. Caimi, T. Hoogland, and L.E. Claes. New in vivo measurements of pressures in the intervertebral disc in daily life. *Spine*, 24(8):755–62, 1999.

[157] H.J. Wilke, K. Wenger, and L. Claes. Testing criteria for spinal implants: recommendations for the standardization of in vitro stability testing of spinal implants. *Eur Spine J*, 7(2):148–54, 1998.

[158] A. Winkler and J. Suchy. Dynamic force/torque measurement using a 12dof sensor. In *Proc. IEEE/RSJ Int. Conf. Intelligent Robots and Systems IROS 2007*, pages 1870–1875, 2007.

[159] C.M. Wiseman, D.P. Lindsey, A.D. Fredrick, and S.A. Yerby. The effect of an interspinous process implant on facet loading during extension. *Spine*, 30(8):903–7, 2005.

[160] T. Wongratanaphisan and M. Chew. Gravity compensation of spatial two-dof serial manipulators. *Journal of Robotic Systems*, 19(7):329–347, 2002.

[161] Savio Woo, Rui Liang, and Matthew Fisher. Future of orthopaedic sports medicine and soft tissue healing: The important role of engineering. *Cellular and Molecular Bioengineering*, 2:448–461, 2009. 10.1007/s12195-009-0065-7.

[162] Savio L.-Y. Woo, Steven D. Abramowitch, Robert Kilger, and Rui Liang. Biomechanics of knee ligaments: injury, healing, and repair. *Journal of Biomechanics*, 39(1):1 – 20, 2006.

[163] Savio L-Y Woo, Richard E Debski, Eric K Wong, Masayoshi Yagi, and Danyel Tarinelli. Use of robotic technology for diathrodial joint research. *Journal of Science and Medicine in Sport*, 2(4):283 – 297, 1999.

[164] Savio L-Y. Woo, Ross J. Fox, Masataka Sakane, Glen A. Livesay, Theodore W. Rudy, and Freddie H. Fu. Biomechanics of the acl: Measurements of in situ force in the acl and knee kinematics. *The Knee*, 5(4):267 – 288, 1998.

[165] G. Wu and P.R. Cavanagh. Isb recommendations for standardization in the reporting of kinematic data. *J Biomech*, 28(10):1257–61, 1995.

[166] T. Yoshikawa. Dynamic hybrid position/force control of robot manipulators description of hand constraints and calculation of joint driving force. In *Proc. IEEE Int. Conf. Robotics and Automation*, volume 3, pages 1393–1398, 1986.

[167] T. Yoshikawa, T. Sugie, and M. Tanaka. Dynamic hybrid position/force control of robot manipulators–controller design and experiment. In *Proc. IEEE Int. Conf. Robotics and Automation*, volume 4, pages 2005–2010, 1987.

[168] J. S. Yuan. Closed-loop manipulator control using quaternion feedback. *IEEE J JRA*, 4(4):434–440, 1988.

[169] Giovanni Zamarra, Matthew Fisher, Savio Woo, and Giuliano Cerulli. Biomechanical evaluation of using one hamstrings tendon for acl reconstruction: a human cadaveric study. *Knee Surgery, Sports Traumatology, Arthroscopy*, 18:11–19, 2010. 10.1007/s00167-009-0911-0.

[170] Nephi A. Zufelt. A kinematics-based testing protocol to study the mechanics of the human lumbar spine. Master's thesis, University of Tennessee Health Science Center, 2008.